A novel porous Ffowcs-Williams and Hawkings acoustic methodology for complex geometries

A THESIS
SUBMITTED TO THE FACULTY OF THE GRADUATE SCHOOL
OF THE UNIVERSITY OF MINNESOTA
BY

Zane Lloyd Nitzkorski

IN PARTIAL FULFILLMENT OF THE REQUIREMENTS
FOR THE DEGREE OF
Doctor of Philosophy

Krishnan Mahesh, Adviser

August, 2015

Acknowledgements

Thank you to everyone one who has encouraged me through the years. Professor Mahesh, whose support and direction were invaluable. He is motivating and incredibly encouraging. His depth of understanding has greatly inspired and taught me about the field of fluid dynamics.

To my office mates for the interesting discussions, and to those students who came before for all of their help and guidance.

To my wife and family, I can't express how instrumental your support has been.

This work has been supported by the United States Office of Naval Research (ONR) under Grant No. N00014-14-1-0304 with Dr. Ki-Han Kim as technical monitor.

Computing resources were provided by Minnesota Scientific computing Institute, the High Performance Computing centers at the Department of Defense, and the National Science Foundation through XSEDE resources provided by XSEDE Science Gateway progarm.

Dedication

To my loving wife, family, and pugs.

Abstract

Predictive noise calculations from high Reynolds number flows in complex engineering geometry are becoming a possibility with the high performance computing resources that have become available in recent years. Increasing the applicability and reliability of solution methodologies have been two key challenges toward this goal. This dissertation develops a porous Ffowcs-Williams and Hawkings methodology that uses a novel endcap methodology, and can be applied to unstructured grids. The use of unstructured grids allows complex geometry to be represented while porous formulation eliminates difficulties with the choice of acoustic Green's function. Specifically, this dissertation (1) proposes and examines a novel endcap procedure to account for spurious noise, (2) uses the proposed methodology to investigate noise production from a range of subcritical Reynolds number circular cylinders, and (3) investigates a trailing edge geometry for noise production and to illustrate the generality of the Green's function.

Porous acoustic analogies need an endcap scheme in order to prevent spurious noise due to truncation errors. A dynamic end cap methodology is proposed to account for spurious contributions to the far–field sound within the context of the Ffowcs–Williams and Hawkings (FW–H) acoustic analogy. The quadrupole source terms are correlated over multiple planes to obtain a convection velocity which is then used to determine a corrective convective flux at the FW–H porous surface. The proposed approach is first demonstrated for a convecting potential vortex. The correlation is investigated by examining it pass through multiple exit planes. It is then evaluated by computing the sound emitted by flow over a circular cylinder at Reynolds number of 150 and compared to other endcap methods, such as Shur et al. [1]. Insensitivity to end plane location and spacing and the effect of the dynamic convection velocity are computed.

Subcritical Reynolds number circular cylinder flows are investigated at $Re = 3900$, 10000 and 89000 in order to evaluate the method and investigate the physical sources of noise production. The $Re = 3900$ case was chosen due to its highly validated flow-field and to serve as a basis of comparison. The $Re = 10000$ cylinder is used to validate the noise production at turbulent Reynolds numbers against other simulations. Finally the $Re = 89000$ simulations are used to compare to experiment serving as a rigorous test

of the methods predictive ability. The proposed approach demonstrates better performance than other commonly used approaches with the added benefit of computational efficiency and the ability to query independent volumes. This gives the added benefit of discovering how much noise production is directly associated with volumetric noise contributions. These capabilities allow for a thorough investigation of the sources of noise production and a means to evaluate proposed theories. A physical description of the source of sound for subcritical Reynolds number cylinders is established.

A 45° beveled trailing edge configuration is investigated due to its relevance to hydrofoil and propeller noise. This configuration also allows for the evaluation of the assumption associated with the free-space Green's function since the half-plane Green's function can be used to represent the solution to the wave equation for this geometry. Similar results for directivity and amplitudes of the two formulations confirm the flexibility of the porous surface implementation. Good agreement with experiment is obtained. The effect of boundary layer thickness is investigated. The noise produced in the upper half plane is significantly decreased for the thinner boundary layer while the noise production in the lower half plane is only slightly decreased.

Contents

List of Tables

List of Figures

Chapter 1

Introduction

1.1 Motivation

Noise production and abatement from turbulent flows is of interest for a variety of applications including airframe noise from aircraft take-off/landings, jet engines, and marine vehicles as shown in figure 1.1. Acoustic emissions from these types of machines have become an increasingly important design consideration for next generation technology. Two key features stand out in these examples; it is the received noise at considerable distance that is usually of interest, and there is the need to handle complex engineering geometries. Computational acoustics uses computational fluid dynamics (CFD) to solve the compressible Navier-Stokes equations to propagate the acoustic signal to the desired location. This is computationally very expensive at high Reynolds (Re) number due to the need for high fidelity, high-order methods to resolve a sound field usually three to six orders of magnitude smaller than the mean flow, also fine grids with large numbers of grid points are required to prevent dissipation or dispersion of the acoustic field over large distances from the source.

For this reason, traditionally, computational acousticians decouple the source field from the propagation field. The source field is computed using high fidelity direct numerical simulation (DNS), large-eddy simulation (LES), detached eddy simulation (DES), or Reynolds Averaged Navier Stokes (RANS). As pointed out in Lyrintzis [9], two dominant approaches exist to obtain the far-field sound: (1) the direct approach of

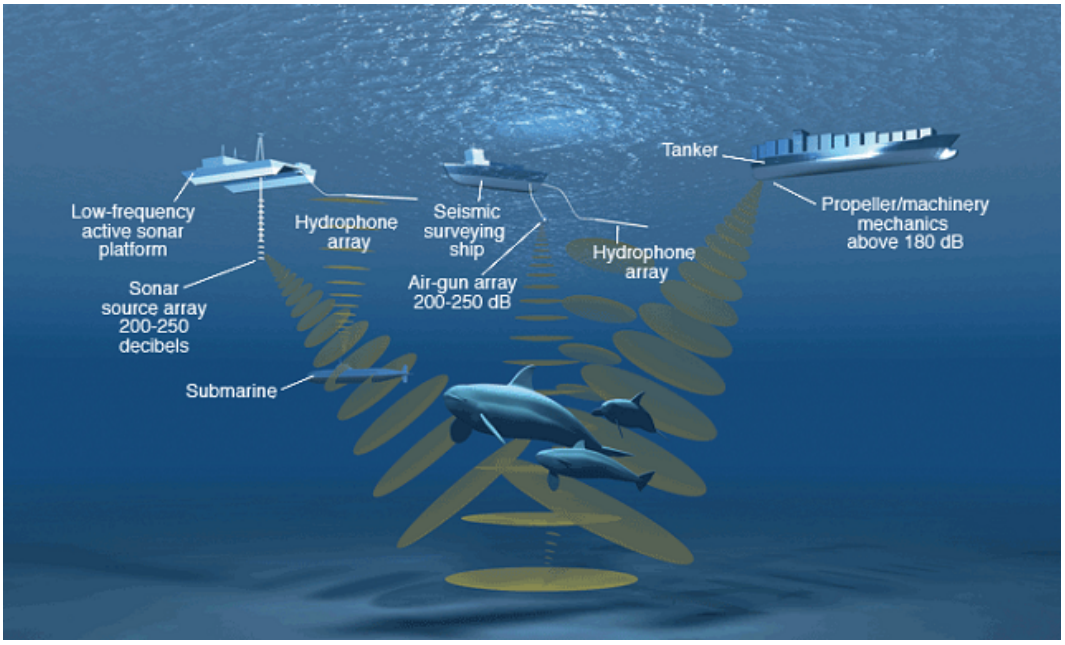

Figure 1.1: Marine acoustic environment example from www.underwaternoise.net

computing the propagating wave all the way to far-field or (2) using an integration surface which serves as the sources for a wave equation which is solved analytically. Direct approaches include solving a modified wave equation or the linearized Euler equations (LEE); they require large grids and can suffer from errors originating from the coupling of the linearized equations to the source region. Acoustic analogies analytically propagate the acoustic field by solving a wave equation with a relevant Green's function. There are many implementations, but the Ffowcs-Williams and Hawkings (FWH) porous surface implementation is the focus of this thesis.

Work on acoustic analogies in the current context started when Lighthill [10] constructed a wave equation decomposition for turbulent free shear flow and demonstrated scalings associated with jet-noise. The work by Curle [11] advanced this approach by describing the effect of volume sources as they interacted with solid bodies with the inclusion of a Green's function to solve for the wave equation. Ffowcs-Williams and Hawkings [12] generalized this formulation to allow for porous surfaces and moving media. Since there are not many well-defined Green's functions applicable for engineering geometries the porous surface approach allows for carefully selecting bounding surfaces

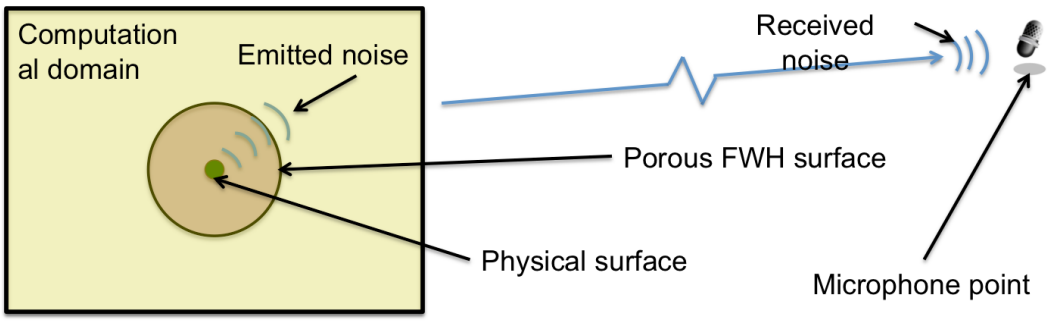

Figure 1.2: A general sound schematic for how porous FWH surfaces are constructed and acoustic noise is computed.

which encompass the dominant sound sources and therefore allow the use of the free space Greens function to propagate noise exterior to that surface. An example of this concept is shown in figure 1.2 demonstrating the key feature that the domain is decomposed into the physical surface, a possible porous data surface through which sound transits, an external volume, and a distant receiver location to which the source terms are propagated.

An important implementation aspect in using the porous FWH acoustic analogies involves how undamped acoustic sources are handled at the exit plane. There have been a variety of approaches for dealing with this problem which are examined more closely in chapter 3. A sample of computational layouts are shown in schematic figure 1.3. The FWH equations allow for computation of noise based on terms which are integrated at the physical body or on a porous data surface. As will be discussed in chapter 2 the configuration of where to place the porous data surface and what volume of integration should be used are important considerations that must be made before the calculation is performed.

In the presence of mean background velocity U_c, acoustic waves undergo convective amplification and Doppler shift. The equations which relate the changes due to Doppler effects retain three components; the motion of the source, observer, and medium. The acoustic analogy approach allows for the independent motion of all three components to be represented separately. If the either the medium, v_m, or source, v_s, have relative velocity to the observer the wavelength of the received noise changes. If the source and observer, v_o, have relative velocity then there is a frequency shift. All of the combined

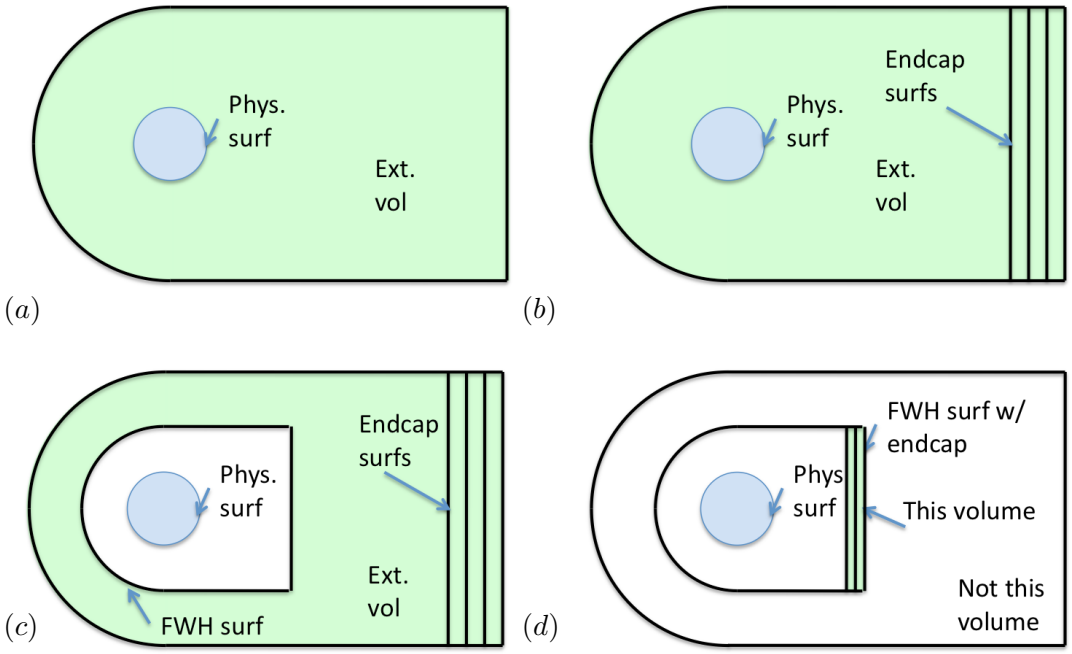

Figure 1.3: Different computational setups for porous FWH implementations with endcaps. (d) is the chosen method for the current work. (a) represents a computational domain which lacks both a porous surfaces and any endcap setup. (b) utilizes the entire computational domain, still lacking a porous surface instead relying on the physical surface, but includes a endcap setup. (c) includes both a porous surface and an endcap setup but the volume domain is large, especially if most of the acoustic source regions are inside the porous surface. (d) is an efficient porous FWH setup with a endcap correction scheme to account for any volume errors.

effects for frequency f shifts, changes in wavelength λ, or wave particle velocity v and are expressed as

$$\lambda' = \lambda(1 + v_m/v - v_s/v) \tag{1.1}$$

$$f' = f\frac{1 + v_m/v + v_o/v}{1 + v_m/v - v_s/v} \tag{1.2}$$

$$v' = v + v_m + v_o \tag{1.3}$$

This is the reason the convective test cases in chapter 2 and the dipole type sound from cylinders in chapter 3 are slanted forward; in the upstream direction wave fronts are compressed and more intense sound results. From the acoustic pressure p, either the sound pressure level (SPL) measured in decibels (dB) or acoustic intensity measured in

W/m^2 is computed:

$$SPL = 20 \log_{10}(p/p_{ref}) dB \tag{1.4}$$

and acoustic intensity is $I = pv$ where v is the acoustic particle velocity. p_{ref} is usually 2e-5 for air and 1e-6 for water. The speed of sound c_0 is defined as,

$$c_0^2 = \left(\frac{\partial p}{\partial \rho}\right)_s . \tag{1.5}$$

1.2 Overview

This dissertation develops the capability to predict noise from engineering configurations and provide physical insight into the production and propagation of noise. Principally it is developed in the context of bluff body flows but is an approach which is widely adaptable. First, a novel endcap closure method is proposed to correct for a deficit in the FWH equations and examined in the context of bluff body flows. Next, LES is performed for cylinders at various Reynolds numbers to serve as validation for the approach and investigate the effects of increasing Reynolds number on noise production and propagation. Finally, the method is used to examine a trailing edge configuration to examine its applicability in an engineering context. An overview of relevant past work as well as a summary or important results are provided in each chapter.

The principal contributions of this work are as follows:

- A Ffowcs-Williams and Hawkings porous surface acoustic analogy is developed and described in the context of wall resolved LES. To this end, a review and derivation of the FWH equations are provided with emphasis on the the assumptions involved and their impact on implementation. This acoustic analogy is then validated for test cases of a point monopole, dipole, and quadrupole. Surface and volume extraction techniques are described and validated.

- A novel endcap method is proposed to account for the closure problem associated with the FWH equations. The approach relates fluxes on the exit FWH surface to volume terms in a neighboring volume and applies a corrective convective flux to the neighboring volume. Furthermore a dynamic averaging scheme is proposed to solve for the convection velocity.

- This proposed endcap approach is then compared and contrasted with other closure schemes for a $Re = 150$ cylinder. The sound field is validated by comparing to the work of Inoue and Hatakeyama [3], and the current approach shows improved accuracy over other schemes. The sensitivity of the proposed approach is also examined and shown to be largely insensitive to endcap location or spacing.

- LES of turbulent cylinders at $Re = 3900,\ 10000,$ and 890000 are performed in order to validate the noise predictions with the computations of Khalighi et al. [4] for the $Re = 10000$ cylinder and the experiments of Revell et al. [5] for the $Re = 89000$ cylinder. Good agreement is obtained for both cases and much better agreement with experiment is demonstrated over previous URANS computations of Cox et al. [6]. A mechanistic examination of the sound sources and the effect of Reynolds number is performed.

- LES is performed of a 45° beveled trailing edge configuration. This configuration examines fully separated turbulent wakes interacting and scattering on sharp trailing edges. A recycle rescale methodology following the work of Lund et al. [13] is implemented to prescribe inflow conditions for two boundary layer thicknesses. Sound sources are examined and good agreement is obtained with the experiments of Olson and Mueller [7], and the impact on boundary layer thickness is investigated. The proposed approach with its universal choice of the free-space Green's function is shown to agree with the predictions obtained using surface terms along with an analytical half-plane Green's function.

This dissertation is organized as follows. Chapter 2 covers the governing equations and derivation of the Ffowcs-Williams and Hawkings acoustic analogy as well as a discussion of the algorithm and numerical discretization of the flow solver and acoustic analogy for unstructured grids. The acoustic analogy solver is then validated for simple canonical cases. Chapter 3 introduces the endcap closure problem and the novel proposed solution. This is tested for a simple vortex model and then using Re=150 cylinder flow to validate and compare and contrast with other endcap schemes. Chapter 4 examines the effect of Reynolds number on noise production for cylinder flows in the subcritical regime. A discussion of analysis techniques and source effects is documented. Trailing edge noise production is investigated in chapter 5 and the effect of

boundary layer thickness as a sound source is investigated. Furthermore, the validity of the free-space Green's function is examined.

Chapter 2

Acoustic analogy arrangement of the governing Navier-Stokes equations

2.1 Navier-Stokes equations

The governing equations for a compressible fluid are the compressible Navier–Stokes (N–S) equations:

$$\frac{\partial \rho}{\partial t} + \frac{\partial \rho u_j}{\partial x_j} = 0, \tag{2.1}$$

$$\frac{\partial \rho u_i}{\partial t} + \frac{\partial \rho u_i u_j}{\partial x_j} = -\frac{\partial p}{\partial x_i} + \frac{\partial \tau_{ij}}{\partial x_j}, \tag{2.2}$$

$$\frac{\partial \rho E}{\partial t} + \frac{\partial \left(\rho E + p\right) u_j}{\partial x_j} = \frac{\partial \tau_{ij} u_i}{\partial x_j} + \frac{\partial}{\partial x_j}\left(k \frac{\partial T}{\partial x_j}\right) \tag{2.3}$$

with equation of state,

$$p = \rho R T. \tag{2.4}$$

The variables ρ, p, and u_i denote the density, pressure, and velocities respectively. E is the total energy per unit mass and $\tau_{ij} = \mu\left(\frac{\partial u_i}{\partial x_j} + \frac{\partial u_j}{\partial x_i} - \frac{2}{3}\frac{\partial u_k}{\partial x_k}\delta_{ij}\right)$ is the viscous stress tensor with viscosity μ. $k = \frac{\mu}{(\gamma-1)M_\infty^2 RePr}$ is the thermal conduction coefficient with

Mach number M_∞, Reynolds number Re, and Prandtl number Pr. The equations 2.1 and 2.2 describe the evolution of mass and momentum of a fluid element respectively. If the density is assumed fixed for these equations the incompressible N–S equations are obtained:

$$\frac{\partial u_i}{\partial x_i} = 0, \tag{2.5}$$

$$\frac{\partial u_i}{\partial t} + \frac{\partial u_i u_j}{\partial x_j} = -\frac{\partial p/\rho}{\partial x_i} + \frac{\partial \tau_{ij}}{\partial x_j}, \tag{2.6}$$

where the density has been absorbed into the pressure term. In DNS, these governing equations are solved by resolving all scales down to the Kolmogorov length. In LES, the largest energy containing scales are accurately represented and the sub-grid stresses are modeled to account for the smaller scales.

2.1.1 Large eddy simulation

In LES, the large energy carrying scales of turbulence are directly resolved on the computational grid and the effect of the smaller scales is modeled. The flow variables are decomposed into large scales (denoted by $\overline{(\cdot)}$) and small scales (denoted by $(\cdot)'$):

$$f(\mathbf{x}, t) = \overline{f}(\mathbf{x}, t) + f'(\mathbf{x}, t). \tag{2.7}$$

this decomposition is achieved by applying a low–pass spatial filter G to the flow variable f,

$$\overline{f}(\mathbf{x}, \Delta, t) = G * f(\mathbf{x}, t) = \int_D G(\mathbf{x}, \mathbf{x} - \mathbf{r}; \Delta) f(\mathbf{r}, t) dr, \tag{2.8}$$

where Δ is the filter width and the integration is over the domain of computation.

Applying the filter operation to the N–S equations and assuming commutation with the spatial derivatives yields the filtered N–S equations:

$$\frac{\partial \overline{u}_i}{\partial x_i} = 0, \tag{2.9}$$

$$\frac{\partial \overline{u}_i}{\partial t} + \frac{\partial}{\partial x_j}(\overline{u}_i \overline{u}_j) = -\frac{\partial \overline{p}}{\partial x_i} + \nu \frac{\partial^2 \overline{u}_i}{\partial x_j \partial x_j} - \frac{\partial \tau_{ij}}{\partial x_j}, \tag{2.10}$$

where $\overline{(\cdot)}$ denotes the filtered flow variable at scale Δ and $\tau_{ij} = \overline{u_i u_j} - \overline{u}_i \overline{u}_j$ is the sub–filter scale (SFS) stress which in our implementation uses grid–filtered LES, meaning

$SFS = SGS$. The SGS stress τ_{ij} which are needed close eq. 2.10 are modeled using the surrogate correlation time scale Lagrangian averaging scheme for the dynamic Smagorinsky model developed by Verma and Mahesh [2].

2.1.2 SGS stress model: Verma and Mahesh [2]

The Smagorinsky model [14] relates the anisotropic residual SGS stress to the filtered strain rate $\overline{S}_{ij}$ by an eddy viscosity ν_t

$$\tau_{ij} - \frac{1}{3}\tau_{kk}\delta_{ij} = -2\nu_t\overline{S}_{ij}. \tag{2.11}$$

The eddy viscosity is modeled as

$$\nu_t = l_s^2|\overline{S}| = -2(C_s\Delta)^2|\overline{S}|, \tag{2.12}$$

leading to the SGS stress model

$$\tau_{ij} - \frac{1}{3}\tau_{kk}\delta_{ij} = -2\nu_t\overline{S}_{ij} = -2(C_s\Delta)^2|\overline{S}|\overline{S}_{ij} \tag{2.13}$$

where C_s is a model coefficient and $|\overline{S}| = (2\overline{S}_{ij}\overline{S}_{ij})^{1/2}$ which is typically set to 0.16. However, specifying a constant C_s results in inaccurate prediction especially near walls.

The Dynamic Smagorinsky model (DSM), proposed by [15], removes this limitation by dynamically computing the model coefficient C_s from the resolved scales allowing it to vary in space and time. DSM is based on the Germano identity

$$L_{ij} = T_{ij} - \widehat{\tau}_{ij} \tag{2.14}$$

where

$$L_{ij} = \widehat{\overline{u_i}\overline{u_j}} - \widehat{\overline{u}}_i\widehat{\overline{u}}_j, \qquad T_{ij} = \widehat{\overline{u_i}\overline{u_j}} - \widehat{\overline{u}}_i\widehat{\overline{u}}_j \quad \text{and} \quad \widehat{\tau}_{ij} = \widehat{\overline{u_i}\overline{u_j}} - \widehat{\overline{u_i}}\widehat{\overline{u_j}}. \tag{2.15}$$

Here, $\widehat{(\cdot)}$ denotes test filtering at scale $\widehat{\Delta}$ which is usually taken to be $\widehat{\Delta} = 2\Delta$. T_{ij} is the SGS stress at the test filter scale. L_{ij} is the stress due to scales intermediate between Δ and 2Δ and can be computed directly from the resolved field. Similar to τ_{ij}, the deviatoric part of T_{ij} is modeled using the Smagorinsky model and the dynamic procedure to obtain the SGS model coefficient C_s attempts to minimize the Germano-identity error (GIE),

$$\epsilon_{ij} = (C_s\Delta)^2 M_{ij} - L_{ij}^d, \tag{2.16}$$

where $M_{ij} = 2\left[\widehat{|\overline{S}|\overline{S}}_{ij} - \left(\frac{\hat{\Delta}}{\Delta}\right)^2 \widehat{|\overline{S}|}\widehat{\overline{S}}_{ij}\right]$. The standard DSM approach [15] yields

$$(C_s\Delta)^2 = \frac{(L_{ij}M_{ij})_\Omega}{(M_{ij}M_{ij})_\Omega}, \tag{2.17}$$

where $(\cdot)_\Omega$ denotes averaging over Ω. [15] suggested averaging over homogeneous directions for stability.

The requirement of averaging over at least one homogeneous direction is impractical for complex inhomogeneous flows. Meneveau et al. [16] proposed Lagrangian averaging to obtain a time scale which contained an adjustable parameter θ. Park and Mahesh [17] proposed a dynamic extension to find T for unstructured grids which was extended by Verma and Mahesh [2] and is discussed below. The dynamic time scale minimizes the pathline average of the local GIE squared, ($\mathcal{E} = \epsilon_{ij}\epsilon_{ij}$). The objective function to be minimized is

$$E = \int_{pathline} \epsilon_{ij}(\mathbf{z})\epsilon_{ij}(\mathbf{z})d\mathbf{z} = \int_{-\infty}^{t} \epsilon_{ij}(\mathbf{z}(t'),t')\epsilon_{ij}(\mathbf{z}(t'),t')W(t-t')dt' \tag{2.18}$$

where $\mathbf{z}$ is the trajectory for earlier times $t' < t$ and W is a weighting function to control the relative importance of events near time t.

Choosing the time weighting function of the form $W(t-t') = T^{-1}e^{-(t-t')/T}$ yields two transport equations for the Lagrangian average of the tensor products $L_{ij}M_{ij}$ and $M_{ij}M_{ij}$ as $\mathcal{I}_{LM}$ and $\mathcal{I}_{MM}$ respectively as,

$$\frac{D\mathcal{I}_{LM}}{Dt} \equiv \frac{\partial \mathcal{I}_{LM}}{\partial t} + \overline{u}_i\frac{\partial \mathcal{I}_{LM}}{\partial x_i} = \frac{1}{T}\big(L_{ij}M_{ij} - \mathcal{I}_{LM}\big) \quad \text{and} \tag{2.19}$$

$$\frac{D\mathcal{I}_{MM}}{Dt} \equiv \frac{\partial \mathcal{I}_{MM}}{\partial t} + \overline{u}_i\frac{\partial \mathcal{I}_{MM}}{\partial x_i} = \frac{1}{T}\big(M_{ij}M_{ij} - \mathcal{I}_{MM}\big). \tag{2.20}$$

whose solutions yields

$$(C_s\Delta)^2 = \frac{\mathcal{I}_{LM}}{\mathcal{I}_{MM}}. \tag{2.21}$$

Here T is a time scale which represents the 'memory' of the Lagrangian averaging.

The procedure uses an osculating parabola constructed to pass through three points of a running average of the surrogate Lagrangian correlations which are constructed from five points of the instantaneous GIE squared. These correlations are then normalized by the zero-separation correlation $\mathcal{C}(0)$ to obtain

$$\rho(0) = 1, \qquad \rho(\Delta t) = \frac{\mathcal{C}(\Delta t)}{\mathcal{C}(0)}, \qquad \rho(2\Delta t) = \frac{\mathcal{C}(2\Delta t)}{\mathcal{C}(0)}. \tag{2.22}$$

The time scale which results from this surrogate correlation procedure for timesteps beyond the first is

$$T_{SC} = min\left[\frac{dt}{\sqrt{1-\rho(\Delta t)}}, \frac{2dt}{\sqrt{1-\rho(2\Delta t)}}\right]. \tag{2.23}$$

The minimum of the time scales is chosen so that the solution has lesser dependence on past values and can evolve faster from the initial transient stage. A simple material derivative as proposed by Park and Mahesh [17] is used to approximate Lagrangian quantities in an Eulerian framework. Verma and Mahesh [2] discuss the details of the methodology. It is shown that the procedure works well on unstructured grids and shows improvement over existing averaged DSM methods.

2.1.3 N-S discretization

Since both the compressible and incompressible formulations are used to compute the noise at various times, an overview of both discretizations are provided. The details of the discretization for the incompressible equations can be found in [18] and in [19] for the compressible equations. The use of the compressible equations provides a direct computation option where enough points are used to resolve the acoustic propagation over the desired distance. This option was only used for validation for the low Reynolds number cylinder flow in chapter 3 since this approach becomes untenable at high Reynolds number. Instead the incompressible equations are used to get the source fields. [4], [20], [21], and others have used incompressible hydrodynamic fields to provide the source fields for the acoustic analogy schemes. As pointed out by Howe [22, chapter 2], using an incompressible hydrodynamic field produces an error $O(M^2)$ in most engineering scenarios relative to the compressible equations; meaning that for the largest $M = 0.2$ in this dissertation the errors are acceptably small. The biggest drawback of incompressiblity is that any scattered acoustic field will not be able to interact with the incident acoustic field because everything in the near-field is coupled elliptically. This results in the idea of compactness where the size of the body is smaller than the dominant wavelengths of noise it produces $wl/c << 1$. Further discussion on this topic can be found in Crow [23].

2.1.4 Incompressible formulation

The unstructured grid, finite-volume algorithm for solving the incompressible Navier–Stokes equations is that developed by [18]. The algorithm emphasizes discrete–kinetic energy conservation in the inviscid limit which enables it to simulate high–Reynolds number flows in complex geometries without adding numerical dissipation. Using a predictor–corrector methodology the solution is advanced by first predicting the velocities using the momentum equation alone, and then correcting using the pressure gradient obtained from the Poisson equation yielded by the continuity equation. The time advancement is implicit and uses the Crank–Nicholson discretization with a linearization of the convection terms. The algorithm has been validated for a wide range of complex problems which include a gas turbine combustor geometry [18], predicting propeller crashback [24, 25] and turbulent jets ([26], [27, 28, 29]). The LES subgrid stresses in the present simulations are performed using a dynamic Lagrangian model where the Lagrangian time scale is dynamically computed as proposed by Park and Mahesh [17] and Verma and Mahesh [2].

The Cartesian velocities u_i and pressure p are stored at the centroids of the cells and the face–normal velocities v_n are stored independently at the centroids of the faces. Henceforth, all resolved flow variables will be denoted simply, without the overbar $\overline{()}$.

A predictor–corrector type, fractional–step method is used to solve eq. 2.10. The non–linear convective term is denoted by NL and the viscous term incorporating the SGS stress term is denoted by $VISC$. Explicit time advancement is performed using the Adams–Bashforth scheme which is $O(\Delta t^2)$. The predicted velocities u_i^* at the control volume centroids are first obtained from the previous time steps k and $k-1$:

$$\frac{u_i^* - u_i^k}{\Delta t} = \frac{1}{2}\left[3(NL + VISC)^k - (NL + VISC)^{k-1}\right], \tag{2.24}$$

and then interpolated using symmetric averaging ($O(\Delta x^2)$) to obtain the predicted face–normal velocities:

$$v_n^* = \left(\frac{u_{i,icv1}^* + u_{i,icv2}^*}{2}\right) n_i, \tag{2.25}$$

where the face–normal $\vec{n}$ and hence v_n points from control volume $icv1$ to $icv2$.

The corrector step

$$\frac{u_i^{k+1} - u_i^*}{\Delta t} = -\frac{\partial p^{k+1}}{\partial x_i} \tag{2.26}$$

is projected onto the face–normal as:

$$\frac{v_n^{k+1} - v_n^*}{\Delta t} = -\frac{\partial p^{k+1}}{\partial n}. \tag{2.27}$$

The continuity equation imposes the constraint

$$\sum_{\text{facesofcv}} v_n^{k+1} A_f = 0, \tag{2.28}$$

where A_f is the face area. Substituting in eq. 2.27 yields a Poisson equation for p^{k+1}:

$$\sum_{\text{facesofcv}} v_n^{k+1} A_f - \sum_{\text{facesofcv}} v_n^* A_f \quad = -\Delta t \textstyle\sum_{\text{facesofcv}} \frac{\partial p^{k+1}}{\partial n} A_f \tag{2.29}$$

$$\Rightarrow \Delta t \sum_{\text{facesofcv}} \frac{\partial p^{k+1}}{\partial n} A_f \qquad = \textstyle\sum_{\text{facesofcv}} v_n^* A_f, \tag{2.30}$$

which is solved using the Algebraic Multi-Grid (AMG) method of the library *hypre* [30].

Once p^{k+1} is known, the pressure gradient $\frac{\partial p}{\partial x_i}$ is computed in a novel least squares formulation which minimizes the conservation error:

$$\sum_{\text{facesofcv}} \left(\frac{\partial p}{\partial x_i} n_i A_f - \frac{\partial p}{\partial n} A_f \right)^2. \tag{2.31}$$

Finally, corrected u_i and v_n are computed from eqns. 2.26 and 2.27 using p^{k+1}.

All of the simulations in this dissertation are performed with implicit time advancement using the Crank–Nicolson scheme which is $O(\Delta t^2)$:

$$\frac{u_i^* - u_i^k}{\Delta t} = \frac{1}{2}\left[(NL + VISC)^k + (NL + VISC)^{k+1} \right]. \tag{2.32}$$

$(NL + VISC)^{k+1}$ contains u_i^{k+1} which is expressed in terms of u_i^k as

$$u_i^{k+1} = u_i^* - \Delta t \frac{\partial p^{k+1}}{\partial x_i}, \tag{2.33}$$

where p^{k+1} is linearized as $p^{k+1} = p^k + O(\Delta t)$. Eq. 2.32 reduces to a system of linear equations which is solved for u_i^*.

Note that typically, the face–normal derivatives at a face are computed using

$$\frac{\partial(\cdot)}{\partial n}\Big|_f = \frac{(\cdot)_{nbr} - (\cdot)_{icv}}{d_f}, \tag{2.34}$$

where nbr denotes the neighboring control volume of icv and $d_f = (x_{i,nbr} - x_{i,icv})n_{i,f}$ is the face–normal distance. In chapter 4 of this dissertation, the face–normal derivatives of p, and u_i in $VISC$ are computed using the Improved Deferred Correction method of [31].

2.1.5 Compressible formulation

The compressible equations are solved using an algorithm developed for unstructured grids by [19]. The algorithm employs a least–square method for flux reconstruction on faces of control volumes, viscous flux splitting to ensure that the dominant component only depends on the nearest neighbors and is therefore more accurate at high wavenumbers, and devoid of odd-even decoupling. The algorithm uses a shock–capturing scheme that was originally proposed by [32] for structured meshes and was extended by [19] to unstructured meshes, and further localized to reduce unnecessary numerical dissipation. Time advancement is explicit and uses the second order Adams Bashforth method. The methodology has also been shown to perform well in various complex flows such as supersonic boundary layer transition due to roughness element [33] and distributed roughness [34], and LES of decaying isotropic turbulence and shock/turbulence interaction [35].

A predicted value is first obtained by solving Eqs. (2.1,2.2,2.3) using a symmetric and non-dissipative scheme. The convective fluxes at the face are estimated using a symmetric average with a gradient term using Taylor series expansion to obtain

$$\phi_{f_c} = \frac{\phi_{icv1} + \phi_{icv2}}{2} + \frac{1}{2}\left(\nabla\phi|_{icv1} \cdot \Delta\mathbf{x}^{icv1} + \nabla\phi|_{icv2} \cdot \Delta\mathbf{x}^{icv2}\right), \tag{2.35}$$

where $\Delta\mathbf{x}^{icv1} = \mathbf{x}_{f_c} - \mathbf{x}_{icv1}$, and $\nabla\phi|_{icv1}$denotes the gradient defined at $icv1$.

The viscous term is split into two parts, $\sigma_{ij} = \sigma^1_{ij} + \sigma^2_{ij}$, where $\sigma^1_{ij} = \frac{\mu}{Re}\frac{\partial u_i}{\partial x_j}$ and $\sigma^2_{ij} = \frac{\mu}{Re}\left(\frac{\partial u_j}{\partial x_i} - \frac{2}{3}\frac{\partial u_k}{\partial x_k}\delta_{ij}\right)$. σ^2_{ij} can be interpreted as a 'compressible' contribution, since it vanishes in the incompressible limit. The 'incompressible' component σ^1_{ij} is computed by

$$\frac{1}{V_{\text{cv}}}\sum_{\text{faces}}\left(\frac{\mu}{Re}\right)_f \frac{\partial u_i}{\partial x_j}\Big|_f n_j A_f = \frac{1}{V_{\text{cv}}}\sum_{\text{faces}}\left(\frac{\mu}{Re}\right)_f \frac{\partial u_i}{\partial n}\Big|_f A_f. \tag{2.36}$$

Here, the normal gradient at the face is computed by

$$\frac{\partial \phi}{\partial n} = \frac{\phi_{ifn2} - \phi_{ifn1}}{d_f}, \tag{2.37}$$

where $ifn1$ ($ifn2$) is the projection of $icv1$ ($icv2$) onto the extension of normal vector $\mathbf{n}$ and d_f is the distance between $ifn1$ and $ifn2$. ϕ_{ifn1} is given by

$$\phi_{ifn1} = \phi_{icv1} + \nabla\phi|_{icv1} \cdot (\mathbf{x}_{ifn1} - \mathbf{x}_{icv1}), \tag{2.38}$$

where the linear least-square method is used to determine the gradient $\nabla\phi$ at $icv1$. Viscosity at the cell face is obtained using Eq. 2.35 and a least square reconstruction. Thus, the incompressible part corresponds to a compact-stencil method. $\sigma^2_{ij,f}$ is constructed by the interpolation of $\sigma^2_{ij}\Big|_{icv1}$ and $\sigma^2_{ij}\Big|_{icv2}$.

A second order explicit Adams-Bashforth scheme is used.

$$q_j^{n+1} = q_j^n + \frac{\Delta t}{2}\left[3\mathrm{rhs}_j(\mathbf{q}^n) - \mathrm{rhs}_j(\mathbf{q}^{n-1})\right], \tag{2.39}$$

where rhs_j denotes j^{th} component of the right hand side of the governing equation, and the superscript n denotes the n^{th} time step.

2.2 Ffowcs-Williams and Hawkings equation

The N–S equations can be rearranged into an inhomogeneous wave equation which analytically describes propagation of the sound field relative to the source field. Rearranging the momentum equation 2.2 to obtain

$$\frac{\partial \rho u_i}{\partial t} + \frac{\partial}{\partial x_j}\left(\rho u_i u_j + P_{ij}\right) = 0, \tag{2.40}$$

where $P_{ij} = (p - p_o)\,\delta_{ij} - \tau_{ij}$ and noting that p_o is uniform, shows that we recover the Navier–Stokes equations. The derivation of the equations by using generalized derivatives is detailed by Brentner and Farassat. To take a generalized derivative let $q(x)$ be a function with a discontinuity across a surface $f(x) = 0$. By convention $f > 0$ exterior to the surface and $f < 0$ inside the surface such that ∇f points along the exterior pointing normal. Next, define Δq and the process of generalized differentiation

as

$$\Delta q = q(f = 0+) - q(f = 0-), \tag{2.41}$$

$$\frac{\bar{\partial} q}{\partial x_i} = \frac{\partial q}{\partial x_i} + \Delta q \frac{\partial f}{\partial x_i}\delta(f), \tag{2.42}$$

$$\frac{\bar{\partial} q}{\partial t} = \frac{\partial q}{\partial t} + \Delta q \frac{\partial f}{\partial t}\delta(f), \tag{2.43}$$

where $\delta(f)$ is the Dirac delta function and $\frac{\partial q}{\partial x_i}$ and $\frac{\partial q}{\partial t}$ are the ordinary partial derivatives. $\frac{\partial f}{\partial t}$ is the velocity of the surface in the opposite direction of the surface normal or $-v_n$. Similarly, $\frac{\partial f}{\partial x_i}$ is the normal of the surface n_i. Now taking generalized derivative of the continuity equation yields

$$\begin{aligned}
\frac{\bar{\partial}\rho}{\partial t} + \frac{\bar{\partial}\rho u_i}{\partial x_i} &= \frac{\partial \rho}{\partial t} + \Delta\rho \underbrace{\frac{\partial f}{\partial t}}_{-v_n}\delta(f) + \frac{\bar{\partial}\rho u_i}{\partial x_i} + \Delta(\rho u_i)\underbrace{\frac{\partial f}{\partial x_i}}_{n_i}\delta(f) \\
&= \underbrace{\frac{\partial \rho}{\partial t} + \frac{\partial \rho u_i}{\partial x_i}}_{0 \text{ by continuity}} + \left[\rho_0 v_n - \rho v_n + \rho u_n\right]\delta(f) \\
&= \left[\rho_0 v_n + \rho(u_n - v_n)\right]\delta(f),
\end{aligned} \tag{2.44}$$

which defines the monopole or thickness source as,

$$Q_j n_j = [\rho_0 v_j + \rho(u_j - v_j)]n_j, \tag{2.45}$$

where $u_n = u_j n_j$ and it has been assumed that jump in ρ is from quiescent, ρ_0, to the local density, ρ. Similarly the jump in velocity is assumed to be from a stationary reference condition, $u_{0,j} = 0$ to the local velocity u_j. For the modified momentum equation (2.40) the process is similar.

$$\begin{aligned}
\frac{\bar{\partial}\rho u_i}{\partial t} + \frac{\bar{\partial}}{\partial x_j}\left(\rho u_i u_j + P_{ij}\right) &= \frac{\partial \rho u_i}{\partial t} + \Delta(\rho u_i)\underbrace{\frac{\partial f}{\partial t}}_{-v_n}\delta(f) + \frac{\partial}{\partial x_j}\left(\rho u_i u_j + P_{ij}\right) \\
&\quad + \Delta(\rho u_i u_j + P_{ij})\underbrace{\frac{\partial f}{\partial x_j}}_{n_j}\delta(f) \\
&= \underbrace{\frac{\partial \rho u_i}{\partial t} + \frac{\partial}{\partial x_j}\left(\rho u_i u_j + P_{ij}\right)}_{0 \text{ by equation (2.40)}} + [\rho u_i(u_n - v_n) + \Delta P_{ij} n_j]\delta(f) \\
&= [\rho u_i(u_n - v_n) + \Delta P_{ij} n_j]\delta(f)
\end{aligned} \tag{2.46}$$

which defines the dipole or loading source as,

$$L_{ij} = \rho u_i(u_j - v_j) + \Delta P_{ij}. \tag{2.47}$$

To obtain the FWH equation take the derivative $\frac{\bar{\partial}}{\partial t}$ of equation (2.44) and the then $\frac{\bar{\partial}}{\partial x_i}$ of equation (2.46) and then subtract $\bar{\nabla}^2[c^2(\rho-\rho_0)]$ from both sides and incorporate a substitution of $\rho-\rho_0$ into the $\frac{\bar{\partial}^2\rho}{\partial t^2}$ term since ρ_0 is invariant with respect to time. Finally, rearrange the equation so that the operator acts only on $c^2(\rho-\rho_0)$, this assumes c is invariant of time and if the equation is to capture this quantity in the acoustically linear region, then the substitution $p - p_0 = c^2(\rho - \rho_0)$ is appropriate. One recovers,

$$\begin{aligned}
(\frac{1}{c^2}\frac{\partial^2}{\partial t^2} - \nabla^2)p'(x,t) &= \frac{\partial}{\partial t}\{[\rho_0 v_n + \rho(u_n - v_n)]\delta(f)\} \\
&- \frac{\partial}{\partial x_i}\{[\rho u_i(u_n - v_n) + \Delta P_{ij}n_j]\delta(f)\} \\
+\frac{\partial^2}{\partial x_i \partial x_j}\{(\rho u_i u_j &+ ((p-p_0) - c_0^2(\rho-\rho_0))\delta_{ij} - \tau_{ij})H(f)\},
\end{aligned} \tag{2.48}$$

where the quadrupole or volume term is defined as,

$$T_{ij} = \rho u_i u_j + ((p-p_0) - c_0^2(\rho-\rho_0))\delta_{ij} - \tau_{ij} \tag{2.49}$$

which is also known as the Lighthill stress tensor. So in shortened notation,

$$\begin{aligned}
(\frac{1}{c^2}\frac{\partial^2}{\partial t^2} - \nabla^2)p'(x,t) &= \frac{\partial}{\partial t}\{[Q_i n_i]\delta(f)\} \\
-\frac{\partial}{\partial x_i}\{[L_{ij}n_j]\delta(f)\} &+ \frac{\partial^2}{\partial x_i \partial x_j}\{T_{ij}H(f)\}.
\end{aligned} \tag{2.50}$$

Note that this equation is for a wave in quiescent background flow and would have to be modified to account for background flow as shown in appendix A. The solution to the wave equation depends on the appropriate Green's function based on the geometry of the problem. Usually the free space Green's function is used and is,

$$G(\mathbf{x}, t|\mathbf{y}, \tau) = \frac{1}{4\pi|\mathbf{x}-\mathbf{y}|}\delta(t - \tau - \frac{|\mathbf{x}-\mathbf{y}|}{c_0}) \tag{2.51}$$

and is the causal solution of the wave equation for an impulsive point source $\delta(x - y)\delta(t-\tau)$, located at time $t = \tau$ and $x = y$,

$$\left(\frac{1}{c_0^2}\frac{\partial^2}{\partial t^2} - \nabla^2\right)G = \delta(\mathbf{x}-\mathbf{y})\delta(t-\tau) \text{ where } G = 0 \text{ for } t < \tau. \tag{2.52}$$

2.2.1 Integral Form

The integral solution of the above equations solves for the acoustic response at any point away from the source field. By convention, this describes the fluctuating pressure at position $\vec{\mathbf{x}}$ and time t and the source domain is located at $\vec{\mathbf{y}}$ and time τ which is the emission time or retarded time. Since the wave equation is a linear operator, all the sources are separable and each source location independently effects the received acoustic field. The received noise is the cumulative effect of the monopole or thickness, dipole or loading, and quadrupole or volume terms.

The solution for the portion due to the monopole is obtained by inserting the Green's function and separating source from received noise;

$$p'_m(\mathbf{x},t) = \int_{-\infty}^{t}\int_{-\infty}^{\infty} \frac{\partial}{\partial\tau}\left\{[\rho_0 v_n + \rho(u_n - v_n)]\delta(f)\right\} G(\mathbf{x},t|\mathbf{y},\tau)d^3\mathbf{y}\ d\tau \tag{2.53}$$

with emission or retarded time

$$\tau = t - \frac{|\mathbf{x}-\mathbf{y}|}{c_0}. \tag{2.54}$$

If the distance $R = |\mathbf{x}-\mathbf{y}| \neq R(\tau)$ and the surface $f \neq f(\tau)$ is not a function of τ, this means that the time differential only affects the flow variables. This means we can integrate through the time delta function in (2.51) by switching the integration:

$$\begin{aligned} p'_m(\mathbf{x},t) &= \frac{1}{4\pi}\int_{-\infty}^{\infty}\left[\frac{\frac{\partial}{\partial t}\left([Q_i n_i]\right)\delta(f)}{|\mathbf{x}-\mathbf{y}|}\right]_{\tau=t-R/c_0} d^3\mathbf{y} \\ &= \frac{1}{4\pi}\frac{\partial}{\partial t}\int_S \left[\frac{Q_i n_i}{|\mathbf{x}-\mathbf{y}|}\right]_{ret} dS(y). \end{aligned} \tag{2.55}$$

This term demonstrates how the time rate of change of the mass flux over a bounding surface contributes to the far-field noise. Also it is important to note that the time derivative can effectively be moved into or out of the integrand if R and f are some analytic function, or not a function of time.

For the two other terms, the derivatives of delta functions require integrating by parts. The process for the dipole or loading terms start with the integral form as

$$p'_d(\mathbf{x},t) = -\int_{-\infty}^{\infty}\int_{-\infty}^{\infty} \frac{\partial}{\partial y_i}\left\{L_{ij} n_j \delta(f)\right\} G(\mathbf{x},t|\mathbf{y},\tau)d^3\mathbf{y}\ d\tau. \tag{2.56}$$

Integration by parts for each y_i leads to,

$$p'_d(\mathbf{x},t) = \frac{1}{4\pi}\int_{-\infty}^{\infty}\int_{-\infty}^{\infty}\left\{[L_{ij}n_j]\delta(f)\frac{\partial}{\partial y_i}\frac{\delta(t-\tau-\frac{|\mathbf{x}-\mathbf{y}|}{c_0})}{|\mathbf{x}-\mathbf{y}|}\right\}d^3\mathbf{y}\ d\tau$$

since the evaluation of the delta function at the bounds of integration is zero. Furthermore, $\frac{\partial}{\partial y_i}G(\mathbf{x},t|\mathbf{y},\tau) = -\frac{\partial}{\partial x_i}G(\mathbf{x},t|\mathbf{y},\tau)$ which allows for the differential to be removed from the integral and the integration with respect to retarded time τ to be performed to achieve,

$$\begin{aligned} p'_d(\mathbf{x},t) &= -\frac{1}{4\pi}\frac{\partial}{\partial x_i}\int\int_{-\infty}^{\infty}[L_{ij}n_j]\,\delta(f)\frac{\delta(t-\tau-\frac{|\mathbf{x}-\mathbf{y}|}{c_0})}{|\mathbf{x}-\mathbf{y}|}d^3\mathbf{y}d\tau \\ &= -\frac{1}{4\pi}\frac{\partial}{\partial x_i}\int_{-\infty}^{\infty}\left[\frac{L_{ij}n_j}{|\mathbf{x}-\mathbf{y}|}\right]_{ret}dS. \end{aligned} \tag{2.57}$$

This process can be repeated for a point quadrupole as

$$\begin{aligned} p'_q(\mathbf{x},t) &= \int\int_{-\infty}^{\infty}\frac{\partial^2}{\partial y_i\partial y_j}\left\{T_{ij}H(f)\right\}G(\mathbf{x},t|\mathbf{y},\tau)d^3\mathbf{y}d\tau \\ &= -\int\int_{-\infty}^{\infty}\frac{\partial}{\partial y_i}\left\{T_{ij}H(f)\right\}\frac{\partial}{\partial y_j}G(\mathbf{x},t|\mathbf{y},\tau)d^3\mathbf{y}d\tau \\ &= \frac{1}{4\pi}\int\int_{-\infty}^{\infty}T_{ij}H(f)\frac{\partial^2}{\partial x_i\partial x_j}\left(\frac{\delta(t-\tau-\frac{|\mathbf{x}-\mathbf{y}|}{c_0})}{|\mathbf{x}-\mathbf{y}|}\right)d^3\mathbf{y}d\tau \\ &= \frac{1}{4\pi}\frac{\partial^2}{\partial x_i\partial x_j}\int_{V_{ext}}\left[\frac{T_{ij}}{|\mathbf{x}-\mathbf{y}|}\right]_{ret}dV. \end{aligned} \tag{2.58}$$

Collecting all of the individual integral expressions,

$$\begin{aligned} p'(\mathbf{x},t) &= p'_m(\mathbf{x},t) + p'_d(\mathbf{x},t) + p'_q(\mathbf{x},t) \\ &= \frac{1}{4\pi}\frac{\partial}{\partial t}\int\left[\frac{Q_in_i}{|\mathbf{x}-\mathbf{y}|}\right]_{ret}dS - \frac{1}{4\pi}\frac{\partial}{\partial x_i}\int\left[\frac{L_{ij}n_j}{|\mathbf{x}-\mathbf{y}|}\right]_{ret}dS \\ &+ \frac{1}{4\pi}\frac{\partial^2}{\partial x_i\partial x_j}\int_{V_{ext}}\left[\frac{T_{ij}}{|\mathbf{x}-\mathbf{y}|}\right]_{ret}dV. \end{aligned} \tag{2.59}$$

2.2.2 Far Field approximation

The evaluation of the sound in the far field from the retarded time equations requires further approximation. Under the assumption that the source region is small with

respect to an acoustic wavelength, i.e. compact, and is therefore only a function of $\mathbf{y}, \tau$ such that as $|\mathbf{x}| \to \infty$ one concludes that $|\mathbf{x}| \gg |\mathbf{y}|$. This means the far field expansion is based on

$$|\mathbf{x}-\mathbf{y}| \equiv (|\mathbf{x}|^2 - 2\mathbf{x}\cdot\mathbf{y} + |\mathbf{y}|^2)^{\frac{1}{2}} = |\mathbf{x}|\left(1 - \frac{2\mathbf{x}\cdot\mathbf{y}}{|\mathbf{x}|^2} + \frac{|\mathbf{y}|^2}{|\mathbf{x}|^2}\right)^{\frac{1}{2}}$$
$$\approx |\mathbf{x}|\left\{1 - \frac{\mathbf{x}\cdot\mathbf{y}}{|\mathbf{x}|^2} + \mathcal{O}\left(\frac{|\mathbf{y}|^2}{|\mathbf{x}|^2}\right)\right\}.$$

So the approximation becomes

$$|\mathbf{x}-\mathbf{y}| \approx |\mathbf{x}| - \frac{\mathbf{x}\cdot\mathbf{y}}{|\mathbf{x}|} \quad \text{when } \frac{\mathbf{y}}{\mathbf{x}} \ll 1. \tag{2.60}$$

Also under this assumption,

$$\frac{1}{|\mathbf{x}-\mathbf{y}|} \approx \frac{1}{|\mathbf{x}| - \frac{\mathbf{x}\cdot\mathbf{y}}{|\mathbf{x}|}} \approx \frac{1}{|\mathbf{x}|}\left(1 + \frac{\mathbf{x}\cdot\mathbf{y}}{|\mathbf{x}|^2}\right)$$

Therefore,

$$\frac{1}{|\mathbf{x}-\mathbf{y}|} \approx \frac{1}{|\mathbf{x}|} + \frac{\mathbf{x}\cdot\mathbf{y}}{|\mathbf{x}|^3} \quad \text{when } \frac{|\mathbf{y}|}{|\mathbf{x}|} \ll 1. \tag{2.61}$$

Using this approximation, 2.61, demonstrates how the sound decays as $1/r = 1/\mathbf{x}$ from the source. However, if one wants to invoke the Fraunhofer approximation to retain possible phase difference based interference within the source region, then the first two leading terms of 2.60 are retained inside the integrand describing the source locations for the Green's function as shown by [22]. Finally, by applying the Fraunhofer approximation to equation 2.59,

$$\begin{aligned} p'(\mathbf{x},t) &= \frac{1}{4\pi}\left\{\frac{\partial}{\partial t}\int \frac{1}{|\mathbf{x}|}\left[Q_i\left(\mathbf{y}, t - \frac{|\mathbf{x}|}{c_0} + \frac{\mathbf{x}\cdot\mathbf{y}}{c_0|\mathbf{x}|}\right)n_i\right]dS\right. \\ &- \frac{\partial}{\partial x_i}\int \frac{1}{|\mathbf{x}|}\left[L_{ij}\left(\mathbf{y}, t - \frac{|\mathbf{x}|}{c_0} + \frac{\mathbf{x}\cdot\mathbf{y}}{c_0|\mathbf{x}|}\right)n_j\right]dS \\ &+ \left.\frac{\partial^2}{\partial x_i \partial x_j}\int_{V_{ext}} \frac{1}{|\mathbf{x}|}\left[T_{ij}\left(\mathbf{y}, t - \frac{|\mathbf{x}|}{c_0} + \frac{\mathbf{x}\cdot\mathbf{y}}{c_0|\mathbf{x}|}\right)\right]dV\right\} \end{aligned} \tag{2.62}$$

To further simplify equation 2.62, it is possible to replace the differential operator $\frac{\partial}{\partial x_j}$ with time derivatives like $\frac{\partial}{\partial t}$. This is accomplished with the observation that for an

arbitrary source q_j,

$$\begin{aligned}
\frac{\partial q_j}{\partial x_j} &\equiv \frac{\partial q_j}{\partial x_j}\left(\mathbf{y}, t - \frac{|\mathbf{x}|}{c_0} + \frac{\mathbf{x}\cdot\mathbf{y}}{c_0|\mathbf{x}|}\right) \\
&= \frac{\partial q_j}{\partial t}\left(\mathbf{y}, t - \frac{|\mathbf{x}|}{c_0} + \frac{\mathbf{x}\cdot\mathbf{y}}{c_0|\mathbf{x}|}\right)\frac{\partial}{\partial x_j}\left(t - \frac{|\mathbf{x}|}{c_0} + \frac{\mathbf{x}\cdot\mathbf{y}}{c_0|\mathbf{x}|}\right) \\
&= \frac{\partial q_j}{\partial t}\left(\mathbf{y}, t - \frac{|\mathbf{x}|}{c_0} + \frac{\mathbf{x}\cdot\mathbf{y}}{c_0|\mathbf{x}|}\right)\left(-\frac{x_j}{c_0|\mathbf{x}|} + \frac{y_j}{c_0|\mathbf{x}|} + \frac{(\mathbf{x}\cdot\mathbf{y})x_j}{c_0|\mathbf{x}|^3}\right) \\
&\approx -\frac{x_j}{c_0|\mathbf{x}|}\frac{\partial q_j}{\partial t}\left(\mathbf{y}, t - \frac{|\mathbf{x}|}{c_0} + \frac{\mathbf{x}\cdot\mathbf{y}}{c_0|\mathbf{x}|}\right) \text{ as } |\mathbf{x}| \to \infty. \qquad (2.63)
\end{aligned}$$

The $1/|\mathbf{x}|$ dependence is maintained because $x_j/|\mathbf{x}|$ is the j^{th} component of the unit vector $\mathbf{x}/|\mathbf{x}|$ which does not effect the decay rate but does effect directivity. The y_j term is assumed small and if we neglect the near field that means we assume the third term to be small. We have thus shown Howe's [22] equation 1.9.7,

$$\frac{\partial}{\partial x_j} \leftrightarrow -\frac{1}{c_0}\frac{x_j}{|\mathbf{x}|}\frac{\partial}{\partial t} \qquad (2.64)$$

which when applied to 2.62 yields,

$$\begin{aligned}
p'(\mathbf{x}, t) &= \frac{1}{4\pi|\mathbf{x}|}\frac{\partial}{\partial t}\int Q_i\left(\mathbf{y}, t - \frac{|\mathbf{x}|}{c_0} + \frac{\mathbf{x}\cdot\mathbf{y}}{c_0|\mathbf{x}|}\right) n_i dS \\
&- \frac{x_i}{4\pi c_0|\mathbf{x}|^2}\frac{\partial}{\partial t}\int L_{ij}\left(\mathbf{y}, t - \frac{|\mathbf{x}|}{c_0} + \frac{\mathbf{x}\cdot\mathbf{y}}{c_0|\mathbf{x}|}\right) n_j dS \\
&+ \frac{x_i x_j}{4\pi c_0^2|\mathbf{x}|^3}\frac{\partial^2}{\partial t^2}\int_{V_{ext}} T_{ij}\left(\mathbf{y}, t - \frac{|\mathbf{x}|}{c_0} + \frac{\mathbf{x}\cdot\mathbf{y}}{c_0|\mathbf{x}|}\right) dV. \qquad (2.65)
\end{aligned}$$

These equations represent the far-field approximations. The acoustic analogy code retains these and the next highest order terms which decay like $1/|\mathbf{x}|^2$ and represent the effects of the near-field acoustics. This leads to the equation which is implemented

in the code,

$$
\begin{aligned}
p'(\mathbf{x},t) &= \frac{1}{4\pi|\mathbf{x}|}\frac{\partial}{\partial t}\int Q_i\left(\mathbf{y},t-\frac{|\mathbf{x}|}{c_0}+\frac{\mathbf{x}\cdot\mathbf{y}}{c_0|\mathbf{x}|}\right)n_i dS \\
&+ \frac{\mathbf{x}\cdot\mathbf{y}}{4\pi|\mathbf{x}|^3}\frac{\partial}{\partial t}\int Q_i\left(\mathbf{y},t-\frac{|\mathbf{x}|}{c_0}+\frac{\mathbf{x}\cdot\mathbf{y}}{c_0|\mathbf{x}|}\right)n_i dS \\
&+ \frac{x_i}{4\pi c_0|\mathbf{x}|^2}\frac{\partial}{\partial t}\int L_{ij}\left(\mathbf{y},t-\frac{|\mathbf{x}|}{c_0}+\frac{\mathbf{x}\cdot\mathbf{y}}{c_0|\mathbf{x}|}\right)n_j dS \\
&- \frac{(\mathbf{x}\cdot\mathbf{y})x_i}{4\pi c_0|\mathbf{x}|^2}\frac{\partial}{\partial t}\int L_{ij}\left(\mathbf{y},t-\frac{|\mathbf{x}|}{c_0}+\frac{\mathbf{x}\cdot\mathbf{y}}{c_0|\mathbf{x}|}\right)n_j dS \\
&+ \frac{x_i x_j}{4\pi c_0^2|\mathbf{x}|^3}\frac{\partial^2}{\partial t^2}\int_{V_{ext}} T_{ij}\left(\mathbf{y},t-\frac{|\mathbf{x}|}{c_0}+\frac{\mathbf{x}\cdot\mathbf{y}}{c_0|\mathbf{x}|}\right)dV \qquad (2.66) \\
&- \frac{(\mathbf{x}\cdot\mathbf{y})x_i x_j}{4\pi c_0^2|\mathbf{x}|^5}\frac{\partial^2}{\partial t^2}\int_{V_{ext}} T_{ij}\left(\mathbf{y},t-\frac{|\mathbf{x}|}{c_0}+\frac{\mathbf{x}\cdot\mathbf{y}}{c_0|\mathbf{x}|}\right)dV. \qquad (2.67)
\end{aligned}
$$

2.2.3 FWH implementation

In order to compute the noise, either a small set of positions or times must be fixed in order to choose a large set of the other. If a small set of positions are specified then a large and temporally well resolved time bracket is specified for each location. These points, usually specified along an arc or a circle encompassing the most important source region gives the directivity by resolving the received sound intensities. Directivity plots are ones in which the acoustic intensity, p_{rms}, or sound pressure level is plotted as the radius and the physical angle of the position is used to set the angle in a polar plot. If instead a small set of times are specified then the sound field can be visualized by computing the the noise for a large set of locations points. In this way the sound field can be visualized.

The implementation of equation 2.67 depends on specifying integration surfaces and volumes. The FWH surfaces are prescribed on background unstructured grids, which makes arbitrary surface extraction within the computational domain challenging. We define arbitrary surfaces and discretize the surface in a manner that reflects the volume grid in the interior. We accomplish this by projecting the centroids of the volume grid on the FWH surface and then generate a constrained Delaunay triangulation for the connectivity while its mesh dual, the Voronoi diagram capped by the boundary, provides the projected face areas. Finally, we establish exterior and interior volumes which allow for surface integration to be handled in tandem with consistent volume integration.

Alternatively, all faces which intersect the desired surface can be used to represent the surface, but discontinuous normals, large numbers of faces, and highly discontinuous volume representations present their own unique challenges and this is our non-standard backup. Our spatial decomposition ensures that a projected partner separated by a fixed distance in a fixed normal direction exists between any two extraction stations. This process is described in detail in appendix B.

The surface integrals are handled independently from the volume terms. For the surface terms there are two options for processing; either at runtime or post processing. The density, pressure, and fluctuating velocities, $v' = v_{tot} - v_{bar}$, are either written to a file to be post-processed or integrated at runtime. The Reynolds' stress, compressive, and viscous stress tensor are computed each timestep and integrated over the specified volumes, set to encompass all important sound sources. These volumes usually contain too much data to be written to data files for post-processing and as a result the computed noise must be computed at runtime. Linear interpolation is used to map runtime onto either the time bracket or spatial bracket.

The implementation of these equations is such that either the compressible or incompressible CFD solvers can be used to compute the noise.

2.3 Initial tests of the FWH solver

In order to test the implementation of our FWH implementation, standard test cases with the three basic polar expansions represented in the FWH equations are tested. These cases with relative motion are also tested and the important steps in deriving the mean background FWH equations are shown in appendix A which also includes important notation.

2.3.1 Point monopoles

A monopole source is physically represented by a pulsating sphere with mass displacement and is represented mathematically by $q(t)\delta(\mathbf{x})$ where $q(t)$ is the source strength. The velocity potential wave equation is

$$\left(\frac{1}{c_0^2}\frac{\partial^2}{\partial t^2} - \nabla^2\right)\varphi = -q(t)\delta(\mathbf{x}). \tag{2.68}$$

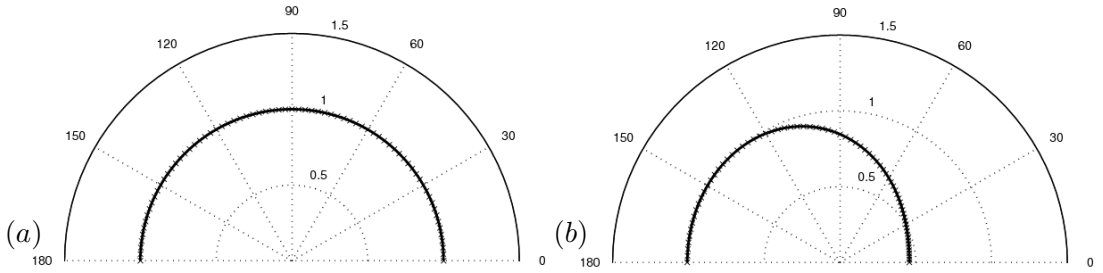

Figure 2.1: Noise recovered at $r = 340$ from a point monopole located at the origin at (a) $M = 0$, (b) $M = 0.5$. (–) exact solution, (x) computed solution.

This leads to the solution,

$$\varphi(\mathbf{x}, t) = \frac{-q(t - \frac{|\mathbf{x}|}{c_0})}{4\pi|\mathbf{x}|}, \tag{2.69}$$

where for incompressible fluid there is no retarded time effect. Lockard [36] describes the monopole velocity potential as a simple harmonic oscillator,

$$\varphi(\mathbf{x}, t) = \frac{q}{4\pi R*} \exp(iw(t - R/c_0)) \tag{2.70}$$

with source strength q. The induced pressure is then calculated as,

$$p'(\mathbf{x}, t) = -\rho_o \frac{\partial}{\partial t}\varphi. \tag{2.71}$$

The noise received from a point monopole 340 radii away using our FWH solver is shown in figure 2.1 (a) compared to equation 2.71.

The velocity potential which describes noise from a point monopole in a mean background fluid is

$$\varphi(\mathbf{x}, t) = \frac{-q(t - \frac{R}{c_0})}{4\pi R*}, \tag{2.72}$$

where R and $R*$ are the physical and acoustic distances respectively shown in chapter 3. The induced pressure is then solved to be

$$p'(\mathbf{x}, t) = -\rho_o \left[\frac{\partial}{\partial t} + U_0 \frac{\partial}{\partial x_1}\right] \varphi. \tag{2.73}$$

This is compared to the noise received from our FWH solver in a moving medium at $M = 0.5$ as shown in figure 2.1 (b).

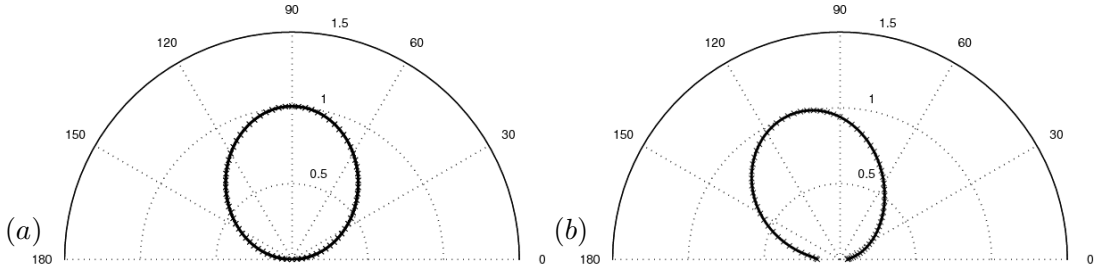

Figure 2.2: Noise recovered at $r = 340$ from a x_2 or y distributed point dipole located at the origin at (a) $M = 0$, (b) $M = 0.5$. (–) exact solution, (x) computed solution.

2.3.2 Point dipoles

An oscillating cylinder is a physical representation of point dipole. It is mathematically described by a source vector which is a function of time $f(t)$ then the forcing function becomes $div(f(t)\delta(\mathbf{x})) = \frac{\partial}{\partial x_j}(f_i(t)\delta(\mathbf{x}))$, meaning a time varying force at the origin. This leads to the pressure equation,

$$p(\mathbf{x}, t) = \frac{\partial}{\partial x_j}\left(\frac{f_j(\mathbf{y}, t - \frac{|\mathbf{x}|}{c_0})}{4\pi|\mathbf{x}|}\right). \tag{2.74}$$

The convected wave solution is obtained by the inclusion of the convected Greens function switching distances $|\mathbf{x}|$ to the acoustic and physical distances obtained similarly for the point monopole case. The results for two different Mach numbers for a dipole oriented along the x_2 axis are shown in figure 2.2.

2.3.3 Point quadrupole

A pair of oscillating cylinders or four monopoles whose net volume source strength is zero is the physical represention of a point quadrupole. Its mathematical description source function is $\frac{\partial^2 T_{ij}}{\partial x_i \partial x_j}(\mathbf{x}, t)$ and leads to an induced pressure of

$$p(\mathbf{x}, t) = \frac{1}{4\pi}\frac{\partial^2}{\partial x_i \partial x_j}\left(\frac{T_{ij}(\mathbf{y}, t - |\mathbf{x}|/c_0)}{|\mathbf{x}|}\right). \tag{2.75}$$

The convected equation is obtained by supplanting the distance functions with R and R^*. The quadrupole chosen is in the x_1, x_2 direction since it produces the characteristic clover-leaf shape in the $x-y$ plane. The case of the stationary and convected quadrupole

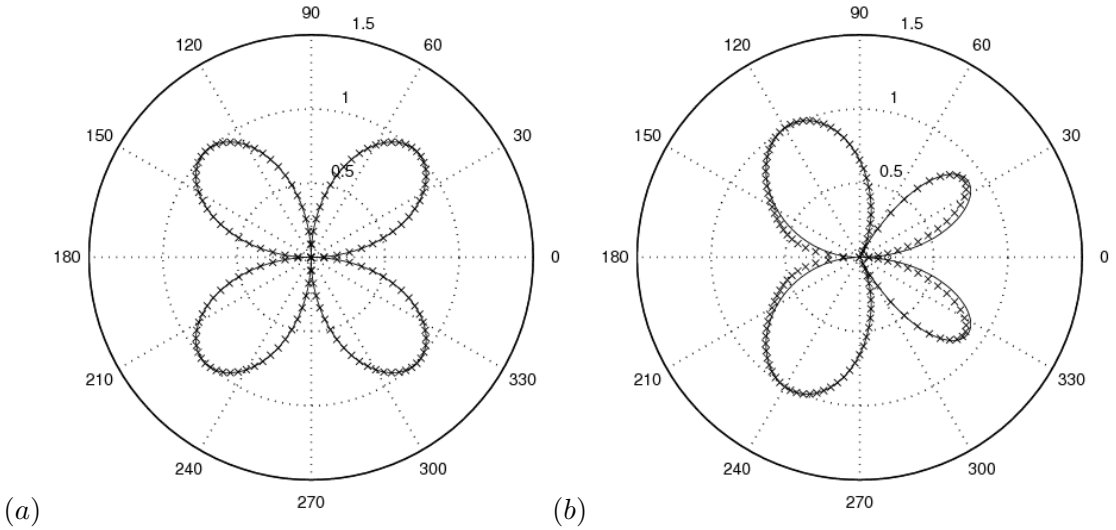

(a) (b)

Figure 2.3: Noise recovered at $r = 340$ from a x_1, x_2 point quadrupole located at the origin at (a) $M = 0$, (b) $M = 0.5$. (–) exact solution, (x) computed solution.

are shown in figure 2.3. The slight disagreement for the convected quadrupole case in figure 2.3 (b) is associated with grid resolution. As the grid resolution increases this discrepancy diminished.

Chapter 3

Dynamic endcap closure model for flows with mean convection

3.1 'End cap' problem

As undamped fluctuating pressure and momentum, which act as acoustic sources, travel across porous FWH planes they can produce a discrete spike unless they are handled by the inclusion of volume terms in the FWH formulation. The volume term can be computationally expensive to retain, and difficult to compute. A related problem is the choice of Greens' function which dictates propagation exterior to the bounding surface. If the porous surface is near or at the physical surface the Greens' function should account for the geometry; if it is sufficiently far away, a free space Greens function may be assumed but handling volume terms become important.

This problem with undamped sources crossing the porous FWH or leaving the domain poses what is termed as the 'end cap' or closure problem. Like the surface terms when an undamped acoustic source exits the zone of integration, there will be a discrete spike in the received noise for no reason other than the finite size of the domain. An example where surface source terms and volume terms are interrelated and non unique is given in [37]. Furthermore, Ffowcs Williams [38] clearly detailed how surface and volume terms are interrelated and non-linearity is expressed depending on the data surface location. The surface terms end up directly relating to the volume terms and vice-versa in that if an uncorrected error occurs in one term it can be rearranged to instead appear

in the other. A variety of approaches are used to appropriately close the integration boundary or correct the porous surface terms (figure 3.1). The first approach is to ignore the volume term by assuming it to be small and instead only use the physical surfaces where penetrating sound sources do not exist. The next approach is to not enclose the back of domain where the problem is manifest, e.g. wake of bluff body, while including other faces of the porous surface. This approach under predicts the noise in radiation directions that are bounded by the normals of the missing surface. The third approach is phase averaging of the noise contributions over a series of exit plane as suggested by Shur et al. [1]. The idea is that if there are enough well-spaced planes the error at each station should be phased shifted relative to the others and that by averaging the complex signal, the average should have lower overall error.

We develop a methodology for end cap correction that uses corrected volume terms, along with multiple exit planes to dynamically calculate correction parameters to appropriately cap surface terms. In addition the proposed method allows efficient computation of the volume terms, querying of independent volumes, is insensitive to to the location of the end cap planes, and is more accurate than the previously discussed approaches. The proposed approach is based on the concept of multiple exit planes over which the flux of quadrupole terms are subtracted and correlated. The exit flux concept was first suggested by Wang et al. [39] in the context of the volume terms with the Lighthill equations and a fixed empirical velocity at the exit of the computational domain in order to deal with spurious, undamped volume noise. Here, we apply it in the context of the FWH methodology specifically as a correction for porous surfaces in the near field along with a dynamic approach to compute the convection velocity by correlating the source terms over multiple planes. Section 3.2 describes the proposed dynamic methodology for end cap correction and evaluates its promise by applying it to a two–dimensional vortex advecting across a FWH porous surface. This is followed by simulations of the flow around circular cylinders, and computation of the emitted far–field noise.

3.2 Methodology for end cap correction

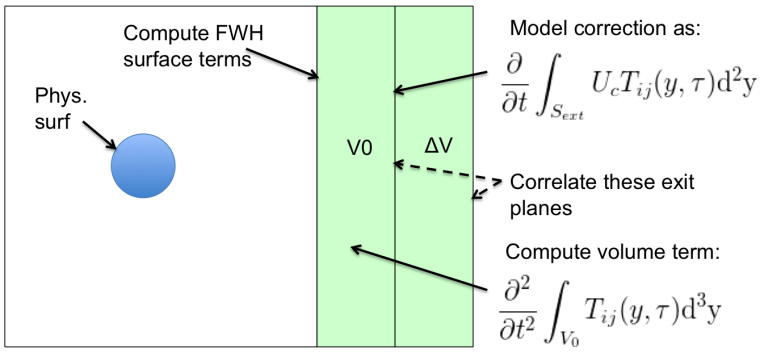

Figure 3.1: Schematic representation of the proposed end cap method.

3.2.1 Basic idea

Figure 3.1 shows a schematic of a FWH porous surface wrapped around a sound source with end cap planes adjacent to one end of the surface. Consider the two volumes V_0 and $V_0 + \Delta V$ that extend exterior to the porous surface. Assume the existence of a background velocity U_c which convects sources over the two differential volumes. A truncation error, E_{ij}, is generated as the source exits each volume. Assuming the sources are largely unchanged across ΔV implies that the truncation error is also unchanged. This means that the differential distance Δy_1 corresponds to a time difference $\Delta\tau = \frac{\Delta y_1}{U_c}$ for the error to be received at a microphone position from each volume. Expressing this error in the first derivative of the volume terms $\dot{T}_{ij}$ and Taylor series expanding yields,

$$\dot{T}^{\pm}_{ij} = \dot{T}_{ij} + E_{ij}[t \mp \Delta/2] \tag{3.1}$$

$$\ddot{T}^{+}_{ij} \approx \frac{1}{2}\left(\ddot{T}^{+}_{ij} + \ddot{T}^{-}_{ij}\right) + \frac{1}{\Delta\tau}\left(\dot{T}^{+}_{ij} + \dot{T}^{-}_{ij}\right) \tag{3.2}$$

between the larger $(+)$ volume and the smaller $(-)$ volumes. Expressing this in integral form for the total volume noise,

$$\ddot{T}_{ij}(t) = \frac{\partial^2}{\partial t^2}\int_{V_0} T_{ij}(y,\tau)\mathrm{dy}^3 + \frac{\partial}{\partial t}\int_{S_{ext}} U_c T_{ij}(y,\tau)\mathrm{dy}^2. \tag{3.3}$$

The corrective flux $\frac{\partial}{\partial t}\int_{S_{ext}} U_c T_{ij}(y,\tau)\mathrm{dy}^2$ is applied at the exit surface of the bounding volume in order to approximate the missing sources exterior to the surface of integration.

The proposed scheme assumes that the primary cause of the error is due to the convection of a truncation error over a finite domain captured only on the porous FWH

surface. This is eliminated by the inclusion of the volume term which is accurately corrected at its truncation location. This means that the corrected volume term is used as the correction to the finite size FWH terms. Furthermore, we dynamically calculate the model constant, U_c, by correlating the the correction term over subsequent exit planes. The first step is finding a pair of related exit surface elements, indexed as j and k, through a ray tracing routine based on the dot product of the total velocity with the element normal $\hat{n}_k$. The distance between the elements $dx_{j,k}$ establishes a correlation function based on the corrective flux to compute U_c as

$$U_c = \sum_{j=0,k=0}^{N_j,N_k} \frac{dx_{j,k} \cdot \hat{n}_k}{max(\frac{\beta(t)\hat{R}_{xy}(m)}{N})dt}, \tag{3.4}$$

The multiplying factor $\beta(t)$ is a windowing function in time which ensures only one maximum correlation over any given averaging period. This is then averaged to obtain the average convection velocity between any two surfaces. It is important to note that in the correlation function,

$$\hat{R}_{xy}(m) = \begin{cases} \sum_{n=0}^{N-m-1} \alpha x_{n+m}\ y_n^* & m \geq 0 \\ \\ \hat{R}_{xy}^*(-m) & m < 0 \end{cases}, \tag{3.5}$$

an optional multiplying term α allows to normalize the signal's strength before the correlation to account for decay in the signal over longer separation distances; a small separation is therefore preferable for highest correlation. For very small separations and using all of the time history one sets $\alpha = \beta(t) = 1$ and recovers the time averaged spatially varying convection velocity which means that the convection velocity can easily be a function of space and/or time i.e. $U_c = U_c(\vec{y}, t)$. Also, it can be computed during run time or in a post processing routine. Obtaining the convection velocity via correlation as opposed to from the time–averaged flow–field ensures its application to non–stationary problems and situations such as gusting inflow and curved bounding surfaces.

3.2.2 Application to potential vortex

The proposed correction is analytically evaluated for the case of an inviscid, incompressible potential vortex initially centered at $(y_1, y_2) = (0, 0)$ superimposed on a uniform

background velocity U_c. The speed of sound is fixed at $340m/s$ and the Mach number is chosen to be $M = 0.1$ which implies $U_c = 34m/s$. The circulation of the vortex is chosen to be $\Gamma = \pi U_c/100$ to ensure small perturbation. The velocity potential is,

$$\begin{aligned} \phi(y,\tau) &= U_c\, x - \frac{\Gamma\theta}{2\pi} \\ \theta &= tan^{-1}(\tilde{y_2}/\tilde{y_1}) \\ \tilde{y_1} &= y_1 - U_c\tau \\ \tilde{y_2} &= y_2 \end{aligned}$$

The velocities are derived from the potential and the pressure is calculated from the non-linear unsteady Bernoulli equation as,

$$\begin{aligned} u(y,\tau) &= U_c + \frac{\Gamma}{2\pi r} sin(\theta) \\ v(y,\tau) &= \frac{-\Gamma}{2\pi r} cos(\theta) \\ p(y,\tau) &= p_0 - \frac{\rho\Gamma^2}{8\pi^2 r^2} \end{aligned}$$

where r and θ are measured with respect to the center of the moving vortex. Given that the background pressure is $p_0 = p_\infty - \rho_0 U_c^2/2$, note that the unsteady Bernoulli term cancels with the cross velocity term leading to the given pressure. The microphone location is at 75D downstream since assumptions of compactness and symmetry result in no variation with respect to y in the predicted acoustic pressure. Ten exit planes are used to correlate and provide correction for surfaces terms as shown in figure 3.2. The incompressibility of the flow-field means that the monopole term is zero clearly shown in equation 2.67 since the time rate of change of the integral of the mass flux is zero.

This setup demonstrates the canonical problem that the end cap methodology is designed to solve, and provides a good test because there is no time varying acoustic pressure; $p_{ac}(x,t) = p_\infty - \rho_0 \left(\frac{\partial\phi}{\partial\tau} + U_c \frac{\partial\phi}{\partial x_1}\right) = p_\infty - \rho_0 U_c^2 \rightarrow p'_{ac} = 0$. The acoustic pressure is the linear solution to the the governing wave equation. Therefore any signal from the surfaces or volumes are erroneous and must be balanced by the correction. Here the momentum flux in the dipole term in equation 2.67 becomes the largest source with the passage of the vortex core. This is balanced by the creation of volume noise as the vortex completes its passage. This is expected since the volume term is related to the surface term for a fixed surface in the convected frame of reference as,

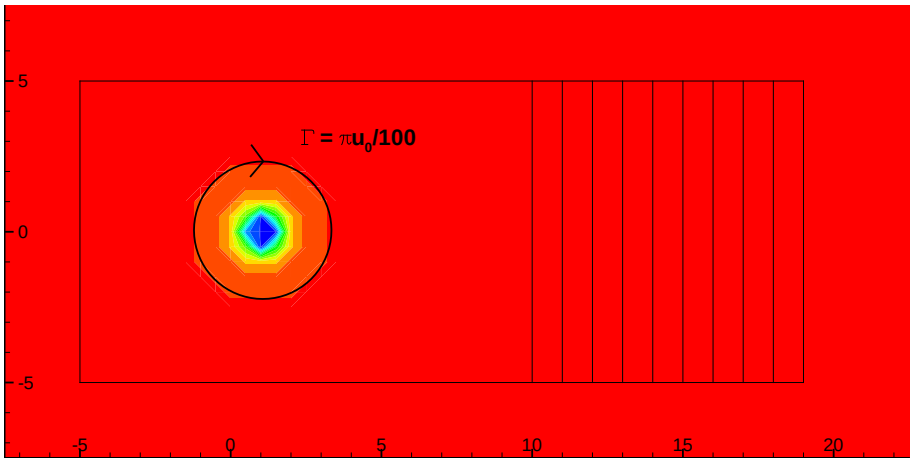

Figure 3.2: The center of the vortex is visualized with the pressure field along with the Ffowcs-Williams and Hawkings planes and exit surfaces.

$$T_{ij} = L_{ij} - \rho u_i U_{cj} - c_0^2(\rho - \rho_0)\delta_{ij}.$$

Assuming $\rho = \rho_0$ leads to time derivatives as,

$$\begin{aligned} \dot{T_{ij}} &= \dot{L_{ij}} - \rho \frac{\partial u_i}{\partial \tau} U_{cj} \\ \ddot{T_{ij}} &= \frac{\partial}{\partial \tau} \dot{L_{ij}} - \rho \frac{\partial^2 u_i}{\partial \tau^2} U_{cj}. \end{aligned}$$

Therefore, the volume term is the time rate of change of the surface term subtracted by the second derivative of the fluctuating velocity multiplied by a mean background velocity. Furthermore, since the volume noise production in ΔV is often negligible, only the passage of the vortex into and out of the volume domain becomes important, to avoid truncation errors. This interpretation therefore demonstrates how convective sources of truncation error from surface terms are related to the corrected volume terms. In the simplified case of the convected vortex, the monopole term is zero because of incompressibility and the integrals of the derivatives of u-velocity are zero because of symmetry which leads to the expression,

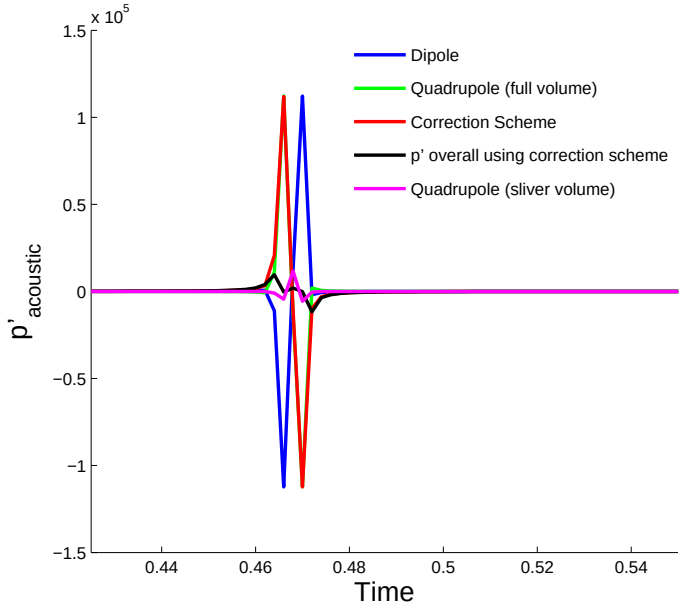

Figure 3.3: The acoustic pressure for the vortex problem obtained from the FWH equations demonstrate how the corrected volume term removes spurious noise components. The microphone location is 75D downstream. The methods compared include the method discussed as well as a FWH approach where an extended volume computational region extends far downstream of the data surface.

$$\begin{aligned} p'_{All} &= \frac{1}{c_0 R^*}\int_S \dot{L_{ij}} n_j \mathrm{dS} + \frac{M_0}{c_0 R^*}\int_{S_{ext}} \dot{T_{ij}} n_j \mathrm{dS} + \frac{1}{c_0^2 R^*}\int_V \ddot{T_{ij}} \mathrm{d^3y} \\ &= \frac{1}{c_0 R^*}\int_S \dot{L_{ij}} n_j \mathrm{dS} + \frac{M_0}{c_0 R^*}\int_{S_{ext}} \dot{L_{ij}} n_j \mathrm{dS} + \frac{1}{c_0^2 R^*}\int_V \ddot{T_{ij}} \mathrm{d^3y} \\ &= \frac{1+M_0}{c_0 R^*}\int_S \dot{L_{ij}} n_j \mathrm{dS} + \frac{1}{c_0^2 R^*}\int_V \ddot{L_{ij}} \mathrm{d^3y}. \end{aligned}$$

This equation assumes a directly downstream microphone location and that the exit surface of the infinitesimal volume is near the FWH data surface. Mitigation of the error is accomplished as a result of a convective derivative type term of the surface forces being offset by the volume term. This is the mechanism which corrects convective type truncation errors when handled completely. This is shown in figure 3.3 where the surface and corrected volume terms are shown as a function of time; note their cancellation.

To examine this effect, the various terms in the FWH equations are computed analytically in the moving frame of reference using the convected Greens function similar to [40]. The convected wave form of the FWH equations and the modified Greens function are

$$\diamond^2 = \frac{1}{c_0^2}\frac{\partial^2}{\partial t^2} - \frac{\partial^2}{\partial x_j \partial x_j} + \frac{2M_{0j}}{c_0}\frac{\partial^2}{\partial t \partial x_j} + M_{0i}M_{0j}\frac{\partial^2}{\partial x_i \partial x_j} \tag{3.6}$$

$$\diamond^2[H(f)p'] = \left(\frac{\partial}{\partial t} + U_{cj}\frac{\partial}{\partial x_j}\right)[Q_k n_k \delta(f)] - \frac{\partial}{\partial x_i}[L_{ij} n_j \delta(f)] + \frac{\partial^2}{\partial x_i \partial x_j}[H(f)T_{ij}] \tag{3.7}$$

$$G(\mathbf{x},\mathbf{y},t-\tau) = \frac{1}{4\pi R^*}\delta\left(t-\tau-\frac{R}{c_0}\right) \tag{3.8}$$

where the distance metrics for the convected wave case are

$$\begin{aligned} R &= \frac{1}{\beta^2}(R^* - M_0(x_1 - y_1)) \\ R^* &= \sqrt{(x_1-y_1)^2 + \beta^2[(x_2-y_2)^2 + (x_3-y_3)^2]} \\ \beta^2 &= 1 - M_0^2 \end{aligned}$$

which means

$$\widetilde{R}_i = \frac{\partial R}{\partial x_i} \Rightarrow \widetilde{R}_1 = \frac{1}{\beta^2}(\widetilde{R}_1^* - M_0), \widetilde{R}_2 = \frac{(x_2-y_2)}{R^*}, \widetilde{R}_3 = \frac{(x_3-y_3)}{R^*}$$
$$\widetilde{R}_i^* = \frac{\partial R^*}{\partial x_i} \Rightarrow \widetilde{R}_1^* = \frac{(x_1-y_1)}{R^*}, \widetilde{R}_2^* = \beta^2\frac{(x_2-y_2)}{R^*}, \widetilde{R}_3^* = \beta^2\frac{(x_3-y_3)}{R^*}.$$

The time derivatives are brought into the integrand as discussed in appendix A, as the Leibnitz terms vanish and the chain rule is applied to the FWH equations. Compatible results were obtained by either the approach of retaining the exterior derivatives or moving them into the integrand. In the chosen wind tunnel frame of reference, the source, observer, and data surface do not move as a function of time which means $v_i = 0$ and any dot products of normals or distance metrics are also zero which simplifies the equations. Also the mean background velocity is fixed and expressed by $U_c = 34m/s$.

The FWH equations, expressed in the wind tunnel frame, have the thickness, $p'_T = 0$ because of incompressibility, loading, p'_L, quadrupole, p'_Q, and correction, $p'_{Q_{cor}}$, terms as,

$$4\pi p'_L = \int_S \left[\frac{\widetilde{R_i}}{c_0 R^*}\dot{L_{ij}}\right] \mathrm{dS}, \quad 4\pi p'_Q = \int \left[\frac{\widetilde{R_i}\widetilde{R_j}}{c_0^2 R^*}\ddot{T_{ij}}\right] \mathrm{d^3y}, \quad 4\pi p'_{Qcor} = \int_{S_{ext}} \left[\frac{M\widetilde{R_i}\widetilde{R_j}}{c_0 R^*}\dot{T_{ij}}\right] \mathrm{dS}$$

where

$$\begin{aligned} \dot{L_{ij}} &= \rho\frac{\partial u_i}{\partial\tau}(u_j + U_{cj}) + \rho u_i\frac{\partial u_j}{\partial\tau} + \frac{\partial p}{\partial\tau}\delta_{ij} \\ \ddot{T_{ij}} &= \rho\big(\frac{\partial^2 u_i}{\partial\tau^2}u_j + 2\frac{\partial u_i}{\partial\tau}\frac{\partial u_j}{\partial\tau} + u_i\frac{\partial^2 u_j}{\partial\tau^2}\big) + \frac{\partial^2 p}{\partial\tau^2}\delta_{ij} \end{aligned}$$

Recall that $U_{c1} = U_c$ and $U_{c2} = 0$. This means that given the derivatives of the field variables gives the complete FWH equations for this case. They are

$$\begin{gathered} \frac{\partial u}{\partial\tau} = \frac{\Gamma U_c}{2\pi r^2}sin(2\theta), \quad \frac{\partial v}{\partial\tau} = \frac{-\Gamma U_c}{2\pi r^2}cos(2\theta), \quad \frac{\partial p}{\partial\tau} = \frac{-\rho\Gamma^2 U_c}{4\pi^2 r^3}cos(\theta) \\ \frac{\partial^2 u}{\partial\tau^2} = \frac{\Gamma U_c^2}{\pi r^3}sin(3\theta), \quad \frac{\partial^2 v}{\partial\tau^2} = -\frac{\Gamma U_c^2}{\pi r^3}cos(3\theta), \quad \frac{\partial^2 p}{\partial\tau^2} = \frac{\rho\Gamma^2 U_c^2}{4\pi^2 r^4}(1 - 4cos^2(\theta)) \end{gathered}$$

which when plugged into the equations for the stress fields simplifies to

$$4\pi p'_{All} = 4\pi\left(p'_L + p'_Q + p'_{Q_{cor}}\right)$$

where,

$$\begin{aligned} p'_L &= \int_S \Big[\frac{\rho M\Gamma}{2\pi r^2 R^*}\Big\{\widetilde{R_1}(U_c sin(2\theta)n_x - \frac{\Gamma}{2\pi r}(cos(3\theta)n_x + sin(3\theta)n_y)) \\ &+ \widetilde{R_2}(-U_c cos(2\theta)n_x - \frac{\Gamma}{2\pi r}(sin(3\theta)n_x - cos(3\theta)n_y))\Big\}\Big]_{ret}\mathrm{dS} \\ p'_Q &= \int_V \Big[\frac{3\rho M^2\Gamma^2}{4\pi^2 r^4 R^*}(-\widetilde{R_1}\widetilde{R_1}cos(4\theta) - 2\widetilde{R_1}\widetilde{R_2}sin(4\theta) + \widetilde{R_2}\widetilde{R_2}cos(4\theta))\Big]_{ret}\mathrm{d^3y} \\ p'_{Q_{cor}} &= \int_{S_{ext}} \Big[\frac{\rho M^2\Gamma^2}{4\pi^2 r^3 R^*}(-\widetilde{R_1}\widetilde{R_1}cos(3\theta) - 2\widetilde{R_1}\widetilde{R_2}sin(3\theta) + \widetilde{R_2}\widetilde{R_2}cos(3\theta))\Big]_{ret}\mathrm{dS}. \end{aligned}$$

Note the cancellation for the simplified cases of having extrusion surfaces aligned in principle directions. For example in the x-direction,

$$\begin{aligned} p'_L &= \frac{-\rho M\Gamma^2}{4\pi^2 R^*}\Big(\int_{S,front/back}\left[\frac{cos(3\theta)n_x}{r^3}\right]\mathrm{dS} + \int_{S,top/bottom}\left[\frac{sin(3\theta)n_y}{r^3}\right]\mathrm{dS}\Big) \\ p'_Q &= \frac{-3\rho M^2\Gamma^2}{4\pi^2 R^*}\int_V\left[\frac{cos(4\theta)}{r^4}\right]\mathrm{d^3y} \\ p'_{Q_{cor}} &= \frac{-\rho M^2\Gamma^2}{4\pi^2 R^*}\int_{S_{ext}}\left[\frac{cos(3\theta)}{r^3}\right]\mathrm{dS}. \end{aligned}$$

Hence under assumptions of compactness,

$$\begin{aligned} p'_{All} &= -\frac{\rho M\Gamma^2}{4\pi^2 R^*}\Big(\int_{S,front}\left[-\frac{cos(3\theta)}{r^3}\right]\mathrm{dS} + \int_{S,back}\left[(1+M)\frac{cos(3\theta)}{r^3}\right]\mathrm{dS} \\ &+ \int_{S,top/bottom}\left[\frac{sin(3\theta)n_y}{r^3}\right]\mathrm{dS} + 3M\int_V\left[\frac{cos(4\theta)}{r^4}\right]\mathrm{d^3y}\Big) \end{aligned} \tag{3.9}$$

Equation 3.9 is numerically integrated at various emission times. The recovered noise from the FWH equations for this flow field is approximately zero, decays quickly away from the vortex center, and exhibits the $(1+M)$ behavior in the surface terms as expected. It is important to note that it is only after the inclusion of the quadrupole correction terms that the cancellation becomes effectively complete. This indicates that the inclusion of the quadrupole term is necessary for the correct changeover of terms as well as the the application of the exit flux correction.

Finally, we demonstrate the ability of the proposed cross-correlation approach to account for a time-varying convection velocity by windowing our correlation function. We choose a top-hat filter of length ten time spaces to ensure smoothness in results based on the chosen dx, U_c, and dt. The resulting cross-correlation coefficients are plotted as a function of time along with the resulting convection velocity as shown in figure 3.4. This clearly demonstrates the ability to handle time varying convection velocities.

3.3 Re=150 cylinder flow validation

The acoustics of low Reynolds' number cylinder flow have been studied by several investigators, e.g.[41], [3], Hardin and Lamkin [42], [43], [44]; also simplified models have

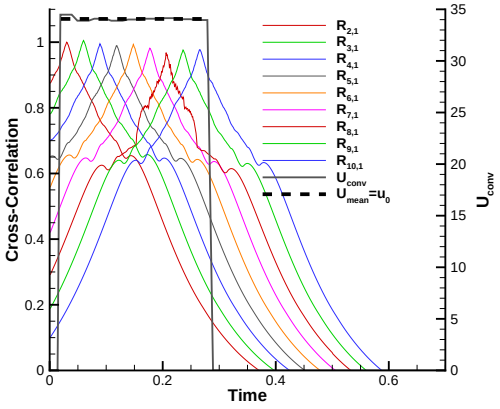

Figure 3.4: The cross-correlation coefficients between each plane with respect to the first plane are shown as well as the convection velocity derived from the method. The mean of the intervals is $U_c = Mc_0 = 34.0$ as specified and is also plotted.

been developed, which render this a good validation problem. Subtle differences in reported results mostly arise from the choice of Greens' function and Doppler shifts but appropriate comparisons can still be made. Phillips constructed a simplified model for Aeolian tones for cylinders and experimented with a $d = 0.0123$cm cylinder over $110 < Re < 160$. For short spans, b, and in-plane observers at distance R and radiation angle θ, Phillips model, with model constant κ, predicts acoustic power $\bar{I}$ given the Strouhal number, St, and flow conditions ρ, V_0, c, and M as

$$\bar{I} = \frac{\kappa^2 St^2 b^2 \rho_0 V_0^6 sin^2\theta}{32 c_0^3 R_0^2 (1 - Mcos\theta)^4} \tag{3.10}$$

Inoue performed computations of a $Re = 150$ cylinder and reported on how Doppler shift is important in the calculation of the two-dimensional acoustic field and how acoustic pressure decays in this configuration. We use a two-dimensional Greens' function to compare to Inoue.

We perform a compressible DNS of the flow around a two-dimensional circular cylinder at $M = 0.2$ and $Re = 150$ with the described FWH acoustic analogy to recover the noise at a distance of 75 and 100D. The compressible results, with an exit sponge, allow for a direct calculation of the noise in the far-field and serves as the basis of comparison for the different methodologies discussed previously. The flow field (lift,drag and basal

Table 3.1: Summary of surface forces and frequencies.

Metric	Result	Norberg
$C_{L,press,max}$	0.2540	0.28
$C_{L,visc,max}$	0.0428	0.045
$C_{D,press,max}$	0.9824	1.00
$C_{D,visc,max}$	0.4046	0.34
$St\ C_L$	0.1646	0.1652
$St\ C_D$	0.3292	0.3304

pressure coefficient) is in good agreement with Inoue and Hatakeyama [3], Beaudan and Moin [45], and Norberg [46], i.e.table 3.1. The Strouhal number agrees with the scaling proposed by Fey et al. [47] of $St = 0.2684 - 1.0356Re^{-0.5} = 0.1648$. The sound comparisons are similarly good. For the sound pressure level (SPL) at a Doppler shifted direction of $\theta = \pi/2$ at $r = 100D$, the Phillips model predicts 87.6dB$\pm$6.02dB based on Phillips' suggested range of $0.5 < k < 2$. Inoue reports a maximum value of 88.5dB and our DNS recovers 89.0dB, all in close agreement. We compare the time histories of the received pressure at this location against Inoue and obtain good agreement as shown in figure 3.5. Also, based on Inoue's scaling arguments for preferential radiation direction $\theta_p = cos^{-1}(M)$ we predict 81 deg which compares well to the predicted maximum of 81.4 deg. These results show that our DNS accurately captures both the flow field and the acoustic field.

Our proposed FWH methodology is used to compute the far-field sound and is compared to DNS at 180 microphone locations at 75D from the cylinder. The data is aggregated via a 2-D FWH implementation that has a porous surface located as fixed planes 5D in front and to the top and bottom of the cylinder. A series of ten exit surfaces are constructed from $x = 5D$ to $7.25D$ downstream of the cylinder. Figure 3.6 evaluates the proposed end cap correction. Note how the correction scheme reduces the maximum value of SPL from 120dB down to 67.204dB in figure 3.6(a). As discussed by Inoue, the expected relative ratio between surface and volume terms is the Mach number, which yields an estimate of 67.574dB. Also, note that with the correction employed the directivity takes on the characteristic quadrupole shape consistent with Gloerfelt et al. [48] or the computations of Hardin and Pope [49]. Figure 3.6(b) illustrates the ability of

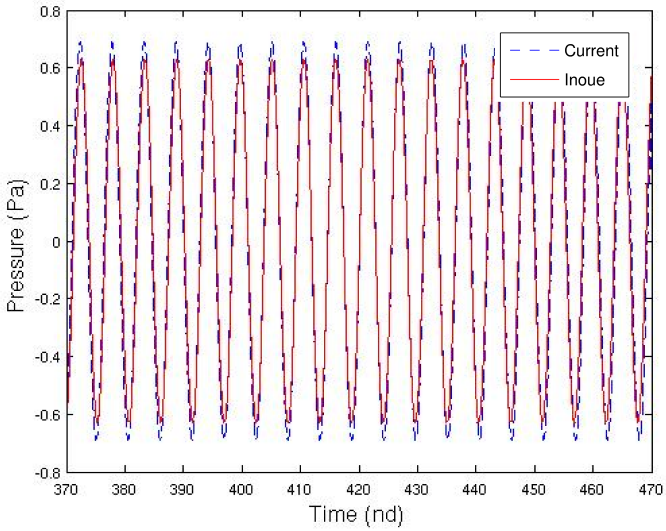

Figure 3.5: For the Re=150 cylinder, a comparison of the time histories of the surface noise is plotted versus Inoue [3] at $\theta = \pi/2$, $R = 100D$.

the dynamic procedure to allow for spatial variation of the convection velocity. Here the convection velocity is assumed to vary across the width of the wake and note how this subtle change provides for diminished off angle errors in the directivity of the quadrupole terms at $f = 2f_0$. This suggests that a fixed convection velocity over-emphasizes the center of the wake in the acoustic analogy. The spatial variation slightly improves the predictions; the improvement depends on the extent of the shear in the wake.

The sensitivity to volume size and the dynamic approach to calculate U_c are examined in figure 3.7. The instantaneous far-field pressure is shown in (a) where the volume noise is calculated for ten volumes each differing by a single grid element dx in the stream-wise direction. Note the scatter in the absence of correction, but when added to the correction for each volume, one recovers the corrected volume noise with less phase and amplitude shifts. Here the convection velocity is externally prescribed. The effect of dynamically computing the convection velocity is shown in (b) where the phase and amplitude variance is significantly reduced if a dynamically calculated U_c is used as opposed to a fixed value. Clearly the phase and amplitude variation decreases across the ten volumes demonstrating both insensitivity to size of the end cap volumes

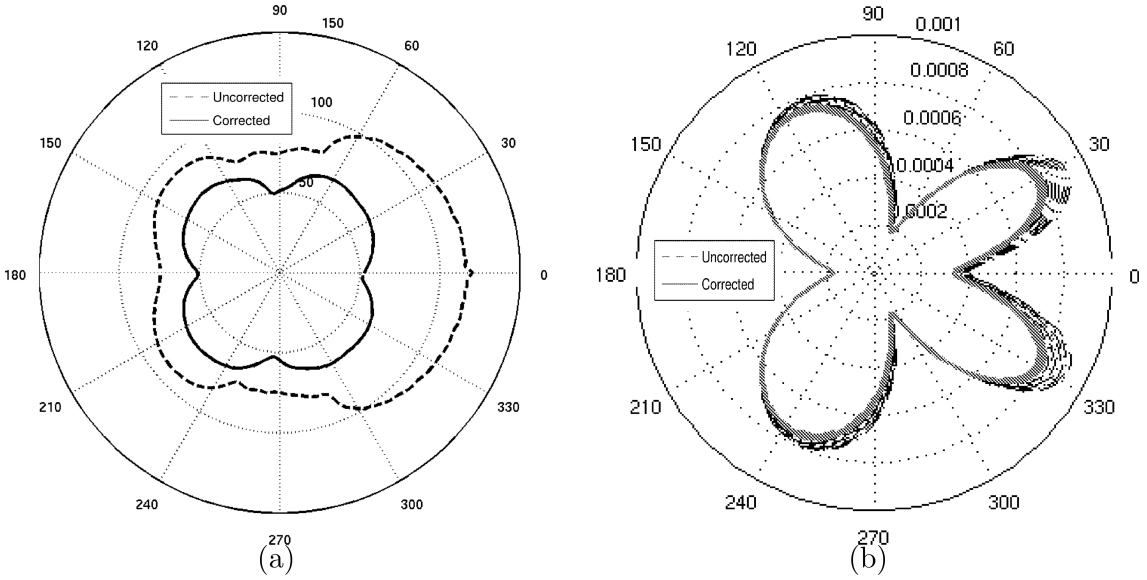

Figure 3.6: Directivity and comparison of volume terms for the Re=150 cylinder. (a) shows the comparison of the recovered quadrupole noise, in SPL(dB), using the prescribed end cap methodology compared to the noise that is computed using no closure mechanism at all. (b) compares the effect of using a fixed or spatially varying convection velocity on recovered noise in p'_{rms} directivity at a discrete frequency, $St = 0.3292$.

in our proposed approach, and the importance of the convection velocity.

The sensitivity to exit plane location was tested by varying the exit plane from 5D to 35D and varying the spacing between correlated planes from dx to 4dx. Note how the results, shown in figure 3.8, are insensitive to both plane location as well as inter-plane spacing.

Figure 3.9 compares the proposed end cap correction method to the other commonly used approaches to compute the overall SPL. Note that the proposed approach is noticeably better. A similar comparison was performed at fixed frequencies. At the Strouhal number of the lift component, $f = f_0$, the proposed method was again seen in figure 3.10 to agree well with the DNS. On the other hand, large variance is seen between the phase averaged approach and others; this is because the distances between subsequent planes are quite small implying large correlation which violates the fundamental assumptions of the phase-average approach. At $f = 2f_0$ which corresponds primarily to the drag fluctuations the proposed method shows good agreement to DNS, i.e. figure 3.11. In

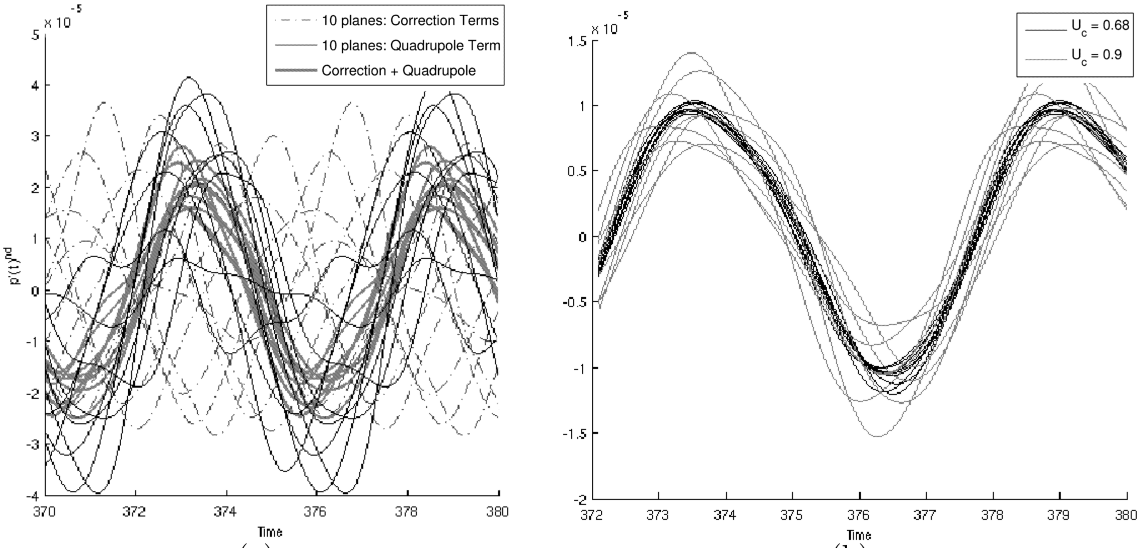

Figure 3.7: The non-dimensional acoustic pressure as a function of time for Re=150 cylinder. (a) displays the calculated volume term, the end cap correction, and the corrected volume noise with an assumed $U_c = 1.0$. (b) shows the same curve as before now with an assumed $U_c = 0.9$ and with the convection velocity obtained by correlation as $U_c = 0.68$. Note how dispersion in the resulting curves is decreased by using the cross-correlation velocity.

contrast, the open and phase averaged methodologies in particular show large variation from DNS data. For the open calculation, there is no predicted sound propagated in the downstream direction while the phase averaging is inaccurate for the same reasons as those described at $f = f_0$.

3.4 Summary

A novel end cap methodology to correct surface terms in the context of porous FWH equations has been proposed and analyzed. This method uses multiple exit planes to extract a convection velocity that can vary as a function of space and time which establishes a model constant for the correction term. This correction term balances the net flux of momentum traversing the porous FWH planes that exists in the dipole term or if using a Curle surface provides the missing component of the volume term exterior to the bounding volume. This approach allows for using the more sensitive FWH equations

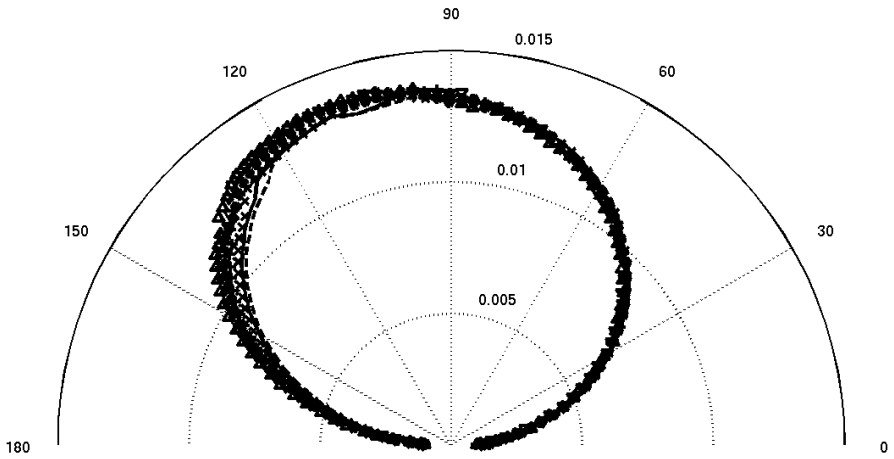

Figure 3.8: Effect of end cap plane spacing and downstream location for the Re=150 cylinder. (–) dx=1dx, L=5D; (-) dx=2dx, L=5D; (x) dx=1dx, L=10D; ($\diamond$) dx=2dx, L=10D; (+) dx=3dx, L=10D; ($*$) dx=4dx, L=10D; ($\triangle$) dx=1dx, L=35D; (∇) dx=2dx, L=35D

in integral form and allows for efficient computation of the acoustic sources due to the ability to maintain minimal volumes while providing proper exit conditions. This approach also lends the ability to query noise contributions from specific volume regions. The proposed methodology works best over short intervals where surface conditions are representative of frozen vortices which are highly correlated. This method is in contrast to the approach of Shur et al.[1] where numerous planes at large separation distances help provide largely phase independent results which are phase averaged to remove spurious noise.

The feasibility of this end cap correction approach was validated for the case of a potential vortex and then was used to predict the noise from various Reynolds' number cylinder flows. The potential flow case demonstrated the terms which are balanced between the dipole noise and the correction term. This case also demonstrated the ability to have a convection velocity that varies as a function of time based on an averaging scheme. For the low Reynolds' number cylinder flow we evaluated the noise computations against Inoue and Hatakeyama [3] and the model of Phillips [41] with close agreement. We also compared our results to other proposed closure methods and found better agreement with respect to the DNS. The approach with spatially varying

convection velocity in the correction term gave the best results. We examined the effect of porous plane placement and displacement and found little sensitivity to these parameters. These results indicate very good accuracy with low computational cost validating the attractiveness of the approach.

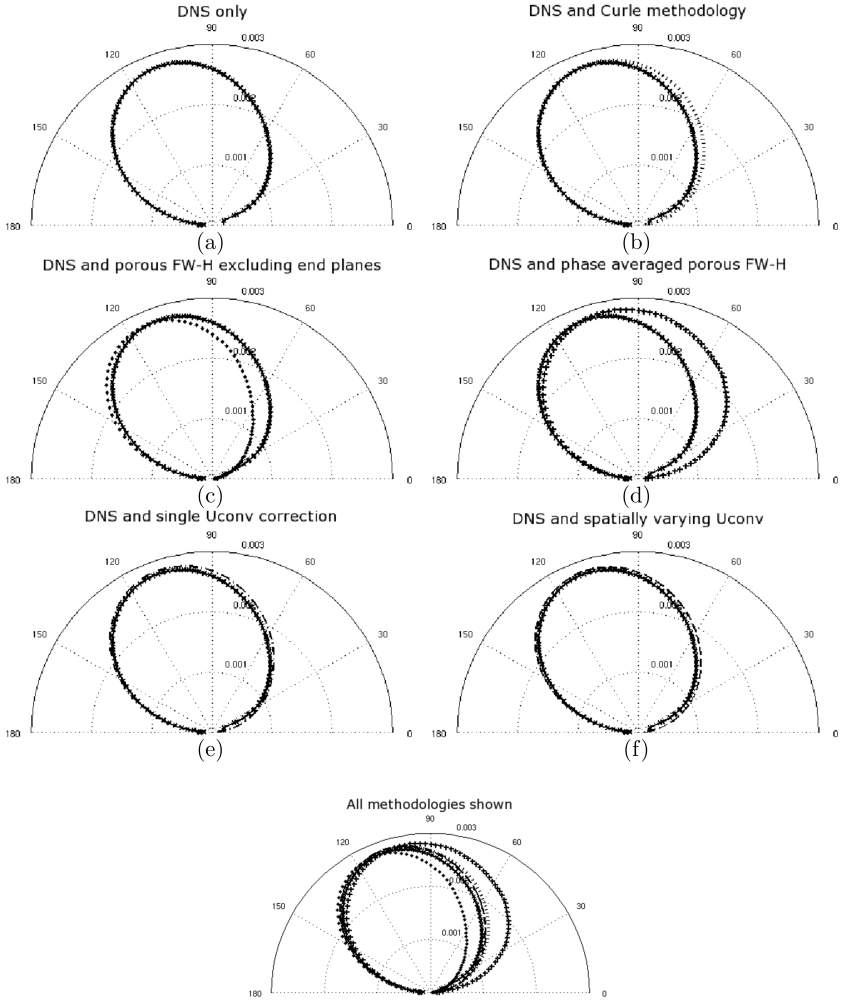

Figure 3.9: Directivity of the received sound, p'_{rms}, for the Re=150 cylinder. (a) is the directivity of received pressure fluctuations directly from the DNS at the microphone locations. (b) is the the comparison of the predicted noise using a Curle methodology compared to the direct DNS approach. (c) a FWH approach with no planes at fixed x-locations downstream of the body, i.e. and open formulation. (d) using a phase average approach over ten downstream planes as suggested by Shur et al. [1].(e) a FWH approach with the described end cap methodology with a single U_{conv} applied at each of the ten exit planes and (f) the same end cap technique with a $U_{conv} = U_{conv}(y)$ approach. (g) Comparison of all of the directivities of the different methodologies as shown

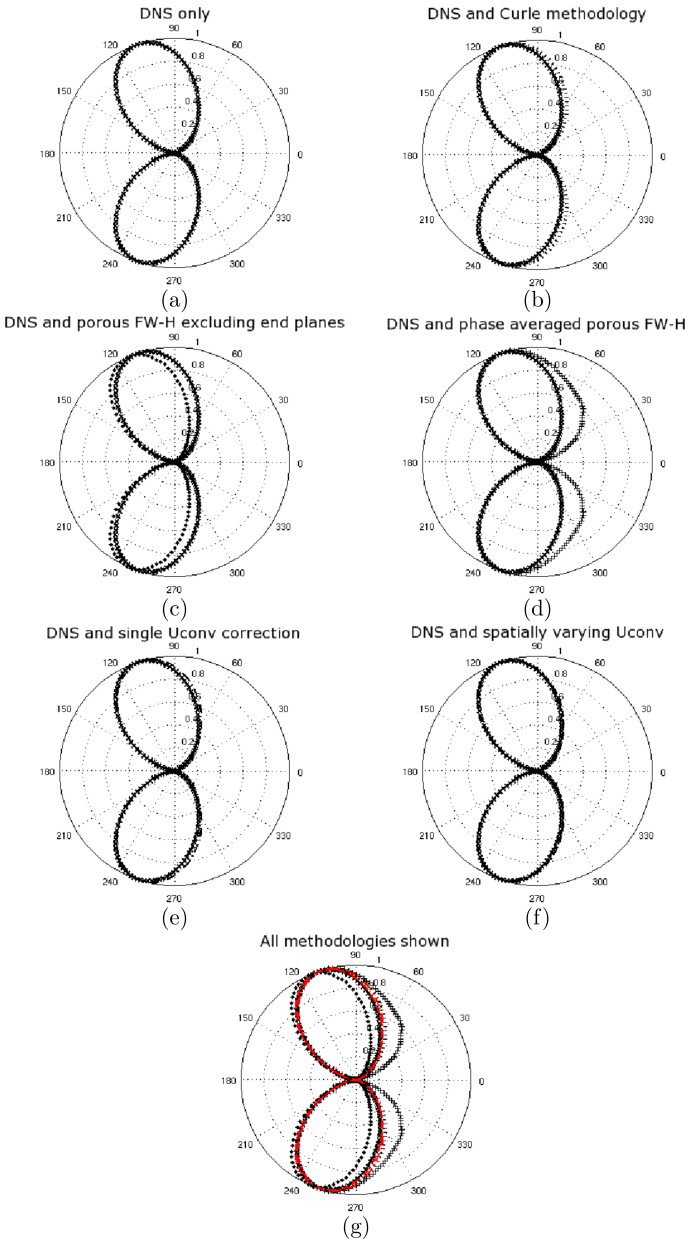

Figure 3.10: Directivity of the sound for the Re=150 cylinder at $f = f_0$ for various approaches. (a) shows DNS only. (b) has a Curle surface approach. (c) is the open exit formulation. (d) is the phase average approach over ten downstream planes. (e) is a FWH approach with a single U_{conv}. (f) is a FWH approach with $U_c = U_c(y)$. (g) is a comparison of all of the different methodologies.

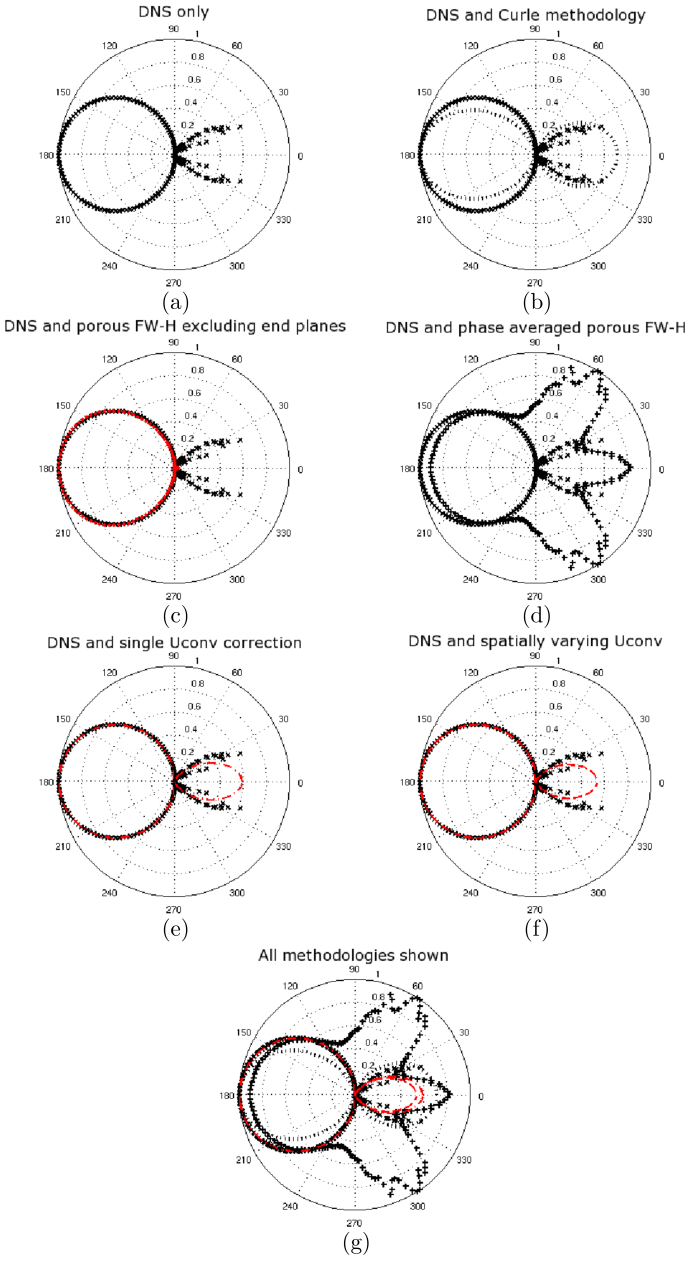

Figure 3.11: Directivity of the sound for the Re=150 cylinder at $f = 2f_0$ for various approaches. (a) shows DNS only. (b) has a Curle surface approach. (c) is the open exit formulation. (d) is the phase average approach over ten downstream planes. (e) is a FWH approach with a single U_{conv}. (f) is a FWH approach with $U_c = U_c(y)$. (g) is a comparison of all of the different methodologies.

Chapter 4

Sound production from cylinders at subcritical Reynolds numbers

4.1 Introduction

The sound field generated from subcritical Reynolds number cylinder flow has been studied since the time of the ancient Greeks. These Aeolian tones, generated by the fluctuating velocity behind cylinders at low Reynolds number, produce surprisingly loud sound [41]. The fluctuating velocity is caused by vorticity generated at the wall diffusing and advecting, which separates the boundary layer and sets up the von Karman street. At lower Reynolds numbers this separation and shedding has a distinct and predictable frequency f, or non-dimensionally a Strouhal number, $St = fD/U_\infty$. As the Reynolds number increases while staying subcritical (below the drag crisis) this regular shedding breaks-up but retains a highly dominant signature. This in turn produces slightly less coherent vorticity in the wake and subsequently the noise has distinct peaks, but also a larger broadband component. For this reason, the noise produced from cylinders have been studied for a while, including serving as a NASA baseline problem [21]. In this chapter, results for wall resolved Large Eddy Simulation (LES) at higher subcritical Reynolds numbers which compare favorably with experiments for both flowfield and sound data, are discussed.

We consider Reynolds numbers of $Re = 3900,\ 10000$ and 89000. Circular cylinder flows at high Reynolds have been examined by Gerrard [50], Roshko [51], and Morkovin

[52]. We also examine results from Macovsky [53], Bishop and Hassan [54], Taniguchi and Miyakoshi [55], Achenbach and Heinecke [56] and West and Apelt [57] in order to validate the flow-field for the $Re = 89000$ case. Norberg [46] gives a comprehensive review associated with the fluctuating lift from cylinders in the subcritical regime; lift contributes most to the noise which cylinders generate. Experiments and computations from the works of Batham [58] and Elmiligui et al. [59] are also used to validate our results for the hydrodynamic field.

In order to investigate the noise production from the cylinders, we utilize results from Schewe [60] and Hansen and Forsythe [61]. Directivity, intensity, sound fields, turbulent kinetic energy, and acoustic source fields are examined. Work from Hardin and Pope [49] and Colonius et al. [62] on noise production from vortices via the process of separation and pairing off is used as background for determining the source strengths of the scattered acoustic field sources. Cantwell and Coles [63] describe the process by which the von Karman street is established for subcritical Reynolds number cylinders, and the relative release of vorticity which is not bound in the traveling vortex cores. It is hypothesized by Cox et al. [6] that it is this energy which establishes the source for both the feedback mechanism which continues the periodic shedding as well as creates the quadrupole source strength which is diffracted by the cylinder e.g. [48].

As Gloerfelt et al. [48] points out, a body at rest cannot itself be the source of sound. This is in contrast to the classic interpretation, that sound production is associated with the pressure forces on the surface as presented by Phillips [41], Goldstein [64], or Blake [65]. The interpretation is that the acoustic energy is due to the pressure fluctuations caused by the vorticity release. The source of this acoustic energy was investigated by Doak [66], Ffowcs-Williams [67], and Crighton and Leppington [68]. They reason that in the near field, $x/D < 1.5$, the vortex stretching which occurs before the recirculation wake closure causes a scattered pressure field to act as the source of noise. Simultaneously, lower pressure due to the asymmetric vortex causes higher pressure in the upstream direction which is radiated by the body into the farfield.

The sound production from cylinders has been investigated numerically via wall resolved LES usually at lower Reynolds numbers, $Re <= 20000$. Only experiments, RANS, DES, and LES with wall models have been used for studying higher Reynolds numbers. For higher number Reynolds number flows RANS or DES have been used by

Cox et al. [6], Elmiligui et al. [59], Slimon et al. [69], Pérot et al. [70], and Catalano et al. [71] for $Re = 900000$ through 1400000. However, often the broadband noise components are suppressed in these computations. To the best of our knowledge, our simulations at $Re = 89000$ are the highest Reynolds number cylinder simulations using wall resolved LES. We will contrast our LES results to RANS for $Re = 89000$.

4.2 Cylinder results

We investigate and contrast the flow-fields and noise production from cylinder flows at $Re = 3900,\ 10000,$ and 89000. We start from a validated in-house data set for $Re = 3900$ provided by [2] and evaluate our acoustic methodology. We validate our acoustic methodology against the computations of Khalighi et al. [4] for $Re = 10000$ and the experiments of Revell et al. [5] for $Re = 89000$.

As the Reynolds number increases, the grid spacing must decrease to accurately resolve the near wall and wake regions in wall resolved LES. A schematic of the grid is shown in figure 4.1 which also shows the bounding box for each computational domain consisting of a semi-circular inflow with radius R_y and a rectangle wake region extending downstream Lx along with the prescribed boundary conditions. The width is L_z in the z-direction and periodic boundary conditions were prescribed in that direction. Table 4.1 lists relevant grid spacing parameters as well as the timesteps used for both the CFD calculation and the acoustic calculation.

The porous FWH surfaces include a series of boxes consisting of a primary box at $x = -5D$ extending from $y = \pm 2.5D$, and a series of ten endcaps spaced at $\Delta x = 0.25$ from $x = 5D$ to $7.25D$. All porous surface data along with the physical surface data were written out to data files to be post processed. The entire data set for the $Re = 89000$ case was 4.7 terabytes. The assumed Mach number for the three cases was $M = 0.15,\ 0.15,$ and 0.2 in order to compare to relevant data. Even though the solutions are derived from the incompressible formulation of the fluid solver a Mach number must be specified to set the sound wave speed in reference to the mean convection speed. All of the frequency data is obtained by performing a 50% overlapping fast Fourier transforms using a Hann filter to ensure periodicity. The time averaged data was also spanwise averaged to increase the sample count.

Table 4.1: Selected grid and timestep parameters used in the calculations for the three cylinder cases.

Re	$R_y x L_x x L_z$	n_z	n_{CV}	Δn_1	y+	Δt	$\Delta t_{acoustic}$
3900	$20 \times 40 \times \pi D$	75	18e6	2e-3	1.4	1e-3	5e-3
1e4	$20 \times 40 \times \pi D$	150	54e6	1e-4	0.52	5e-4	1e-3
8.9e4	$12.5 \times 35 \times \pi D$	150	82e6	1e-4	0.78	2e-4	1e-3

4.2.1 Re=3900 cylinder

At $Re = 3900$, the wake of the cylinder is turbulent; the cylinder flowfield results are obtained from the approach described in [24]. These calculations, using the same data, were continued and served as the basis for our first examinations of the sound produced from turbulent subcritical circular cylinders. The noise data was computed using $100D/U_\infty$ units of time giving a spectral resolution of 0.02 fD/U_∞, due to the 50% overlapping, thus ensuring approximately 10 points below the peak frequency. The Nyquist frequency for this case was 200 Hz.

Flow-field validation

Hydrodynamic flow comparisons were performed by [2] to data from the work of [72], [73], and [74]. Figure 4.2.1 provides a flow visualization of an iso-surface of Q-criterion colored by the u-velocity which a greyscale of pressure shown in the background. Coherent counter-rotating structures are visible in the span, usually at lengths $\pi/4$, in good agreement with what was observed in [75]. A few of the velocity comparisons are shown in figure 4.3 and the minor discrepancy with the data and [2] is due to the current decrease in averaging time which was $100D/U_\infty$ as opposed to $360D/U_\infty$ for [2]. Very good agreement was found for [2] in the mean forces, back pressure, separation angle and recirculation length as well as mean and fluctuation wake velocities. The power spectral densities of the energy agreed quite well with the experiments of [72]. Table 4.2 reports key force parameters including the maximum fluctuation values since surfaces forces drive the majority of noise production.

Table 4.2: Summary of surface forces including fluctuations and frequencies: Strouhal number St, mean drag coefficient $< C_D >$, maximum fluctuating drag and coefficient $(C'_{D,max}, C'_{L,max})$, and rms lift coefficient $\sigma(C_L)$. Additional parameters can be found in [2].

	St	$< C_D >$	$C'_{D,max}$	$C'_{L,max}$	$\sigma(C_L)$
Current	0.2083	1.01	0.0495	0.0532	0.139
Norberg	0.2076	0.99		0.06 ± 0.004	0.137

Sound generation and acoustic results

The noise generated at this Reynolds number has not been studied in the literature, but instead serves as an opportunity for a validated hydrodynamic field to be used to calculate the sound field. Figure 4.4 show the directivity of the overall SPL and p_{rms} as well as the directivity at the Strouhal number and the first three harmonics. The maximum directivity at the St number is 78 deg measured from the front and the maximum overall noise predicted is 55.7 dB at $r/D = 200$. This corresponds to 95.7 dB at $r/D = 100$ which is greater than the 2D results. The SPL falloff between harmonics is 25.4 dB between the St frequency and the first harmonic, similar to the 2D calculations where the drop off was 26.7 dB.

Figure 4.5 shows selected acoustic power versus frequency data at microphone angles of $\theta = 0°, -40°, -81°$ as measured from the downstream of the cylinder. These angles show that the composition of frequency spectrum contains more content at the St frequency f_0 as the angle increases to 90°. This is due to the dipole associated with the lift forces dominating the sound. When the angle is closer to 0° the frequency content has components closer to the drag dipole at $f = 2f_0$ and its harmonics. The angle in-between is a mixture of the two dominant dipole components. Also of note is the large broadband contribution, something lacking in the 2D low Reynolds number cases.

4.2.2 Re=10,000 cylinder

We consider a $Re = 10000$ cylinder as an example of turbulent flow for which we can compare to other simulations which include noise results. Khalighi et al. [4] developed a hybrid boundary element approach which decouples scattered sources from directly

Table 4.3: Summary of surface forces, fluctuations, and frequencies for $Re = 10000$ cylinder.

Metric	Current	Comparison	Author
St	0.197	0.196	Norberg
C'_L	0.503	0.506	Norberg
$< C_D >$	1.336	1.29	Norberg/Khalighi et al.
C'_D	0.090	0.091	Khalighi et al.

propagating sources and compared against an undescribed FWH computation. The noise data was computed using $150D/U_\infty$ units of time and the Nyquist frequency was 500 Hz. A representative flow visualization of an iso-surface of λ_2 colored by u-velocity is shown in figure 4.6. A fixed X-Y plane is used because no large scale coherent spanwise structures exist which are easily visualized. The extracted porous surface elements are shown in figure 4.7.

Flow-field validation

The averaged flow field velocity components are compared to those of Khalighi et al. [4] in figure 4.8(a) and (b); note the good agreement for mean stream-wise velocity and fluctuating components. We surmise from from this result and the surface forces in table 4.3 that good agreement between flow solutions exist. The separation angle $\theta_{sep} = 85.0^\circ$ from the upstream stagnation point with a minimum pressure point at 76°. The recirculation length extracted from the mean flow was $L_{rc} = 1.35D$.

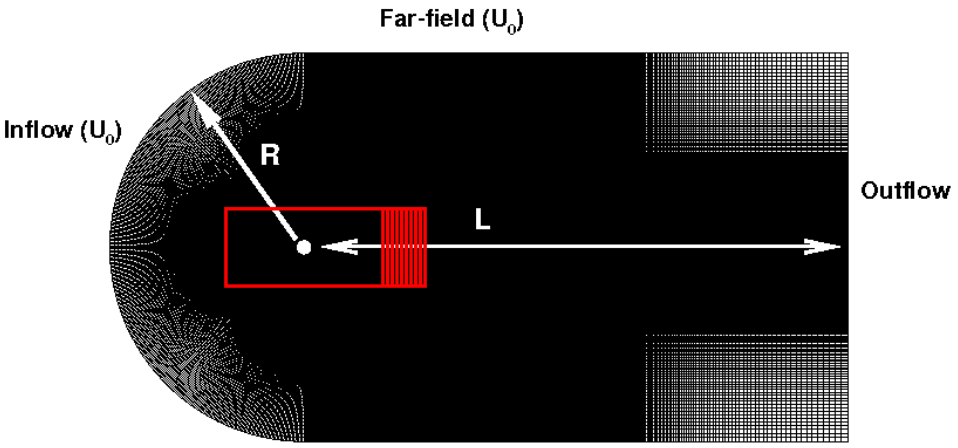

(a)

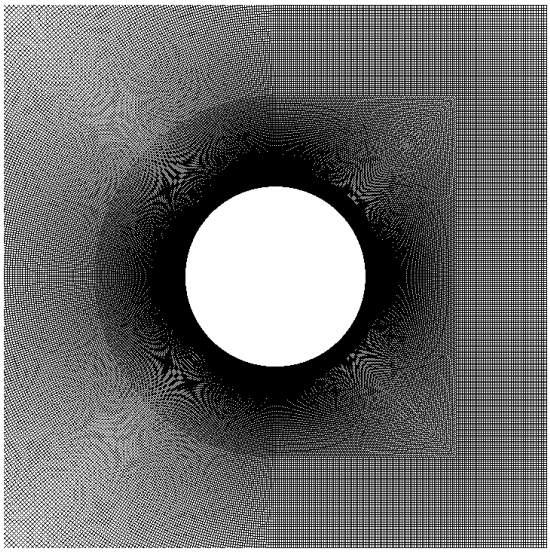

(b)

Figure 4.1: (a) Shows a schematic of the grid including the important lengths detailed in table 4.1 including the positions of the porous FWH surfaces. (b) Shows a closeup around the cylinder detailing the meshing strategy and the fineness of the grid used for the $Re = 89000$ case.

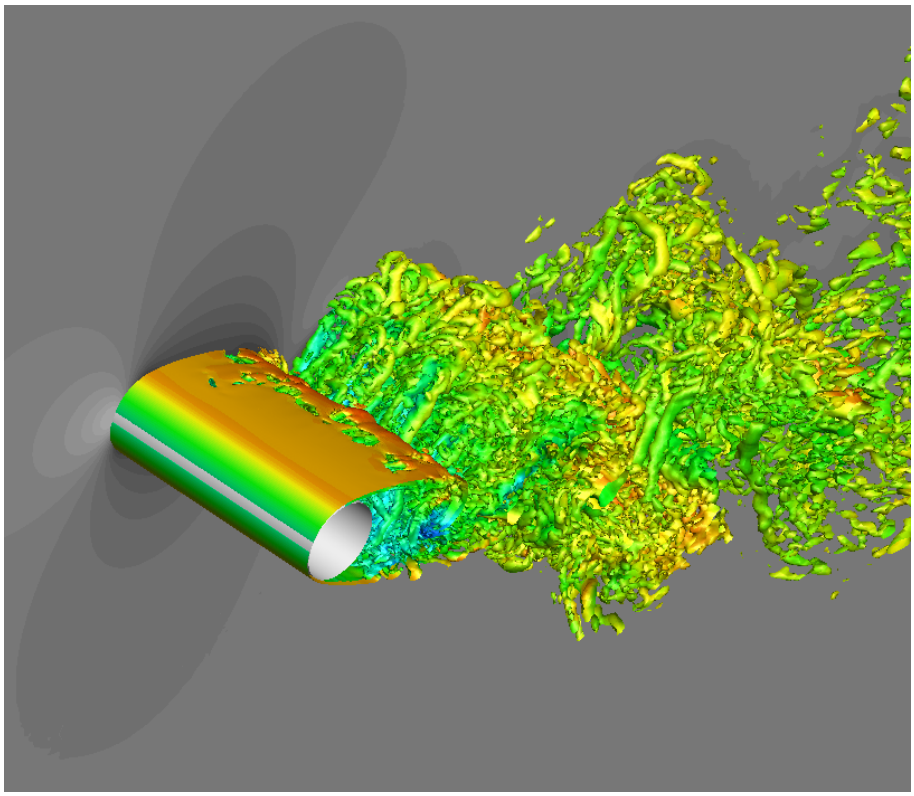

Figure 4.2: Re=3900 flow visualization of iso-contour of q-criterion colored by u-velocity with pressure field in greyscale.

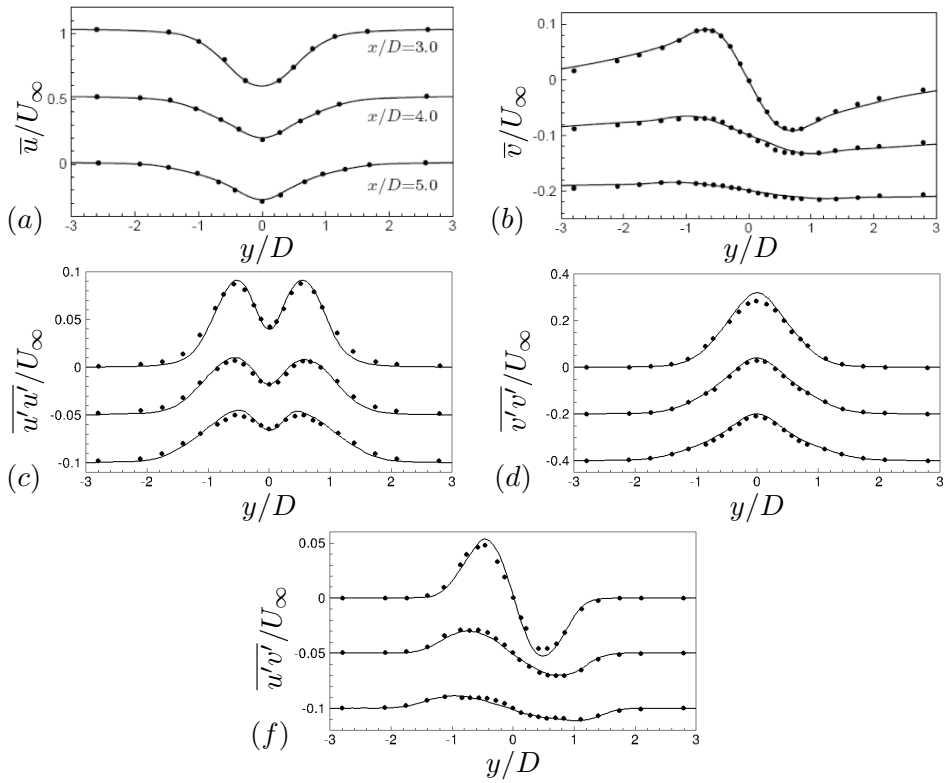

Figure 4.3: Velocity comparisons of the hydrodynamic field for the Re=3900 cylinder versus y/D at $x/D = 3.0, 4.0, 5.0$. (a) Shows mean u-velocity, (b) shows mean u-velocity, (c) shows fluctuating u-velocity, (d) shows fluctuating v-velocity, (e) shows $u - v$ cross stress term.

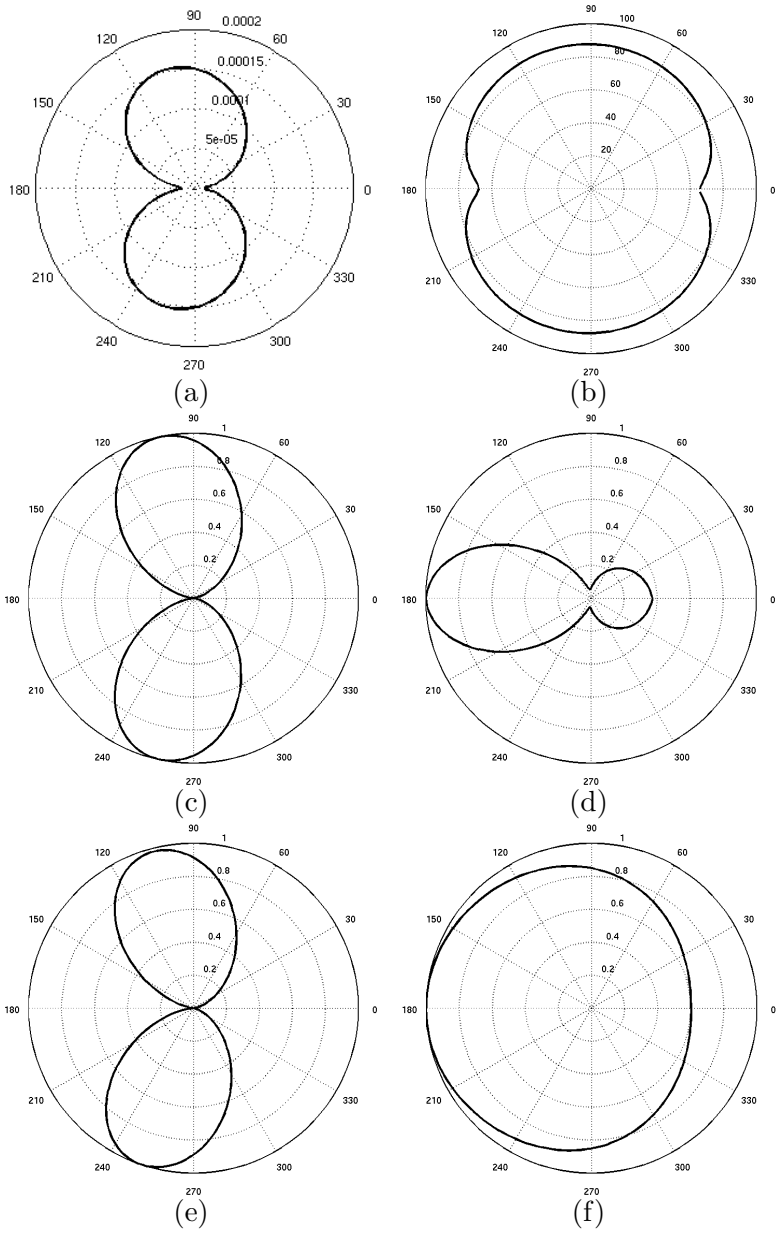

Figure 4.4: Directivity of the sound for the Re=3900 cylinder. (a) shows p_{rms} directivity. (b) shows OASPL directivity. (c) shows the directivity at the St number, i.e. at $f = f_0$ and $\phi^2_{pp} = 5.1258e-5Pa^2$. (d) shows the directivity at $f = 2f_0$, $SPL_{rel} = -25.4dB$, and $\phi^2_{pp} = 1.4800e-7Pa^2$. (e) is the directivity at $f = 3f_0$, $SPL_{rel} = -31.708dB$, and $\phi^2_{pp} = 3.4588e-8Pa^2$. (f) is the directivity at $f = 4f_0$, $SPL_{rel} = -40.62$, and $\phi^2_{pp} = 4.4446e-9Pa^2$.

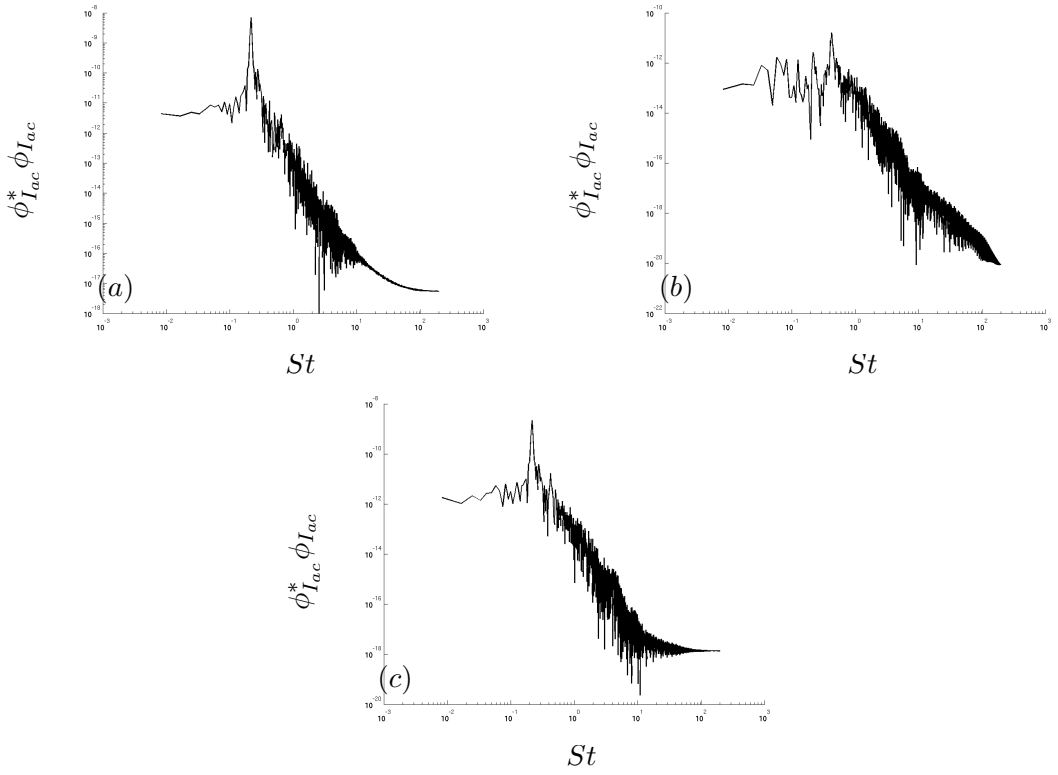

Figure 4.5: Spectral distribution of acoustic intensity power with angles measured from the downstream direction; (a) is at an angle of $-81°$, (b) is at an angle of $0°$, (c) is at an angle of $-40°$.

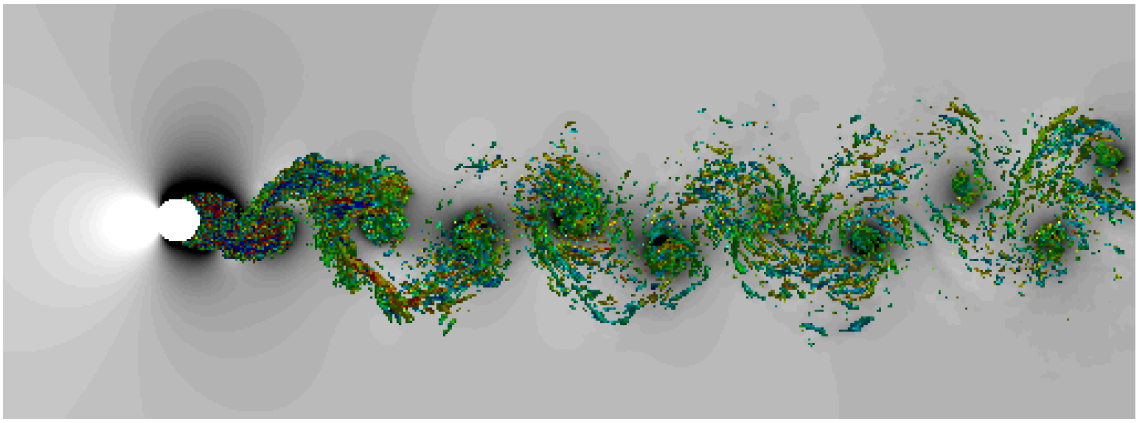

Figure 4.6: A Re=10,000 cylinder flow is visualized using an iso-surface of λ_2 colored by u-velocity with the pressure field in grey-scale.

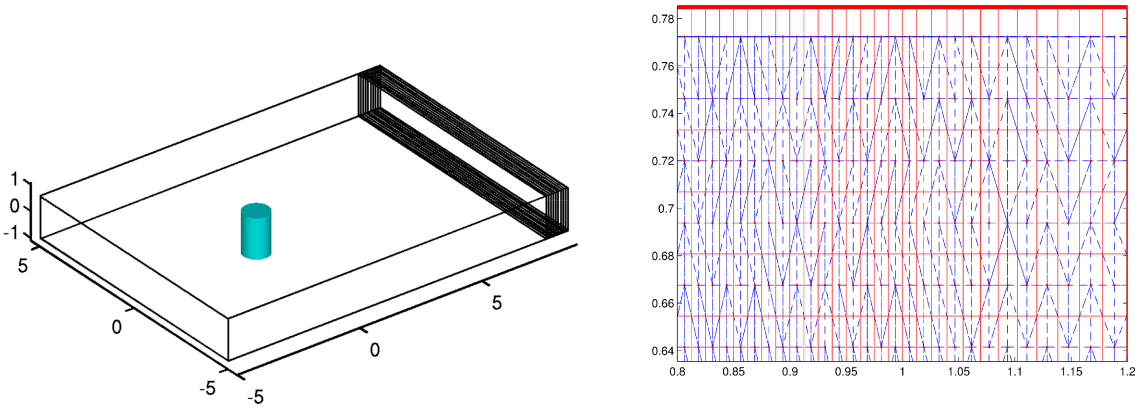

(a) (b)

Figure 4.7: The geometric extraction of the planes for the $Re = 10000$ cylinder are demonstrated in (a) and a closeup of the top plane in (b) shows the Voronoi areas (squares), Delaunay triangulation (triangles), and the boundary (bold-top) of the projected surface elements. Note the contraction of grid spacing with increasing x-distance demonstrating the correspondence between the FWH data surface and the computational grid.

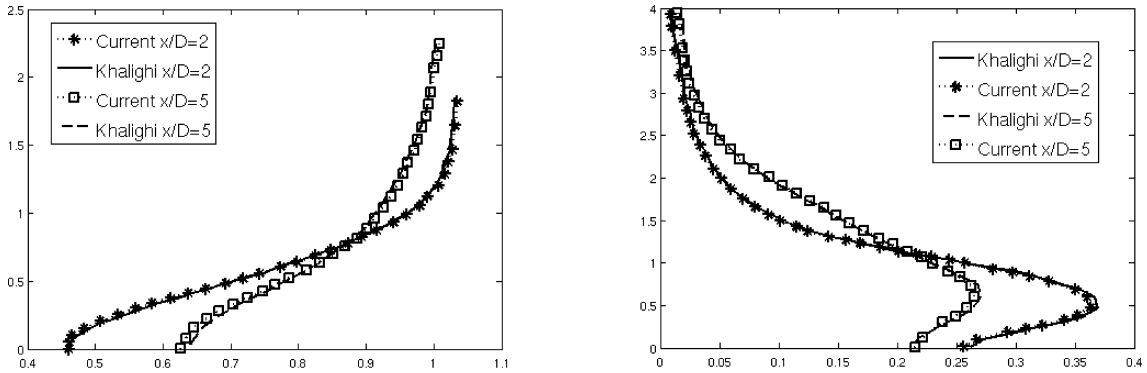

(a) (b)

Figure 4.8: For the Re=10,000 cylinder, the parameters $\bar{u}$ (a) and u'_{rms} (b) from the average flow field at two x-locations $[2, 5]$ are compared to reported results of Khalighi et al. [4].

Acoustic results

The results of figure 4.9 show good agreement in the recovered noise power at a fixed location of (-1.2D,16.2D) indicating consistent flow fields and acoustic content. This location is in the near field being only approximately 3.5 wavelengths away from the cylinder. The acoustic Strouhal number is $St = 0.197$. The maximum recis the largest component overed noise at $r/D = 100$ was 96.1 dB at an angle of 84°. Our methodology is compared at the dominant frequencies displayed in figure 4.10 (a)-(d). Here we find close results with the hybrid methodology which has the effect of volumetric effects through the application of scattered noise in conjunction with direct noise production external to the body. Often the discrepancies that exist are bounded by the FWH results of Khalighi et al. which would demonstrate that surfaces terms are dominant and it is the variation in volume terms that produce the minor difference. The maximum angle of propagation is 83°. The decay in relative SPL between each of the first three harmonics and the dominant frequency is -20.1, -38.2, and -47.0 dB respectively. When only surface terms were used this decay in relative frequency was -26.58, -32.20, and -75.38 dB. Significant differences exist at these even harmonics of the St frequency where the volume term strongly contributes due to Reynolds stresses occurring at these harmonics. This is compared to the reported values in [4] of -20, -37, and -49 dB and close agreement is found.

Overall, total volumetric noise alone contributes 12.83% of the overall p_{rms} which corresponds to 1.05 dB. The spatial distribution of the Lighthill stress tensor which is responsible for the volume noise is shown in figure 4.11. This shows that the bulk of the volume noise is generated well within the porous surfaces which are placed at $5D$ through $7.25D$ downstream. The most important result is that the volume sources are most active in the near wake region where the vorticity is being highly strained before the periodic von Karman street is established.

4.2.3 Re=89,000 cylinder

The highest Reynolds number cylinder flow that we investigate, $Re = 89000$, is chosen to compare against the experiments of Revell et al. [5] who placed a cylinder into the exhaust of a nozzle and captured the noise with a microphone array. More recently, Cox

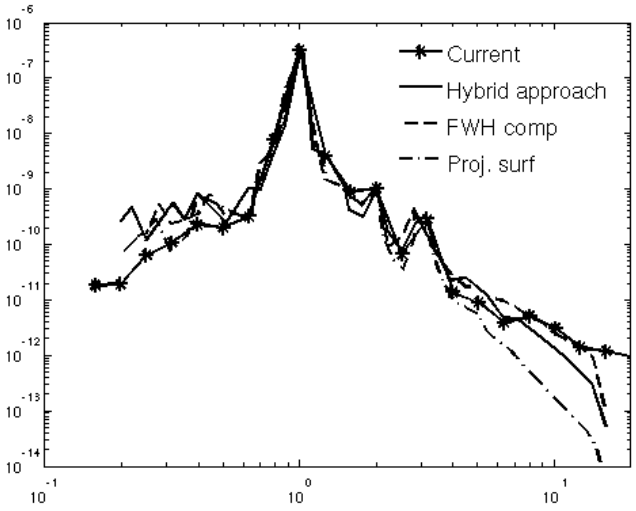

Figure 4.9: A comparison of the predicted noise power versus frequency at the location (-1.2D,16.2D) for the Re=10,000 cylinder is plotted against Khalighi et al. [4].

Table 4.4: Summary of surface forces, fluctuations, and frequencies for $Re = 89000$ cylinder.

Metric	Current	Comparison	Author
St	0.189	0.184	Revell et al. [5]
C'_L	0.512	0.509	Norberg [46]
$< C_D >$	1.1656	1.17	Batham [58]
C'_D	0.122	0.103	Szepessy and Bearman [76]

et al. [6] computed this configuration using the unsteady Reynolds–averaged Navier–Stokes (URANS) approach with two different closure models, and obtained results which indicated only dominant frequencies and their harmonics. The noise data was computed using $180D/U_\infty$ units of time and the Nyquist frequency was 500 Hz. A flow visualization is shown in figure 4.12 from which we can see that the flow structure resembles the flow at lower Reynolds numbers but has a larger range of scales and a larger spreading angle.

Flow-field validation

The minimum pressure point is at 70° and separation angle 82.2° from the upstream stagnation point. The recirculation length was $L_{rc} = 1.29D$. The mean u-velocity behind the centerline of the cylinder is compared to experiments of [75] and [63] in figure 4.13 and good agreement is found. The lack of hydrodynamic data at this Reynolds number means that other cylinder experiments and computations in the subcritical regime are used as the basis for comparison. The coefficient of pressure is also contrasted to [6], [76], and [77] in figure 4.14. The closest agreement is found to be with the URANS calculation of Cox et al. [6] at a very similar Reynolds number. These results and the good agreement found in mean and fluctuating force data provided in table 4.4 provide confindence in the hydrodynamic flow-field.

Acoustic results

The noise at $\theta = \pi/2$ and $r = 128D$ as shown in figures 4.15 and 4.17 shows good agreement at the fundamental frequency as well as the drag and first lift harmonic. The first lift harmonic for the current results show some shift relative to the experiment but our results show the frequency at $f \approx 3f_0$ where the first overtone of lift should reside. In contrast, the URANS predicts no harmonics of lift and drag since it is a 2D computation and has a larger shift in the Strouhal frequency relative to current results. There is a discrepancy at lower frequencies but it is not due to insufficient time samples as we have 180 units of time giving spectral discrimination of 0.0055. The directivities of the overall sound production is broader than that of the $Re = 10000$ case, but the component harmonic directivities show similar results to those at lower Reynolds numbers. The reason for this subtle difference is that the higher frequencies, not shown on the spectral plot, contain more of the overall content, though still quite a small relative to the dominant harmonics. Overall the agreement with experiment is quite good and significantly better than the URANS.

The volumetric noise production is 18.63% of the acoustic pressure which accounts for 1.481 dB of the overall noise. A view showing the instantaneous surface and volume terms is shown in figure 4.20. Here the highly three-dimensional volume sound source field can be seen even with its strongly coherent surface pressure sources acting on the

cylinder. A time averaged view of the mean Lighthill stress field is shown in figure 4.18. The sound field is visualized by solving the FWH equations at a fixed time throughout the domain and the wake is visualized by λ_2 in figure 4.16. It is clear that the principal source of sound is associated with the cylinder body and that the wake provides higher frequency content.

4.3 Interpretation of sound generation phenomena

The sound field radiates preferentially in the upstream direction due to convective amplification where the mean background velocity amplifies the waves by compacting them. This radiation is due to the fluctuating pressure near the stagnation point which is amplified. This is directly tied to the fluctuation in the lift as it cycles at the shedding frequency. This and the drag dipole are the principal source of the sound which is the explanation advanced by [11] and [64]. This can also be seen in in figure 4.19 where the low pressure in the wake from the shedding of the laminar boundary layer has cause a pressure deflection. This interpretation is directly linked to the other posited interpretation. This noise source field is highly active in regions where the strain of the vorticity in the wake is highest and vorticity itself is absent as seen in 4.20. This interpretation is related to the work of [78], [79], and [69], where they report noise generation which is directly related to the strain of the vorticity. Furthermore according to [63] approximately half of the vortical energy produced at the wall is trapped in the vorticity in the von Karman street leaving meaning the other half is converted to other forms of energy within the $< 5D$ distance it takes to establish the von Karman street. This rationale is supported by the Lamb form of the FWH equations i.e. A.14 as shown in appendix A.

Sound production as a scattered quadrupole

This linking of mechanisms is directly related to the work of [48] and [70] where the scattering of the volume terms is presented as the mechanism which links the volumetric nature of the source field to the pressure radiation associated with the shifting force dipoles. In this interpretation a point quadrupole located behind the cylinder acts as the only direct sound source and is amplified by causing a feedback mechanism in which the high pressure near the stagnation point oscillates. The scattered sound equations

for a cylinder which decouples the incident, $\hat{p_0}$, from the scattered noise, $\hat{p_s}$, are found in [48] as,

$$\hat{p_0} = \frac{A}{4i}\sum_{m=0}^{\infty}\varepsilon_m \cos(m(\theta_y-\theta_x))H_m^{(1)}(kr_x)J_m(kr_y) \tag{4.1}$$

$$\begin{aligned}\hat{p_s} &= -\frac{A}{4i}\sum_{m=0}^{\infty}\varepsilon_m \cos(m(\theta_y-\theta_x)) \\ &\times \frac{J_{m-1}(kr_y)-J_{m+1}(kr_y)}{H_{m-1}^{(1)}(ka)-H_{m+1}^{(1)}(ka)}H_m^{(1)}(kr_x)J_m(kr_y),\end{aligned} \tag{4.2}$$

where A represents the source strength, the subscripts x, y denote microphone and source locations respectively, a is the cylinder radius and H, J are the Hankel functions of the first kind and Bezel functions. By using this model, a MATLAB code was written which tested a scattered quadrupole with a volume source term of 18.6% at $1.3D$ downstream of the cylinder. Only 76 percent of the total noise was predicted. The location, strength, and number of wave numbers m was perturbed to ensure convergence. A quadrupole source strength approximately 1.6 times higher than is actually present would be necessary to predict the same total noise. This suggest that the surface amplifies the incident quadrupole noise while it is scattered.

4.3.1 Effect of Reynolds number on sound generation for sub-critical cylinders

For subcritical Reynolds numbers cylinders as the Reynolds number increases the noise increases, the minimum pressure point and the separation point move upstream, and volumetric noise contribution increases. Also, the recirculation length shortens as the length before the von Karman street is established increases. This leads to a larger interaction region where vorticity is strained and interacts with subsequent separation events and noised is produced. This can be seen by the increase in magnitude in source terms along the initial shear layer at the highest Re case. This interaction region also describes why the maximum noise angle increase toward 90°; as more volume noise is produced further downstream the direct contribution causes an overall steeper angle due to the separation distance and the convective amplification angle.

4.4 Summary

Our FWH method was extended to highly three-dimensional flows for cylinders at $Re = 3900, 10,000$ and $89,000$. For these cases, flow comparisons with previous work show good agreement in the resolved sound fields. The method therefore shows good performance for highly turbulent external flows. Furthermore, the predictive ability with high resolution LES demonstrated significantly better results than U-RANS when compared against experiment for the highest Reynolds number case. The larger range of scales and the inherent three-dimensionality do not require the assumed correlation length approach of the two dimensional U-RANS and is reflected in the noise results with more frequency content represented. Overall, the proposed approach has attractive features such as small but customizable volume computation and higher accuracy than other standard methods.

A physical description of the noise production is given based on combining previous arguments to present a unified argument. As vorticity is shed into the wake it is sheared due to the background flow. Due to the large misalignment between the velocity and the vorticity the acoustic source terms in the Lamb vector produces noise. This region of high acoustic source production is where the Reynolds stresses are the highest. This stress field corresponds to a quadrupole distribution which exists behind the cylinder which is in effect scattered by the body. The exact same mechanism of unsteady vorticity release dictates the pressure oscillation of near the upstream stagnation point. This high pressure is radiated from the body, amplifying the scattered scattered and incident volume noise.

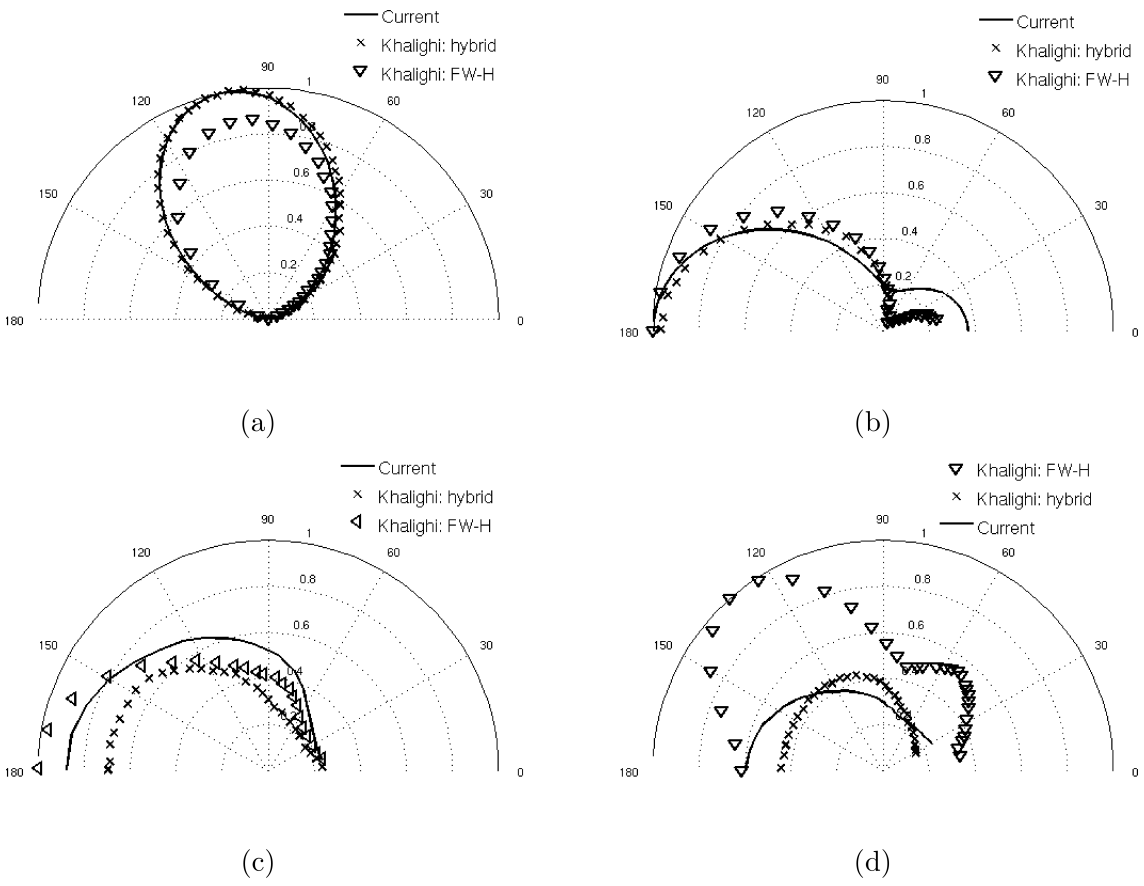

Figure 4.10: A comparison of the directivities for the Re=10,000 cylinder at select frequencies at $r/D = 100$ (a) $f = f_0$, and $\phi_{pp}^2 = 1.0957Pa^2$ (b) $f = 2f_0$, $SPL_{rel} = -20.1dB$, and $\phi_{pp}^2 = 1.071e-2Pa^2$, (c) $f = 4f_0$, $SPL_{rel} = -38.2dB$, and $\phi_{pp}^2 = 1.664e-4Pa^2$, and (d) $f = 8f_0$,$SPL_{rel} = -47.0dB$, and $\phi_{pp}^2 = 2.186e-5Pa^2$ for the described end cap methodology versus two methods presented by Khalighi et al. [4].

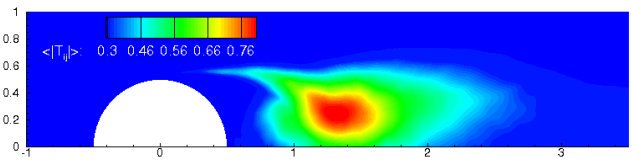

Figure 4.11: Mean of the absolute value of the volumetric based Lighthill stress tensor sources.

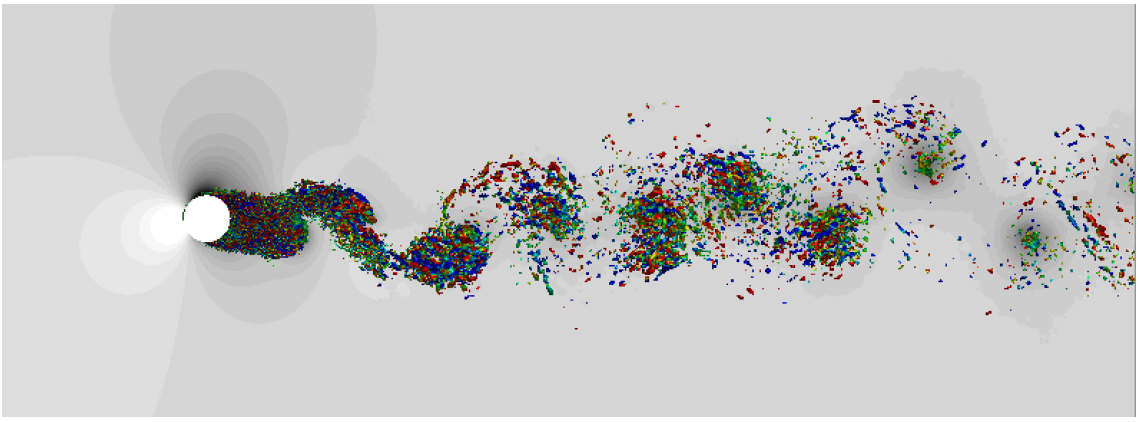

Figure 4.12: The Re=89,000 cylinder flow is visualized by λ_2 colored by u-velocity with pressure field shown in grey scale.

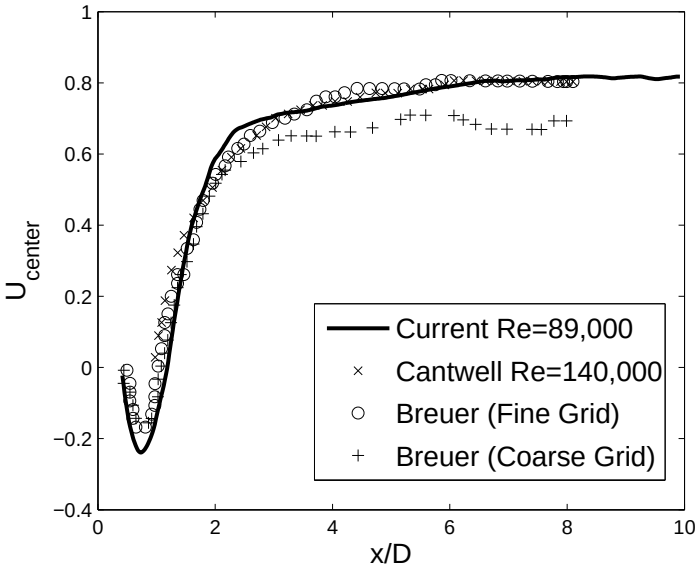

Figure 4.13: The Re=89,000 cylinder centerline velocity is compared to subcritical cylinder flows with comparable Reynolds number.

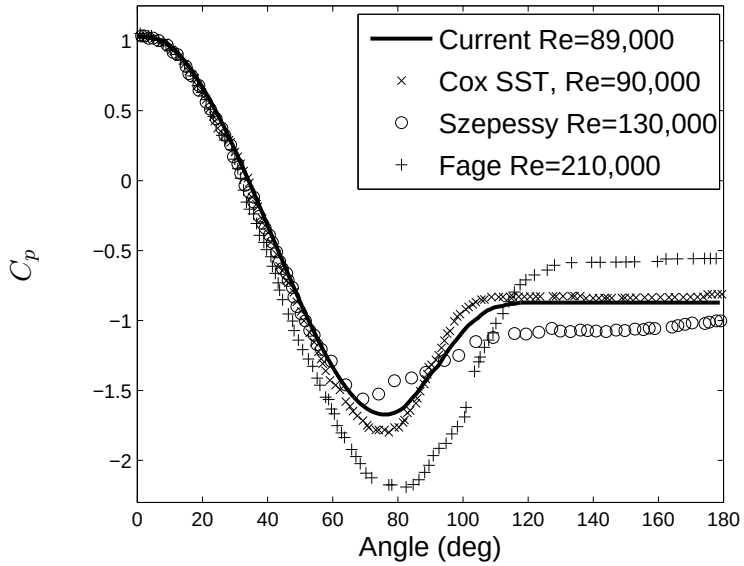

Figure 4.14: Re=89,000 cylinder coefficient of pressure comparison.

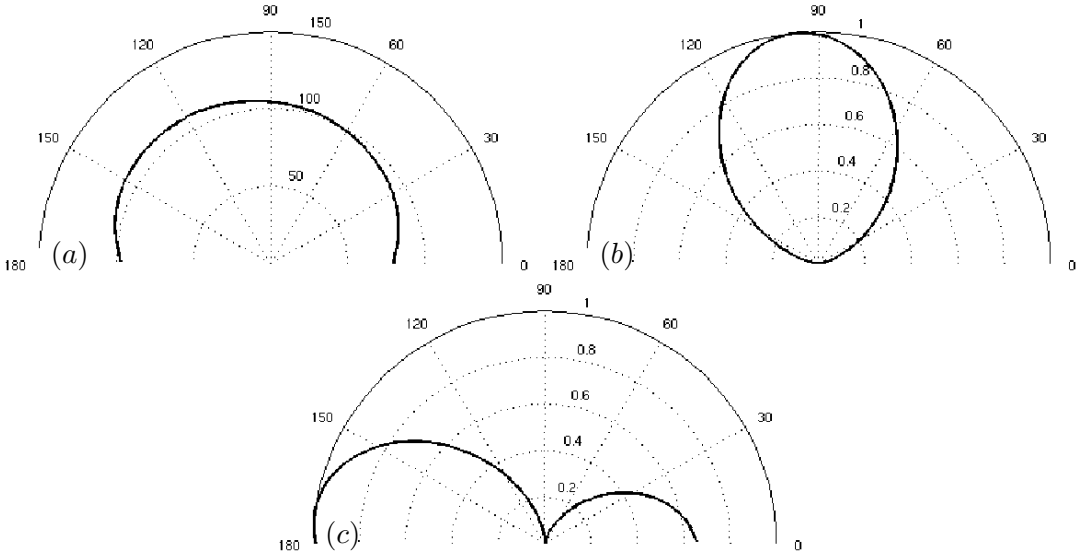

Figure 4.15: The acoustic p'_{rms} directivities for the Re=89,000 cylinder are shown for the overall and major component frequencies as (a) overall, (b) $f = f_0$, and (c) $f = 2f_0$ respectively.

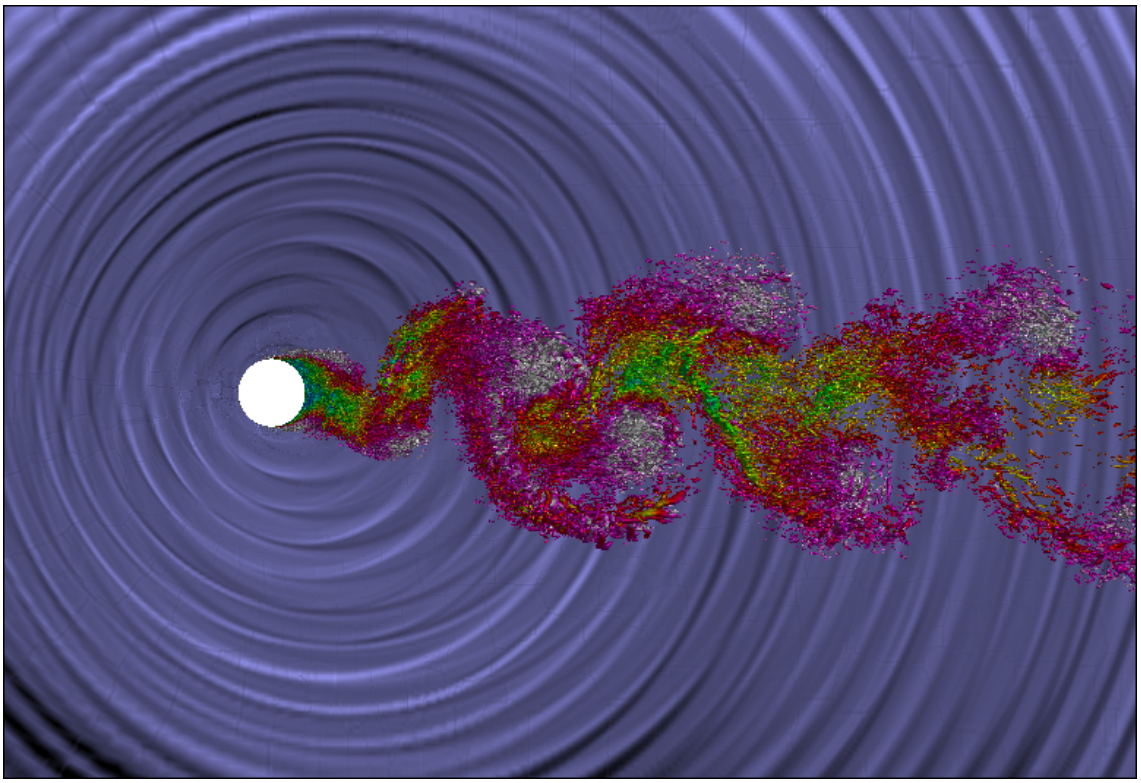

Figure 4.16: The Re=89,000 cylinder wake flow is visualized by λ_2 colored by u-velocity and the sound field is visualized by solving the FWH equations.

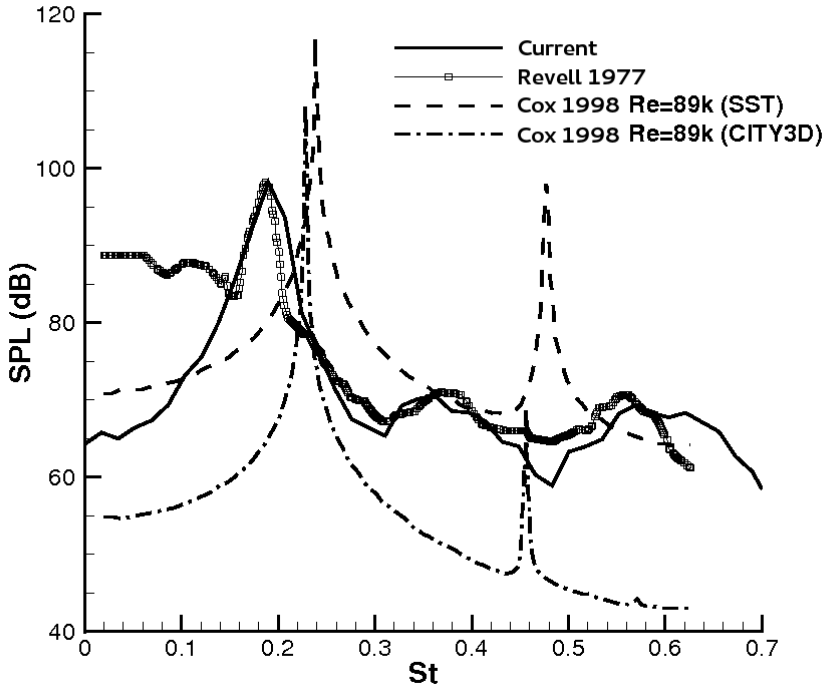

Figure 4.17: The frequency content of the generated noise, SPL(dB) vs frequency, at the location $\theta = \pi/2$ and L=128D is compared to the experiments of Revell et al. [5] and the computations of Cox and Brentner [6].

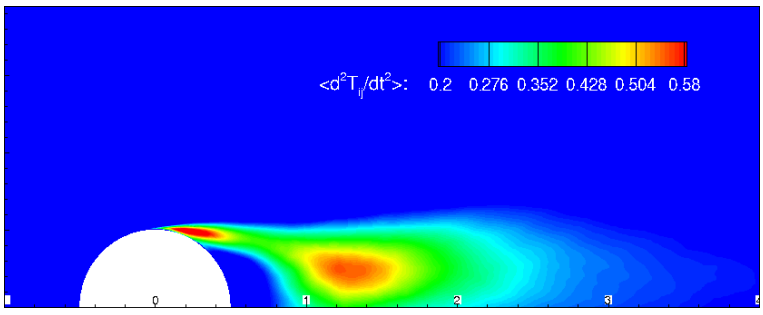

Figure 4.18: The mean of the absolute value of the Lighthill stress field.

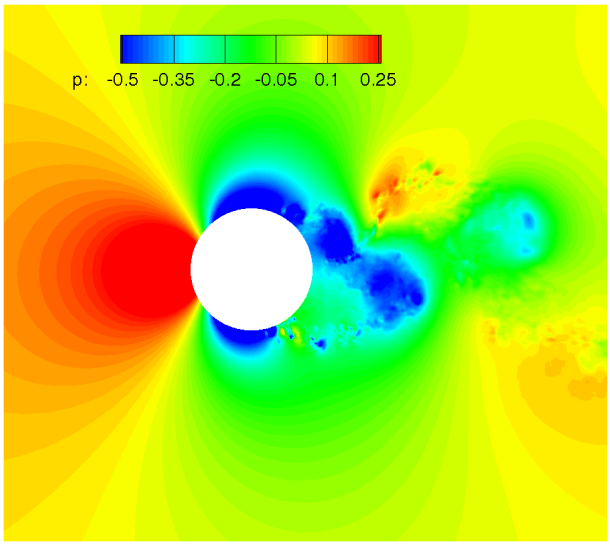

Figure 4.19: A contour plot of the pressure field showing that as the vorticity is released from the upper surface the pressure field around the stagnation point is deflected downward.

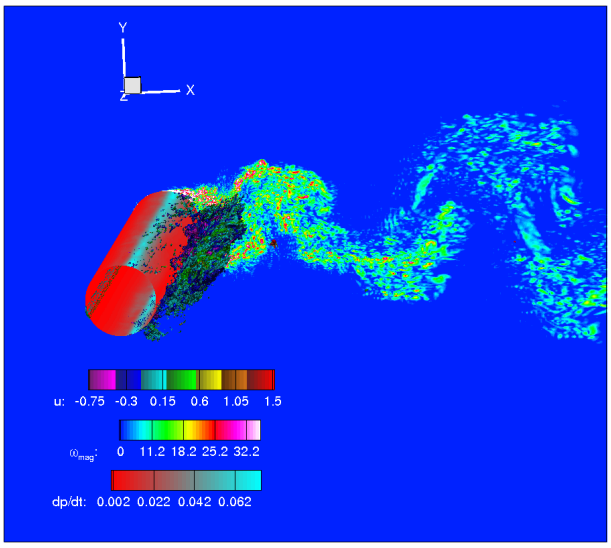

Figure 4.20: The instantaneous volumetric sound source and fluctuating surface force.

Chapter 5

Trailing Edge noise

5.1 Introduction

Investigating noise production from trailing edges and airfoil shapes extends back to the work of Gutin [80]. The trailing edges of airfoil shapes are largely responsible for the noise from a variety of configurations including propellers, fans, rotors and aircraft wings. The theoretical framework for investigating these trailing edge configurations was greatly advanced by Williams and Hall [81] with the application of a tractable half-plane Green's function to theories of [10]. This theoretical work was advanced and extended by Howe [82] who looked at scattering noise for a broad range of frequencies.

A pair of related challenge problems, for trailing edge configurations have been studied. The first one was a trailing edge of 25° which was largely studied by Blake [83]. This produced non coherent shedding and lacked acoustic comparison data, so a second beveled trailing edge at 45° was studied by Blake [84], Gershfeld et al. [85], and summarized in [86]. Additional experiments were conducted more recently to examine the sound field by Olson and Mueller [7], Shannon and Morris [87], and Shannon et al. [88].

A number of computational studies were performed to investigate the noise from trailing edges. These include Wang and Moin [20] who studied 25° trailing edge corresponding to the work of [83] and found comparable trends to the work of [85]. Manoha et al. [89] investigated noise from a flat plane and demonstrated the need for a specific Green's function if surface terms are used for a Curle type acoustic analogy. Oberai

et al. [90] studied scattered noise from airfoils by comparing the scattered noise from prescribed quadrupoles near the trailing edge to an LES performed for the airfoil geometry. A much thinner trailing edge that was excited by a vortex generator slightly upstream was computed using a porous FWH method by Singer et al. [91]. All of these results demonstrated the impact of the noise which is generated by the flow and is then amplified and radiated by the body.

5.2 Problem description

We simulate the experiment by [7] where a 45° beveled airfoil of height h and length $18h$ is placed halfway into the exit nozzle of a low speed $M = 0.1$ flow at a Reynolds number $Re_c = 1.9e6$ such that $9h$ is outside of the nozzle. As a result, half ($9h$) of the airfoil is simulated as well as a larger wake region. The Reynolds number based on height is $Re_h = 105,555$. In the experiment a microphone array is positioned at a distance of $20h$ away and is arranged to capture the corrected noise perpendicular to the trailing edge point. An example flow visualization is shown in figure 5.1 which shows the turbulent wake.

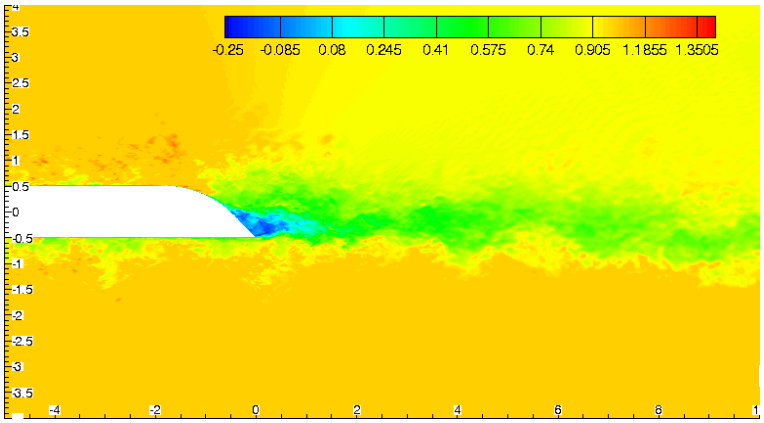

Figure 5.1: An instantaneous u-velocity flow visualization of the trailing edge problem.

This experiment has also been simulated by Wang [8] and it was found that prescribing far-field conditions from the experiment did not produce acceptable agreement in the wake velocities and wake deflection. A RANS simulation was performed by them

on a much larger domain with free stream boundary conditions and the pressure distribution was found to be in closer agreement. Boundary conditions for the fully resolved grid were then extracted on the smaller domain extent in order to maintain the pressure distribution. A similar procedure shown in 5.2.1 was required for the current work as pressure and wake profiles were at first in poor agreement until after an oversized calculation was performed. Extracted mean velocity from the oversized calculation was applied as the far-field condition on the smaller domain and a periodic boundary condition was used in the span. A recycle-rescale methodology detailed in appendix C was employed on both the upper and lower surfaces of the trailing edge with a prescribed $Re_\theta = 1895$ and 1760 respectively, consistent with [8]. The recycle plane was set to be $x/h = 1.75$ or approximately $10\delta_{upper}$ downstream of the inflow condition. The vertical extent of the recycle domain is 1.5δ, which is smaller than the vertical extent of the computational domain. Therefore, at the inflow plane, the recycle values are prescribed at y-locations smaller than the vertical extent of the recycle domain. At larger y locations, the streamwise velocity is set to its freestream value and the vertical velocity is obtained from a quadratic curve constrained by the vertical velocities at the top of the recycle domain and the computational domain respectively.

The simulation solved the incompressible LES equations with a wall spacing of $\Delta n = 2.5e-5$ near the trailing edge and $\Delta n = 5e-4$ in the boundary layer. A timestep of $\Delta t = 5e-5$ was used. The domain was $x/h = [-9, 35]$, $y/h = \pm 20$, and $z/h = 20$ with approximately 72 million total grid points used, and 150 points along the span. The trailing edge tip was rounded with a radius of $0.0005h$ and an extra dense region within a normal distance of $2h$ from the wall was used to resolve the separation and wake interaction. A grid schematic is shown in figure 5.2 which also shows the FWH planes.

The noise was calculated at a distance of $100h$ with a $\Delta T = 100$ and $\Delta t = 5e-5$ giving a spectral discrimination of $0.01Hz$ and a Nyquist frequency of $10,000Hz$. In the experiment a $10Hz$ pass band filter with a Nyquist frequency of $4000Hz$ was used at the location $(x/h, y/h) = (3, 21)$ as opposed to our approach with a Hann filter using 50% overlapping. Wake data as well as available noise data is compared to [8] and [7]. Additional noise calculations such as directivity and sound sources both on the trailing edge as well as within the wake are also presented. A second calculation is performed

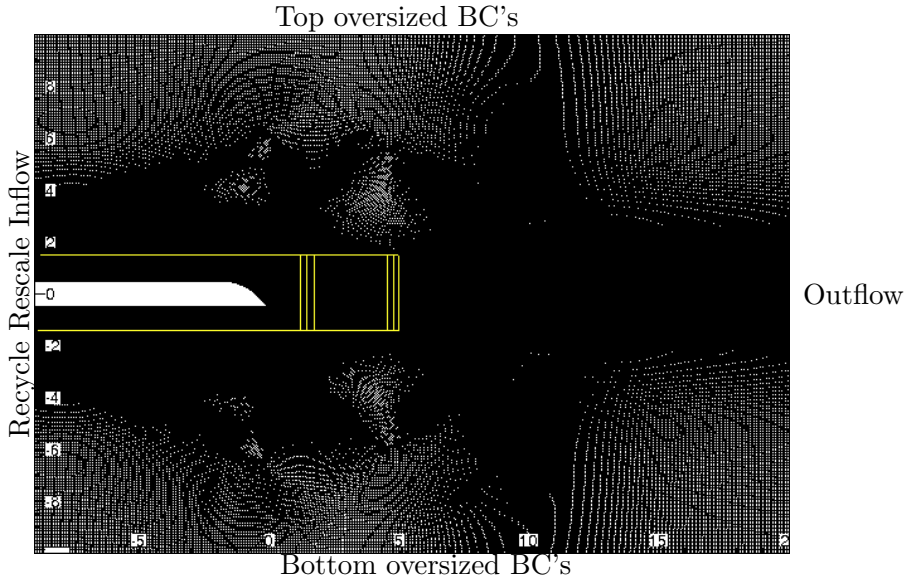

Figure 5.2: A schematic of the grid, FWH planes, and boundary conditions for the trailing edge problem.

with an 18 times thinner boundary layer and the effect of boundary layer thickness is examined. Finally the choice of Green's function and the utilization of the 3D free-space Green's function is examined in the context of using surface terms and the semi-infinite half-plane approximate Green's function.

5.2.1 Oversized grid extent calculations

An oversized domain of $(x/h, y/h) = \pm 100h$ was used and the upstream section including a semi-cylinder fore-body was simulated. Since the entire airfoil was simulated and the domain was significantly larger than the body a far-field condition of $u = u_\infty$ was applied on the inflow as well as the top and bottom. An outflow Neumann condition was applied at the exit and periodicity enforced in the span. An example flowfield in the vicinity of the trailing edge is visualized in figure 5.3. The effect on the coefficient of pressure can be seen in figure 5.4 which shows both the coefficient of pressure along the body before and after the use of the modified far-field boundary conditions.

The time average of $\partial^2 T_{ij}/\partial t^2$ which acts as the dominant source of sound which is in turn amplified and scattered by body is shown in figure 5.5. The maximum location is near the trailing edge point with some source contributions from the upper shear layer.

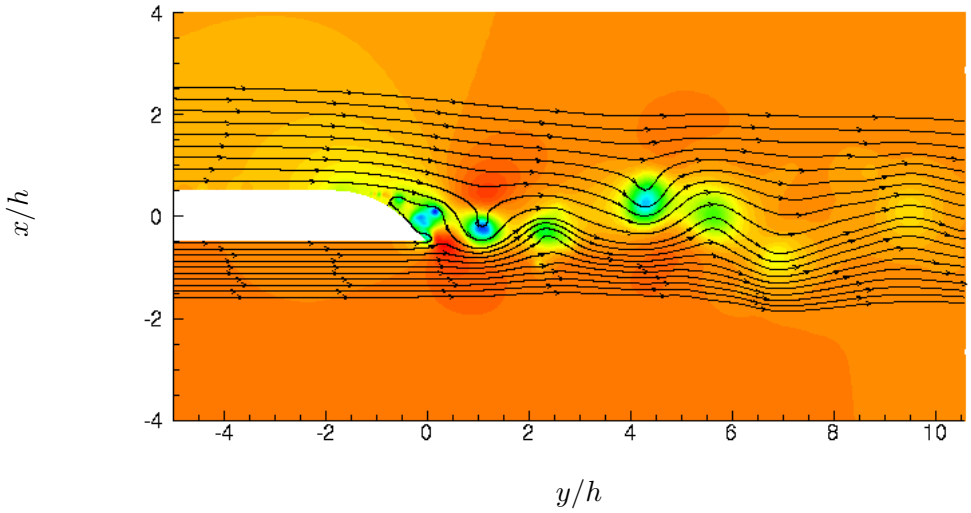

Figure 5.3: Instantaneous pressure contours with streamlines from the oversized calculation.

It is clear that there is no significant deflection wake due to the boundary layers being inconsistent with the experiment. This shows that the oversized calculation constrains the outer boundary conditions and matches coefficient of pressure match better but it is the recycle rescale inflow boundary condition which provides good boundary layer characteristics.

Upper and lower boundary conditions

The time averaged velocity profiles averaged over 260 units of time were extracted at $y/h = \pm 20$. The profiles, as shown in 5.6, were represented by either a fifth or ninth order polynomial as demonstrated in table 5.1. The polynomials were modeled using the MATLAB function polyfit by the equation

$$f(x) = f_1 xs^n + f_2 xs^{n-1} + \cdots + f_n xs + f_{n+1} \tag{5.1}$$

$$xs = \frac{x - \bar{x}}{\sigma_x} \tag{5.2}$$

where xs is the mean scaled x distance. For all equations $\bar{x} = 6.627$ and $\sigma_x = 9.102$. The maximum L_2 error was less than 0.26% when evaluated at 100 points. It should be noted that outside of the x-domain on the fine grid, the polynomials diverge quickly.

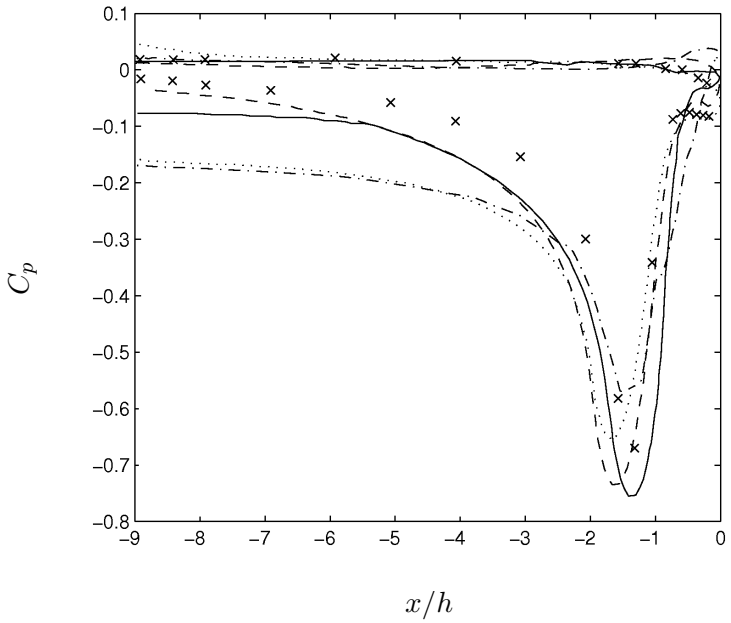

Figure 5.4: Coefficient of pressure from all the methods: (–) current with adjusted BCs, (-.) current with freestream BCs, (x) Olson and Mueller [7], (− −) Wang [8] with adjusted BCs, (. . .) Wang [8] freestream BC.

5.3 Experimental boundary layer

The experimental boundary layer thickness is also the thicker boundary layer investigated. The boundary layers on the top and bottom are $\delta_{99} \approx 0.1712h$ and $0.1642h$ respectively. A set of follow-on experiments to the work by [7] was conducted by Shannon and Morris [87]. They found that dominant phase behavior indicating a dominant frequency was present. Their work is another point of comparison for evaluating the flow field results.

5.3.1 Flow-field validation

Bulk parameters are compared where possible with the cited experiments and computations. The St number for the principal oscillation of the wake was found by Shannon and Morris [87] to be 0.42, Olson and Mueller [7] found 0.40, Wang [8] to be 0.44, and we calculate it at 0.41. The boundary layer profile comparisons along the upper surface

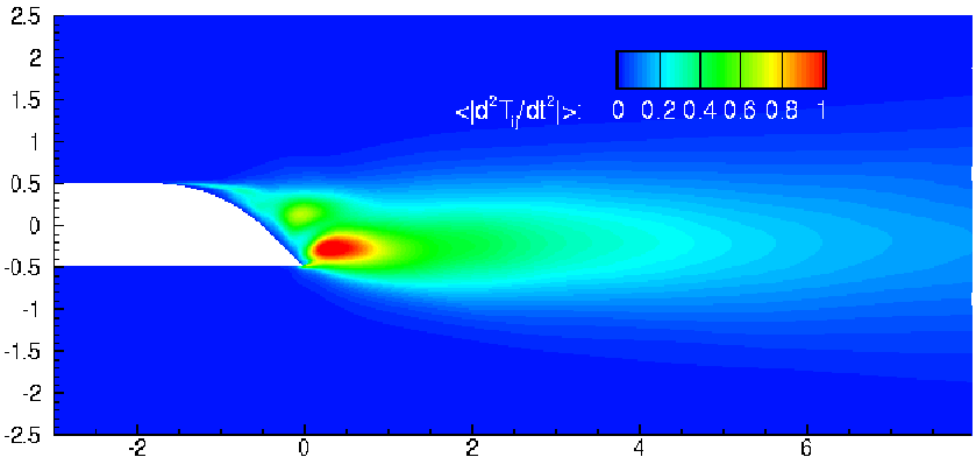

Figure 5.5: Sound sources ($< \frac{\partial^2 T_i j}{\partial t^2} >$) on oversized grid. Note the lack of deflection due to non-consistent boundary layers.

boundary are shown in figure 5.7. The mean streamwise wake profiles downstream of the trailing edge are shown in figure 5.8 which show close agreement between all methods. The evolution of the rms values of u-velocity are shown in figure 5.9. Wang [8] computed the kinetic energy for the velocity components directly behind the trailing edge point at $(x/h, y/h) = (0.5, 0)$ and the comparison is shown in figure 5.10. This reiterates the reasonable flow field comparison in the near wake region.

5.3.2 Acoustic results

The acoustic sources for the experimental boundary layer condition are examined using the time average of their absolute values. The sound sources at the trailing edge surface are the fluctuation pressure dp/dt and the volume terms throughout the entire domain are the second time derivative of the Lighthill stress field. The surface forces are shown in figure 5.11 as the magnitude of the vectors along the trailing edge. The volumetric source fields are shown in figure 5.12, and similar to the cylinders, strong vorticity vectors nearly perpendicular to the background velocity produce large amounts of noise. These regions are associated with the Reynolds stress component $\overline{u'u'}$ in particular, as the vorticity is released from the wall and is accelerated in the downstream direction.

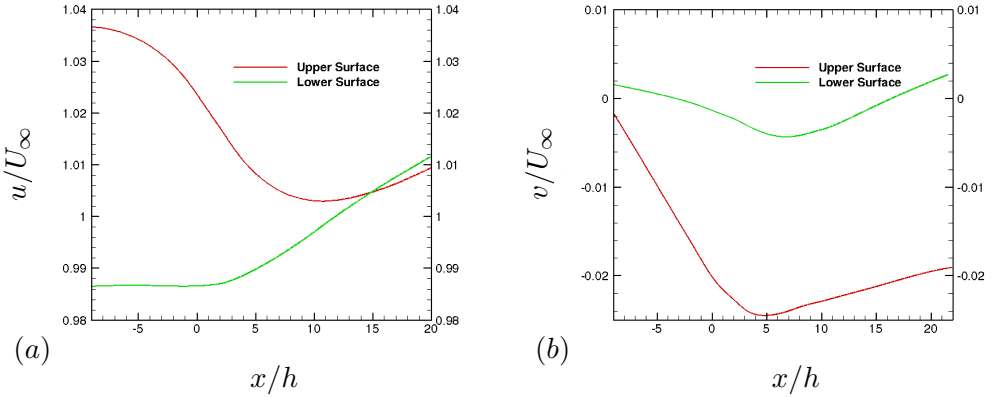

Figure 5.6: The extracted u-velocity (a) and v-velocity (b) which are used as boundary conditions for the smaller, more highly resolved domain calculations.

5.4 Thin boundary layer

The thinner boundary layer, initialized to be 18 times thinner, provides the opportunity to investigate the difference in noise production due to the prescribed boundary thickness. This thickness should affect the noise production due to less momentum being available to delay boundary layer separation on the top surface as well as the boundary layer interaction along the pressure side with its abrupt ejection into the freestream at the trailing edge point. These changes to fluctuating velocities near the trailing edge point should impact noise production.

5.4.1 Flow-field validation

There are no direct comparisons which can be made to validate the flow-field for the thinner boundary layer. A flow visualization showing the u-velocity which clearly demonstrates the thinness of the boundary layer is shown in figure 5.13. This is further reinforced with the boundary layer profile comparison in figure 5.15 which shows how much thinner (momentum thickness θ is 12 to 18 times thinner). Also note how the boundary layer at $x/h = -1.625$ close to the beginning of the bevel thins much faster than in the thicker case. The effect on the fluctuating velocities is shown if figure 5.14 as both the regions of activity and the intensities have diminished.

Table 5.1: Summary of polynomial coefficients for boundary condition.

Coefficient	u_{top}	u_{bot}	v_{top}	v_{bot}
f_1	0.0011	7.424e-5	2.345e-4	-6.47e-10
f_2	6.227e-5	3.859e-5	1.648e-4	-1.912e-4
f_3	-0.0116	-6.928e-4	-0.002	1.132e-4
f_4	0.0025	-4.01e-5	-9.529e-4	0.0014
f_5	0.0186	0.0023	0.0065	-6.327e-4
f_6	-0.0148	-5.575e-4	9.751e-4	-0.0041
f_7	1.0	-0.0059	-0.0104	0.0016
f_8		0.0056	0.0059	0.0066
f_9		0.0122	0.0027	-0.0014
f_10		0.9913	-0.0226	-0.0049

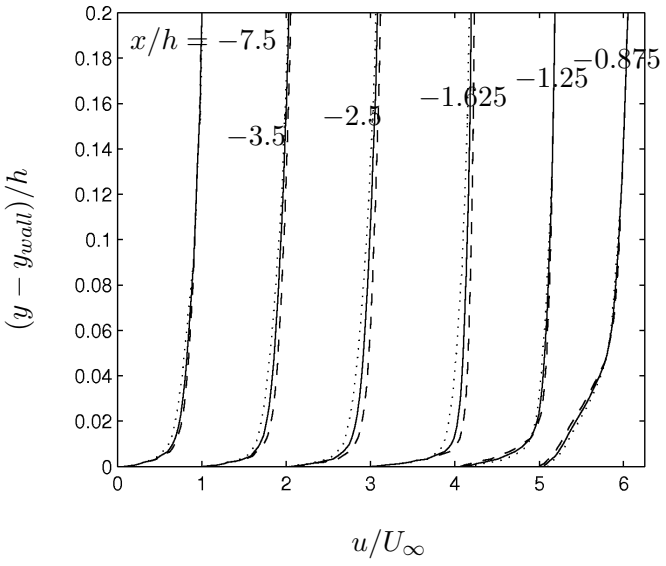

Figure 5.7: Boundary layer comparison at various x-locations between (–) current, (- -) Wang [8], ($\cdots$) Olson and Mueller [7].

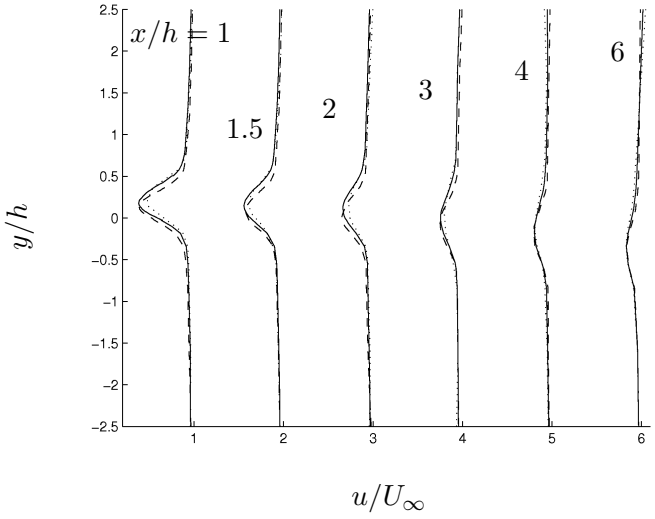

Figure 5.8: Mean u-velocity wake profiles between (–) current, (- -) Wang [8], ($\cdots$) Olson and Mueller [7].

5.4.2 Acoustic results

The sources of sound for the thin boundary layer case are similar to those of the larger case, except decreased in amplitude and extent. Figure 5.16 shows the mean of the absolute value of dp/dt or the mean of the magnitude of the surface sources which produce noise. The volumetric terms are shown in the contour figure 5.17. The regions of noise production as well as their intensities are smaller than for the thicker boundary layer case. Furthermore, the noise production associated with the shear layer on the upper surface is diminished due to the thinner momentum thickness layer which interacts over a shorter length.

5.5 Combined results and effect of boundary layer thickness

The noise production from both boundary layer thickness cases is evaluated by examining the point spectra at a given location and the directivity that is associated with the entire body. The noise at a point $(x/h, y/h) = (3, 21)$ in the near field is shown in figure 5.18. Also shown is the experimental measurement obtained using a two-point acoustic

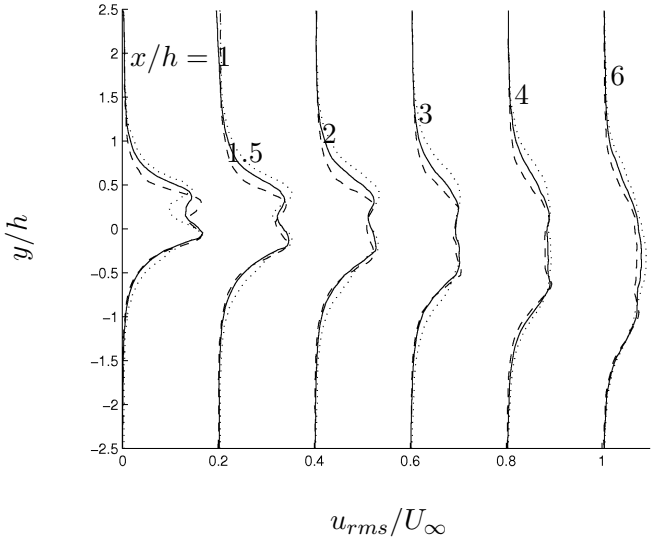

Figure 5.9: Mean u-velocity rms wake profiles between (–) current, (- -) Wang [8], ($\cdots$) Olson and Mueller [7]

array. The Nyquist frequency of the experiment is 4000 Hz and a 10 Hz passband filter is applied to the data; in contrast, the Nyquist frequency of the computations is 100000 Hz and no passband filter is used. The thick boundary layer case shows good agreement with experiment. The mismatch at low frequencies is characteristic of such comparison as mentioned in chapter 4. At high frequencies the simulations capture more sound due to the higher Nyquist frequency which is also higher than that of [8].

The directivity is computed at a distance $r/h = 100$; the maximum $SPL = 42.2dB$ in the upstream direction. Neither the experiment nor Wang's computation report directivity. The relative sound pressure level is plotted in figure 5.19. Qualitatively our directivity is similar to the experiments of Singer et al. [91] and the computations of Oberai et al. [90] who investigated noise from two-dimensional airfoils.

Note that as the boundary layer thins less noise is produced and the directivity shifts. There is increased energy content at higher frequencies for the thin boundary layer, but not significantly. Instead, the largest change occurs in the noise production near the shedding frequency. This directly corresponds to the fact that the thinner boundary layer separates later but with lower intensity, thus producing less pressure fluctuations and Reynolds stresses over a smaller region. This lack of noise production

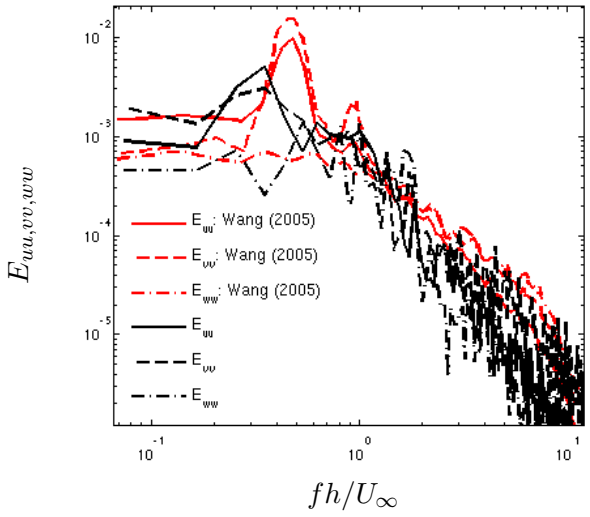

Figure 5.10: Energy spectra versus frequency at$(x/h, y/h) = (0.5, 0)$.

is preferentially directed in the upper half plane in the downstream direction. This is most likely due to the fact that separation over the lower surface always happens at the same point and that it is the directly radiated noise from the bluff body wake along the bevel which accounts for the difference.

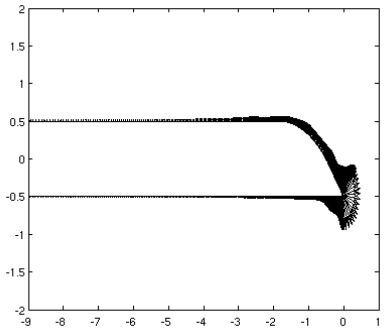

Figure 5.11: Surface sources for experimental boundary layer case.

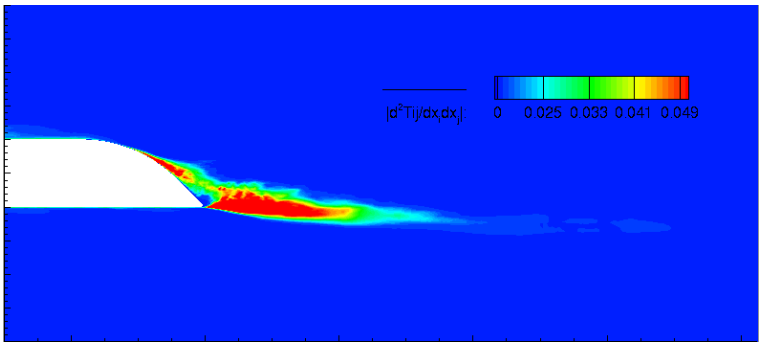

Figure 5.12: Volumetric sound sources for experimental boundary layer case.

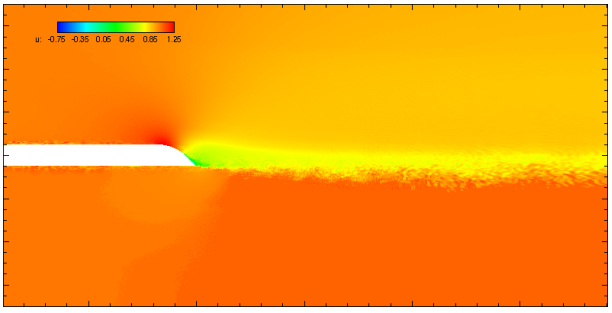

Figure 5.13: Instantaneous u-velocity visualization of the thin boundary layer case.

5.6 Effect of Green's function

A significant motivation to develop the porous FWH methodology is that it enables the use of the free-space Green's function irrespective of geometrical complexity. In this section we demonstrate the reasonableness of this approach by comparing the sound prediction to that obtained using only the surface terms and half-plane Green's function. The half-plane Green's function provides a good representation for the trailing edge. It was described by Williams and Hall [81]; from which Crighton [92] then provided a two-dimensional compact Green's function representation.Howe [93] then represented the Green's function in physical space using the method of stationary phase to achieve,

$$G(\mathbf{x},\mathbf{y},t-\tau) \approx \frac{\varphi(\mathbf{x})\varphi(\mathbf{y})}{4\pi|x|}\delta(t-\tau-|\mathbf{x}|/c_0) \tag{5.3}$$

where $\varphi(.) = \sqrt{r^*}sin(\theta^*/2)$, for each location, $(.)^*$, defined in polar coordinates: $\mathbf{x} = (r_x cos(\theta_x), r_x sin(\theta_x), x_{3,x})$ and $\mathbf{y} = (r_y cos(\theta_y), r_y sin(\theta_y), y_{3,y})$.

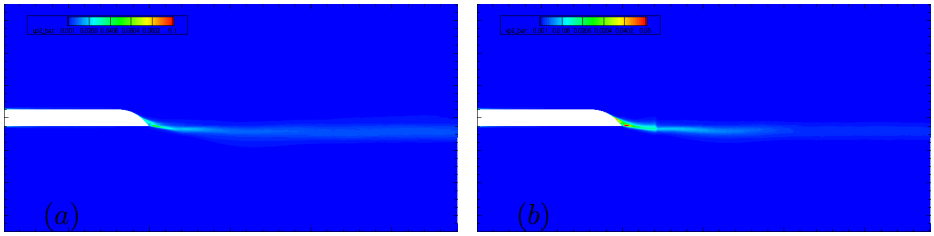

Figure 5.14: Reynolds stress components (a) $\overline{u'u'}$ and (b) $\overline{v'v'}$ for the thin boundary layer case are shown.

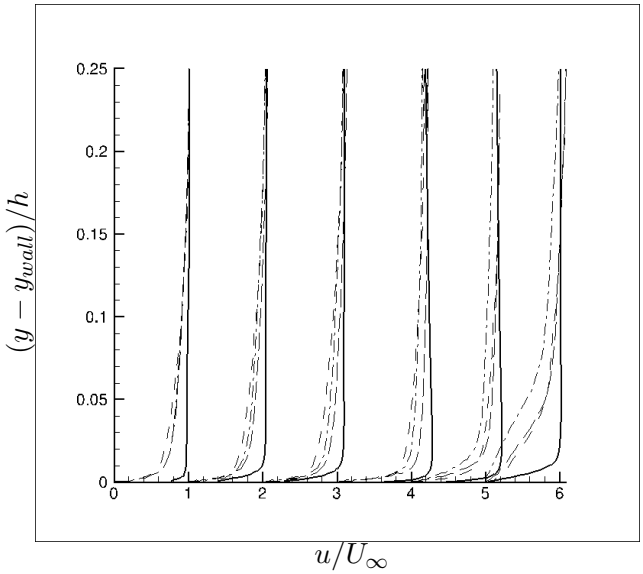

Figure 5.15: Boundary layer profiles compared with the thicker case.

The acoustic calculations have been performed with a porous FWH implementation with the porous surfaces located $1.5h$ away from upper and lower surfaces and $1.5h$ downstream of the trailing edge point as well implementing 5.3 using surface terms. The grid refinement in this area provides high quality resolution resulting in almost a third of all processors having control volumes cut by these porous surfaces. The point noise (figure 5.20) and directivity (figure 5.21) are computed using both approaches for the experimental boundary layer case. It is clear that their are differences are slight. This points to the considerable attractiveness of our porous FWH methodology and the effectiveness of our dynamic endcap approach.

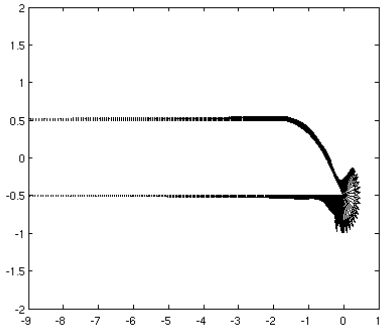

Figure 5.16: Mean surface sources, $|dp/dt|$, plotted as the magnitude of the vectors for the thin boundary layer.

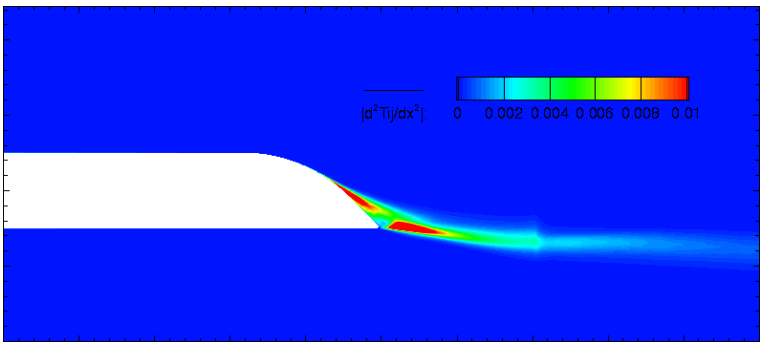

Figure 5.17: Mean of $|\partial^2 T_{ij}/\partial t^2|$ for thin boundary layer case.

5.7 Summary

Our FWH method was applied to a 45° beveled trailing edge. The flow and show fields show good agreement with experiment. The approach for obtaining this agreement involved using an oversized lower fidelity computation in order to obtain reasonable boundary conditions to achieve a comparable coefficient of pressure with experiment. The use of the recycle rescale methodology was also important in order to get boundary layers that were in close agreement with the experiment. These boundary layers dictate both separation as well as fluctuating Reynolds stress components which were in close agreement with those previously observed.

The directivity and the effect of boundary layer thickness are examined. Physical insights developed from the cylinder flow prove useful for examining noise production

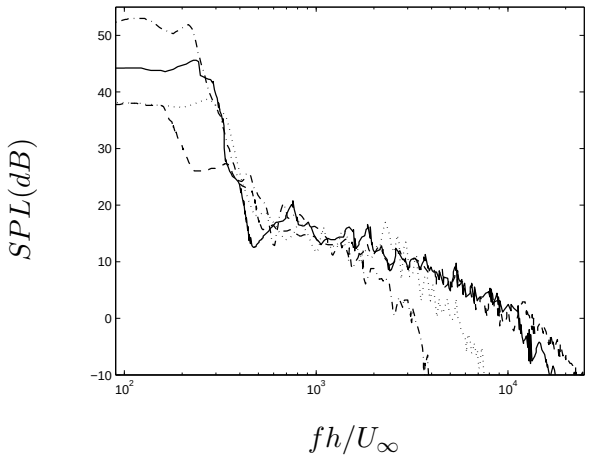

Figure 5.18: Comparison of noise from (–) current thick, (- -) current thin, (-.) Olson and Mueller [7], and $(\cdots)$ Wang [8]

from the trailing edge. Between the two boundary layer thicknesses, the vorticity shed into the wake is larger for the thinner boundary layer, but since it separates later, the values of $\vec{\omega} \times \vec{u}$ are lower. Also, this thinner boundary layer results in a smaller region of source distribution. On the lower surface of the trailing edge boundary layer separation happens at roughly the same location and $\frac{\partial^2 u'u'}{\partial t^2}$ is the dominant source term which is produced over a thinner region but is almost as intense and therefore produces comparable noise.

Our porous FWH methodology is shown to agree well with sound predicted using the surface terms and a half-plane Green's function. This points to the considerable promise of our methodology to predict the sound from turbulent flows and complex configurations.

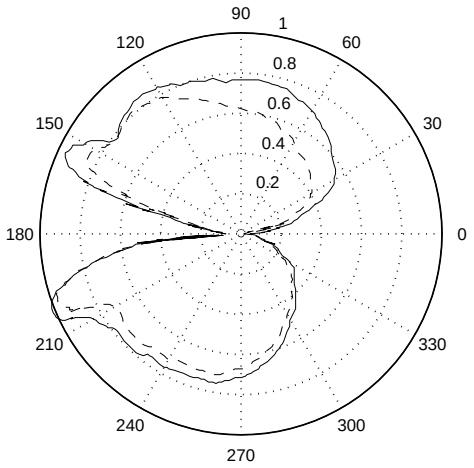

Figure 5.19: Sound Directivity for (–) thick and (- -) thin boundary layers.

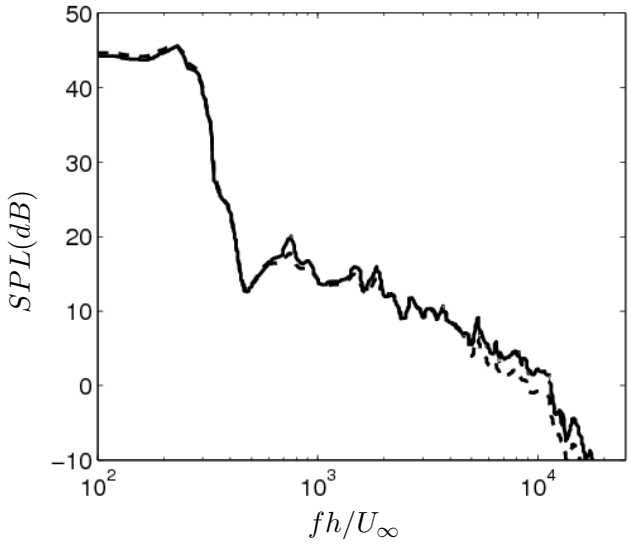

Figure 5.20: Point sound comparison using the half-plane Green's function with surface terms or the porous FWH approach.

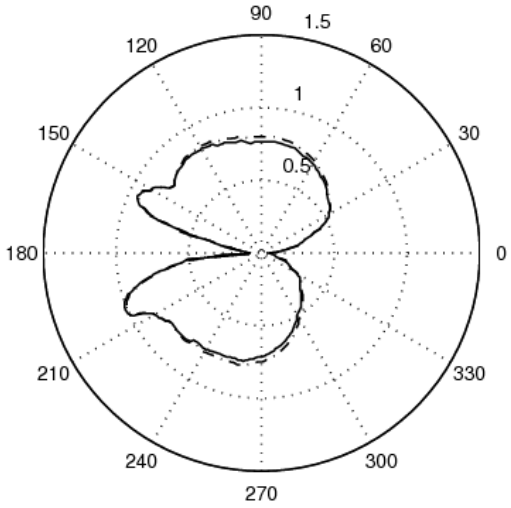

Figure 5.21: Sound directivity for the experimental boundary layer using (-.) the half-plane Green's function with surface terms or (–) the porous FWH approach.

References

[1] M.L. Shur, P.R. Spalart, and M.K. Strelets. Noise prediction for increasingly complex jets, part 1: Methods and tests. *International Journal of Aeroacoustics*, 4(3-4):213–246, 2005.

[2] A. Verma and K. Mahesh. A Lagrangian Subgrid-scale Model with Dynamic Estimation of Lagrangian Time Scale for Large Eddy Simulation of Complex Flows. *Physics of Fluids*, 24(8):085101, 2012.

[3] O. Inoue and N. Hatakeyama. Sound Generation by a Two-dimensional Circular Cylinder in a Uniform Flow. *Journal of Fluid Mechanics*, 471:285–314, 2002. ISSN 0022-1120.

[4] Y. Khalighi, A. Mani, F. Ham, and P. Moin. Prediction of Sound Generated by Complex Flows at Low Mach Numbers. *AIAA Journal*, 48(2):306–316, 2010.

[5] J.D. Revell, R.A. Prydz, and A.P. Hays. Experimental study of airframe noise versus drag relationship for circular cylinders. Final report for NASA contract NAS1-14403, Lockheed Report 28074, 1977.

[6] J.S. Cox, K.S. Brentner, and C.L. Rumsey. Computation of vortex shedding and radiated sound for a circular cylinder: subcritical to transcritical Reynolds numbers. *Theoretical and Computational Fluid Dynamics*, 12:233–253, 1998.

[7] S. Olson and T.J. Mueller. Phased array acoustic imaging of an airfoil trailing edge flow. In *11th International Symposium on Flow Visualization*, 2004.

[8] M. Wang. Compuation of trailing-edge aeroacoustics with vortex shedding. *Center for Turbulence Research: Annual Research Briefs*, pages 379–388, 2005.

[9] A.S. Lyrintzis. Integral Methods in Computational Aeroacoustics -From the CFD Near-Field to the Acoustic Far-Field. *International Journal of Aeroacoustics*, 2 (2):95–128, 2003.

[10] M.J. Lighthill. On sound generated aerodynamically. part I: General theory. *Proceedings of the Royal Society of London*, A(211):564–587, 1952.

[11] N. Curle. The influence of solid boundaries upon aerodynmic sound. *Proceedings of the Royal Society of London*, A(231):505–514, 1955.

[12] J.E. Ffowcs-Williams and D.L. Hawkings. Sound generation by turbulence and surfaces in arbitrary motion. *Philosophical Transactions of the Royal Society of London*, 264A:321–342, 1969.

[13] T.S. Lund, X. Wu, and K.D. Squires. Generation of Turbulent Inflow Data for Spatially-Developing Boundary Layer Simulations. *Journal of Computational Physics*, 140(2):233–258, 1998.

[14] J. Smagorinsky. General circulation experiments with the primitive equations: I. the basic experiment. *Monthly Weather review*, 91(3):99–164, 1963.

[15] M. Germano, U. Piomelli, P. Moin, and W.H. Cabot. A Dynamic Subgrid-scale Eddy Viscosity Model. *Physics of Fluids A*, 3(7):1760–1765, 1991.

[16] C. Meneveau, T. S. Lund, and W. H. Cabot. A Lagrangian Dynamic Subgrid-scale Model of Turbulence. *J. Fluid Mech.*, 319:353, 1996.

[17] N. Park and K. Mahesh. Reduction of the Germano-identity error in the dynamic Smagorinsky model. *Physics of Fluids*, 21(6):065106, 2009.

[18] K. Mahesh, G. Constantinescu, and P. Moin. A numerical method for large-eddy simulation in complex geometries. *J. Comput. Phys.*, 197(1):215, 2004.

[19] N. Park and K. Mahesh. Numerical and modeling issues in les of compressible turbulent flows on unstructred grids. *AIAA Paper*, 722, 2007.

[20] M. Wang and P. Moin. Computation of trailing-edge flow and noise using large-eddy simulation. *AIAA Journal*, 38(12):2201–2209, 2000.

[21] K.S. Brentner, J.S. Cox, C.L. Rumsey, and B.A. Younis. Computation of sound generated by flow over a circular cylinder: an acoustic analogy approach. In *NASA Conference Publication*, pages 289–296. NASA, 1997.

[22] M.S. Howe. *Theory of Vortex Sound*. Cambridge: University Press, 2003.

[23] S.C. Crow. Stability Theory for a Pair of Trailing Vortices. *AIAA Journal*, 8(12): 2172–2179, 1970.

[24] A. Verma, H. Jang, and K. Mahesh. The effect of an upstream hull on a propeller in reverse rotation. *J. Fluid Mech.*, 704:61–88, 2012.

[25] A. Jang and K. Mahesh. Large eddy simulation of flow around a reverse rotating propeller. *Journal of Fluid Mechanics*, 729:151–179, 2013.

[26] P. Babu and K. Mahesh. Upstream entrainment in numerical simulations of spatially evolving round jets. *Phys. of Fluids*, 16(10):3699–3705, 2004.

[27] S. Muppidi and K. Mahesh. Study of trajectories of jets in cross-flow using direct numerical simulations. *Journal of Fluid Mechanics*, 530:81–100, 2005.

[28] S. Muppidi and K. Mahesh. Direct numerical simulation of round turbulent jets in crossflow. *Journal of Fluid Mechanics*, 574:449–461, 2007.

[29] S. Muppidi and K. Mahesh. Direct numerical simulation of passive scalar transport in transverse jets. *Journal of Fluid Mechanics*, 598:335–360, 2008.

[30] URL https://computation.llnl.gov/casc/hypre/software.html.

[31] H. Jang. *Large eddy simulation of crashback in marine propulsors*. PhD thesis, University of Minnesota, 2011.

[32] H.C. Yee, N.D. Sandham, and M.J. Djomehri. Low-dissipative high-order shock-capturing methods using characteristic-based filters. *Journal of Computational Physics*, 150(1):199–238, 1999.

[33] P. Iyer, S. Muppidi, and K. Mahesh. Boundary layer transition in high-speed flows due to roughness. *AIAA Paper*, 1106, 2012.

[34] S. Muppidi and K. Mahesh. DNS of roughness-induced transition in supersonic boundary layers. *Journal of Fluid Mechanics*, 693:28–56, 2012.

[35] X. Chai and K. Mahesh. Dynamic-equation model for large-eddy simulation of compressible flows. *Journal of Fluid Mechanics*, 699:385–413, 2012.

[36] D.P. Lockard. A comparison of Ffowcs Williams-Hawkings solvers for airframe noise applications. *AIAA paper*, 2580(8), 2002.

[37] K. S. Brentner and F. Farassat. Modeling Aerodynamically Generated Sound of Helicopter Rotors. *Progress in Aerospace Sciences*, 39(2-3):83–120, 2003.

[38] J.E. Ffowcs-Williams. Sound sources in aerodynamics–fact and fiction. *AIAA Journal*, 20(3):307–315, 1982.

[39] M Wang, S.K. Lele, and P. Moin. Computation of quadrupole noise using acoustic analogy. *AIAA Journal*, 34(11):2247–2254, 1996.

[40] A. Najafi-Yazdi, G.A. Bres, and L. Mongeau. An acoustic analogy formulation for moving sources in uniformly moving media. *Proceedings of the Royal Society A: Mathematical, Physical and Engineering Sciences*, 467(2125):144–165, 2010.

[41] O.M. Phillips. The Intensity of Aeolian tones. *Journal of Fluid Mechanics*, 1(6): 607–624, 1956.

[42] J.C. Hardin and S.L. Lamkin. Aeroacoustic computation of cylinder wake flow. *AIAA Journal*, 22(1):51–57, 1984.

[43] C. Cheong, P. Joseph, Y. Park, and S. Lee. Computation of Aeolian tone from a circular cylinder using source models. *Applied Acoustics*, 69(2):110–126, 2008.

[44] D.P. Lockard. An Efficient, Two-Dimensional Implementation of the Ffowcs Williams and Hawkings Equation. *Journal of Sound and Vibration*, 229(4):897–911, 2000.

[45] P. Beaudan and P. Moin. Numerical Experiments on the Flow Past a Circular cylinder at Sub-Critical Reynolds Number. Thermosciences Division, Dept. of Mechanical Engineering TF-62, Stanford University, 1994.

[46] C. Norberg. Fluctuating lift on a circular cylinder: review and new measurements. *Journal of Fluids and Structures*, 17(1):57–96, 2003.

[47] U. Fey, M. König, and H. Eckelmann. A new Strouhal Reynolds-number relationship for the circular cylinder in the range $47 < re < 105$. *Physics of Fluids*, 10: 1547–1549, 1998.

[48] X. Gloerfelt, F. Perot, C. Bailly, and D. Juve. Flow-induced cylinder noise formulated as a diffraction problem for low Mach numbers. *Journal of Sound and Vibration*, 287:129–151, 2005.

[49] J.C. Hardin and D.S. Pope. An acoustic/viscous splitting technique for computational aeroacoustics. *Theoretical and Computational Fluid Dynamics*, 6(5-6): 323–340, 1994.

[50] J.H. Gerrard. An experimental investigation of the oscillating lift and drag of a circular cylinder shedding turbulent vortices. *Journal of Fluid Mechanics*, 11(02): 244–256, 1961.

[51] A. Roshko. Experiments on the flow past a circular cylinder at very high Reynolds number. *Journal of Fluid Mechanics*, 10(03):345–356, 1961.

[52] M.V. Morkovin. Flow around circular cylinder: a kaleidoscope of challenging fluid phenomena. In *ASME Symposium on Fully Separated Flows*, pages 102–118. The American Society of Mechanical Engineers New York, 1964.

[53] Morris Macovsky. Vortex-induced vibration studies. Technical Report Rep. 1190, U.S. Navy Dept., D. Taylor Model Basin, 1958.

[54] R.E.D. Bishop and A.Y. Hassan. The lift and drag forces on a circular cylinder in a flowing fluid. In *Proceedings of the Royal Society of London A: Mathematical, Physical and Engineering Sciences*, volume 277, pages 32–50. The Royal Society, 1964.

[55] S. Taniguchi and K. Miyakoshi. Fluctuating fluid forces acting on a circular cylinder and interference with a plane wall. *Experiments in Fluids*, 9(4):197–204, 1990.

[56] E. Achenbach and E. Heinecke. On vortex shedding from smooth and rough cylinders in the range of Reynolds numbers 6×10^3 to 5×10^6. *Journal of fluid mechanics*, 109:239–251, 1981.

[57] G.S. West and C.J. Apelt. Measurements of fluctuating pressures and forces on a circular cylinder in the Reynolds number range 10^4 to 2.5×10^5. *Journal of Fluids and Structures*, 7(3):227–244, 1993.

[58] J.P. Batham. Pressure distributions on circular cylinders at critical Reynolds numbers. *Journal of Fluid Mechanics*, 57(02):209–228, 1973.

[59] A. Elmiligui, K.S. Abdol-Hamid, S.J. Massey, and S.P. Pao. Numerical study of flow past a circular cylinder using RANS, hybrid RANS/LES and PANS formulations. In *22nd Applied Aerodynamics Conference and Exhibit, Rhode Island*, 2004.

[60] G. Schewe. On the force fluctuations acting on a circular cylinder in crossflow from subcritical up to transcritical Reynolds numbers. *Journal of Fluid Mechanics*, 133: 265–285, 1983.

[61] R.P. Hansen and J.R. Forsythe. Large and detached eddy simulations of flow over a circular cylinder using unstructured grids. In *41st Aerospace Sciences Meeting and Exhibit, AIAA*, volume 775, 2003.

[62] T. Colonius, S.K. Lele, and P. Moin. The scattering of sound waves by a vortex: numerical simulations and analytical solutions. *Journal of Fluid Mechanics*, 260: 271–298, 1994.

[63] B. Cantwell and D. Coles. An experimental study of entrainment and transport in the turbulent near wake of a circular cylinder. *Journal of Fluid Mechanics*, 136: 321–374, 1983.

[64] M. E. Goldstein. *Aeroacoustics*. New York: McGraw-Hill, 1976.

[65] W.K. Blake. Dipole sound from cylinders. In *Mechanics of Flow-Induced Sound and Vibration, vol 1: General Concepts and Elementary Sources*, pages 219–287. Academic Press, Inc., New York, 1986.

[66] P.E. Doak. Acoustic radiation from a turbulent fluid containing foreign bodies. In *Proceedings of the Royal Society of London A: Mathematical, Physical and Engineering Sciences*, volume 254, pages 129–146. The Royal Society, 1960.

[67] J.E. Ffowcs-Williams. Hydrodynamic noise. *Annual Review of Fluid Mechanics*, 1(1):197–222, 1969.

[68] D.G. Crighton and F.G. Leppington. On the scattering of aerodynamic noise. *Journal of Fluid Mechanics*, 46(3):577–597, 1971.

[69] S.A. Slimon, M.C. Soteriou, and D.W. Davis. Computational aeroacoustics simulations using the expansion about incompressible flow approach. *AIAA Journal*, 37(4):409–416, 1999.

[70] F. Pérot, J. Auger, H.e Giardi, X. Gloerfelt, and C. Baily. Numerical prediction of the noise radiated by a cylinder. *AIAA Paper*, 3240(9), 2003.

[71] P. Catalano, M. Wang, G. Iaccarino, and P. Moin. Numerical simulation of the flow around a circular cylinder at high Reynolds numbers. *International Journal of Heat and Fluid Flow*, 24(4):463–469, 2003.

[72] L. Ong and J. Wallace. The velocity field of the turbulent very near wake of a circular cylinder. *Experiments in fluids*, 20(6):441–453, 1996.

[73] A.G. Kravchenko and P. Moin. Numerical studies of flow over a circular cylinder at $Re_D = 3900$. 12(2):403–417, 2000.

[74] LM Lourenco and C Shih. Characteristics of the plane turbulent near wake of a circular cylinder, a particle image velocimetry study. *private communication*, 1993.

[75] M. Breuer. Numerical and modeling influences on large eddy simulations for the flow past a circular cylinder. *International Journal of Heat and Fluid Flow*, 19 (5):512–521, 1998.

[76] S Szepessy and PW Bearman. Aspect ratio and end plate effects on vortex shedding from a circular cylinder. *Journal of Fluid Mechanics*, 234:191–217, 1992.

[77] A. Fage and V.M. Falkner. *Further experiments on the flow around a circular cylinder*. HM Stationery Office, 1931.

[78] A. Powell. Theory of vortex sound. *The Journal of the Acoustical Society of America*, 36(1):177–195, 1964.

[79] A.P. Dowling. *Vortex sound*. Springer, London, 1992.

[80] L. Gutin. On the sound field of a rotating propeller. 1948.

[81] J.E. Williams and L.H. Hall. Aerodynamic sound generation by turbulent flow in the vicinity of a scattering half plane. *Journal of Fluid Mechanics*, 40(04): 657–670, 1970.

[82] M.S. Howe. A review of the theory of trailing edge noise. *Journal of Sound and Vibration*, 61(3):437–465, 1978.

[83] W.K. Blake. A statistical description of pressure and velocity fields at the trailing edges of a flat strut. Technical report, DTIC Document, 1975.

[84] W.K. Blake. Mechanics of flow-induced sound and vibration. *New York*, page 9, 1986.

[85] J.L. Gershfeld, W.K. Blake, and C.W. Knisely. Trailing edge flows and aerodynamic sound. In *AIAA Thermophysics, Plasmadynamics and Lasers Conference, San Antonio, Texas AIAA Paper*, volume 3826, pages 2133–2140, 1988.

[86] W.K. Blake and J.L. Gershfeld. The aeroacoustics of trailing edges. In *Frontiers in Experimental Fluid Mechanics*, pages 457–532. Springer, 1989.

[87] D.W. Shannon and S.C. Morris. Experimental investigation of a blunt trailing edge flow field with application to sound generation. *Experiments in Fluids*, 41 (5):777–788, 2006.

[88] D.W. Shannon, S.C. Morris, and T.J. Mueller. Radiated sound and turbulent motions in a blunt trailing edge flow field. *International Journal of Heat and Fluid Flow*, 27(4):730–736, 2006.

[89] E. Manoha, B. Troff, and P. Sagaut. Trailing-Edge Noise Prediction Using Large-Eddy Simulation and Acoustic Analogy. *AIAA Journal*, 38(4):575–583, 2000. ISSN 0001-1452.

[90] A.A. Oberai, F. Roknaldin, and Thomas J. Computation of Trailing-Edge Noise Due to Turbulent Flow over an Airfoil. *AIAA Journal*, 40(11):2206–2216, 2002.

[91] B.A. Singer, K.S. Brentner, and G.M. Lockard, D.P .and Lilley. Simulation of Acoustic Scattering from a Trailing Edge. *AIAA paper*, 231:1999, 1999.

[92] D.G. Crighton. Radiation from a vortex filament motion near a half plane. *Journal of Fluid Mechanics*, 51(02):357–362, 1972.

[93] M.S. Howe. Contributions to the theory of aerodynamic sound, with application to excess jet noise and the theory of the flute. *Journal of Fluid Mechanics*, 71: 625–673, 1975.

[94] F. Farassat. Discontinuities in aerodynamics and aeroacoustics: the concept and applications of generalized derivatives. *Journal of Sound and Vibration*, 55(2): 165–193, 1977.

[95] F. Farassat and M. Farris. Verification and analysis of formulation 4 of Langley for the study of noise from high speed surfaces. *AIAA paper*, pages 99–1881, 1999. 5th AIAA/CEAS Aeroacoustics Conference, Bellevue, WA, May 1999.

[96] P. Di Francescantonio. A new boundary integral formulation for the prediction of sound radiation. *Journal of Sound and Vibration*, 202(4):491–509, 1997.

[97] B. Morgan, J. Larsson, S. Kawai, and S.K. Lele. Improving low-frequency characteristics of recycling/rescaling inflow turbulence generation. *AIAA Journal*, 49 (3):582–597, 2011.

[98] P.R. Spalart, M. Strelets, and A. Travin. Direct numerical simulation of large-eddy-break-up devices in a boundary layer. *International Journal of Heat and Fluid Flow*, 27(5):902–910, 2006.

[99] P.R Spalart. Direct simulation of a turbulent boundary layer up to Re_θ= 1410. *Journal of Fluid Mechanics*, 187:61–98, 1988.

[100] P. Schlatter and R. Örlü. Assessment of direct numerical simulation data of turbulent boundary layers. *Journal of Fluid Mechanics*, 659:116–126, 2010.

Appendix A

Important Ffowcs-Williams Hawkings derivations and additional formulations

A.1 Introduction

Additional formulations of the FWH equations have been performed by a variety of authors ([78], [94], [95], and [93] for example) much in the same way that the Navier-Stokes equations can be rewritten to track quantities such as enstrophy. For example, [4] prescribes a formulation which decouples scattered and incident noise. A few alternative formulations and comments are highlighted in this appendix.

A.1.1 Importance of time derivatives

The time derivatives in equation 2.67 can be brought inside the integrals since the Leibnitz boundary terms are zero due to the radiation condition and the retarded time. In this case, the time derivatives in received time are transformed to time derivatives at emission time. This makes our FWH equations

$$\begin{aligned} p'(\mathbf{x},t) &= \frac{1}{4\pi|\mathbf{x}|}\int \frac{\partial}{\partial\tau}Q_i n_i dS - \frac{x_i}{4\pi c_0|\mathbf{x}|^2}\int \frac{\partial}{\partial\tau}L_{ij}n_j dS \\ &+ \frac{x_i x_j}{4\pi c_0^2|\mathbf{x}|^3}\int_{V_{ext}} \frac{\partial^2}{\partial\tau^2}T_{ij}dV. \end{aligned} \tag{A.1}$$

So the sources of the integrand are $\dot{Q}_i n_i, Q_i \dot{n}_i, \dot{L_{ij}} n_j, L_{ij} \dot{n}_j$, and $\ddot{T_{ij}}$, which represent the time rate of change of the mass flux, the force distribution, and the 'acceleration' of the Lighthill stress field as well as the effect of normal vectors changing. The terms governing porous surface motion, those which include v_n, are also important and are used in this formulation. This approach has been used by [37] and for the thickness and loading term, including the near-field terms which decay like $1/r^2$, at the surface $f = 0$ using the notation $M_r = Mcos(\theta)$ to account for mean background convection results in Formulation 1A. The equation is repeated here,

$$\begin{aligned} 4\pi p'(\mathbf{x},t) &= \int \left[\frac{\rho_0(\dot{v_n} + \dot{v_{\dot{n}}})}{r|1-M_r|^2}\right] dS + \int \left[\frac{\rho_0 v_n (r\dot{M}_r + cM_r - cM^2)}{r^2|1-M_r|^3}\right] dS \\ &+ \frac{1}{c}\int \left[\frac{\dot{l_r}}{r|1-M_r|^2}\right] dS + \int \left[\frac{l_r - l_M}{r|1-M_r|^2}\right] dS \\ &+ \frac{1}{c}\int \left[\frac{l_r (r\dot{M}_r + cM_r - cM^2)}{r^2|1-M_r|^3}\right] dS. \end{aligned} \tag{A.2}$$

A.2 Mean convection case

If mean background convection is analytically separated from the standard representation of u_n, or v_n which can handle mean flow, the influence can be seen analytically. This approach was first investigated by Di Francescantonio [96]. For example, rewriting the continuity equation,

$$\frac{\partial \rho}{\partial t} + U_c \frac{\partial \rho}{\partial x} + \frac{\rho u_j}{\partial x_j} = 0. \tag{A.3}$$

Following the process laid forth in [40] leads to a monopole term and dipole term

$$Q_i = \rho(u_i + U_{c,i} - v_i) + \rho_0(v_i - U_{c,i}) \tag{A.4}$$

$$L_{ij} = \rho u_i (u_j + U_{c,j} - v_j) + \Delta P_{ij}. \tag{A.5}$$

The Lighthill term is unaffected, but the wave equation is modified to account for the fact that $\partial/\partial t \rightarrow \partial/\partial t + U_c \partial/\partial x_1$ which leads to the equations 3.6.

A.3 Notes on collapsing sphere and emission surface formulations

Two other standard implementations of the FWH equations were derived by [94] which are the collapsing sphere and emissions surface approach. The principal benefit of rearranging the FWH equations in this manner is that they eliminate shock singularities allowing integration for sonic and supersonic flows. The physical interpretations are described in [37] and are as follows. The change of variables of the bounds of integration $dy_1 dy_2 dy_3 d\tau$ in equations like 2.53 results in the different forms. The standard retarded time formulation is associated with the exchange of variables $(y3, \tau) \rightarrow (f, g)$.

If noise at a particular point and time is desired only sources on a collapsing sphere of radius $c_0\tau$ can contribute. The sphere has integration area Γ and requires the exchange of variables $(y2, y3) \rightarrow (f, g)$. Therefore,

$$d\mathbf{y}d\tau = \frac{dy_1 df dg}{\partial(f,g)/\partial(y_2,y_3)} = \frac{dy_1 df dg}{(\nabla f \times \nabla g)\cdot \hat{e_1}}. \tag{A.6}$$

For a general source $\mathcal{F}$, this leads to a FWH equation

$$4\pi p'(\mathbf{x},t) = \int_{-\infty}^{t}\int_{f,g=0} \frac{\mathcal{F}}{rsin\theta} cd\Gamma d\tau \tag{A.7}$$

For the emission surface, entire planes emit noise at a given location and time. The integration element therefore becomes $|\nabla F|$ and N_3 is the third component of the emission surface $F = 0$. In this case, it has been shown that the substitution of variables $(y3, \tau) \rightarrow (F, g)$ leads to

$$d\mathbf{y}d\tau = \frac{dy_1 dy_2 dF dg}{\partial(F,g)/\partial(y_3,\tau)} = \frac{dy_1 dy_2 dF dg}{\partial F/\partial y_3} = \frac{d\Sigma dF dg}{|\nabla F|} \tag{A.8}$$

which for a general source $\mathcal{F}$ leads to a FWH equation like

$$4\pi p'(\mathbf{x},t) = \int_{F=0}\left[\frac{\mathcal{F}}{r\Lambda}\right] d\Sigma. \tag{A.9}$$

A.4 Kelvin Helmholtz frequency derivation

The inhomogeneous wave equation can be transformed into frequency space through the use of Fourier transforms. The resulting wave equation is

$$(\nabla^2 + k_0^2)\hat{\varphi} = \hat{\mathcal{F}}(\mathbf{x}, w) \tag{A.10}$$

where the hat denotes the fourier transform or one frequency component, $k_0 = w/c$ is the acoustic wavenumber, and has frequency w. The free-space Green's function becomes

$$\hat{G}(\mathbf{x}, \mathbf{y}, w) = \frac{-e^{ik_0|\mathbf{x}-\mathbf{y}|}}{4\pi|\mathbf{x}-\mathbf{y}|}. \tag{A.11}$$

This leads to the solution for the Fourier transformed pressure $\hat{p}$ as,

$$\begin{aligned} \hat{p}(\mathbf{x}, w) &= -\frac{1}{4\pi}\int \frac{\hat{q}(\mathbf{y}, w)e^{ik_0|x-y|}}{|\mathbf{x}-\mathbf{y}|}d^3\mathbf{y} \\ &- \frac{1}{4\pi}\frac{\partial}{\partial x_j}\int \frac{f_j(\mathbf{y}, w)e^{ik_0|x-y|}}{|\mathbf{x}-\mathbf{y}|}d^3\mathbf{y} \\ &- \frac{1}{4\pi}\frac{\partial^2}{\partial x_i \partial x_j}\int \frac{T_{ij}(\mathbf{y}, w)e^{ik_0|x-y|}}{|\mathbf{x}-\mathbf{y}}d^3\mathbf{y}. \end{aligned} \tag{A.12}$$

A.5 Vortex sound equations: the Lamb vector

The momentum equation of the Navier-Stokes equations can be recast into the Crocco form involving the Lamb vector, $\vec{\omega} \times \vec{v}$, where $\vec{\omega}$ is the vorticity. In the case when the viscous dissipation is neglected, Crocco's equation becomes

$$\frac{\partial v}{\partial t} + \vec{\omega} \times \vec{v} + \nabla B = -\nu(\nabla \times \vec{\omega}) \tag{A.13}$$

where B is the total enthalpy $B = \int \frac{dp}{\rho} + 1/2v^2$. [22] demonstrates how to obtain an acoustic analogy for compact body assumption. It involves combining the definition of total enthalpy after rearranging to solve for pressure, and differentiating with respect to time and using the divergence of Crocco's equation written in the form of equation A.13, in a similar fashion to chapter 2. The resulting equation for the principle dipole component to the far-field noise for a non vibrating compact body is

$$p'(\mathbf{x}, t) \approx \frac{-\rho_0 x_j}{4\pi c_0 |\mathbf{x}|^2}\frac{\partial}{\partial t}\int (\mathbf{w} \times \mathbf{v})(\mathbf{y}, t - \frac{|\mathbf{x}|}{c_0}) \cdot \nabla Y_j(y) d^3y. \tag{A.14}$$

Note the dependence on the Lamb vector, or the importance on the vorticity interacting with the velocity field to generate noise. This source is the principle source of sound generated by the flow itself in many cases. This interacting with the surface, denoted by the $\nabla Y_j(y)$, is the principal interaction for sound radiation to the far-field, generated by the flow and radiated by the body.

Appendix B

Unstructured grid decomposition using Delaunay triangulation

B.1 Introduction

The geometric grid extraction techniques are detailed and discussed in this appendix. The integrals over surfaces are implemented by summing up source contributions on the extracted face areas. In order to project control volume data onto the given face locations the second order least-squares derivatives of the source quantities are used. The way in which the porous surface grid is generated is important in order to be representative of the underlying control volume grid, which ensures accurate extrapolation, with the added goal of making the face normals piecewise continuous. The general approach that has been implemented in order to achieve these goals is as follows.

- Specify the planes, semi-cylinders or hemispheres, grid tagged planes, or polynomial surface representations which are desired.
- Specify the links for these plane structures to form a closed surface
- Specify a point that is 'in' each FWH exit volume
- Find which control volumes that are cut by these surfaces and retain this map as shown in figure B.1. The cv is represented on the plane by the perpendicular projection point.

- Flatten any three-dimensional extraction planes into two-dimensional representations and calculate an initial convex hull.
- Find the exterior edge by sorting nearest distance of points found to be on the exterior based on
  - An assigned boundary, such as 'wall' or 'cylinder'.
  - An inter-processor ghost cv used to exchange inter-processor communication.
  - Truncation due to the desired edge of a plane being reached which causes a change in the convex hull. This is done recursively by eliminating points within a tolerance zone to ensure all points are found even when the boundary which is truncated is non-monotonic.
- Order the found projected cv locations in clockwise fashion which facilitates the Delaunay triangulation.
- Perform a constrained Delaunay triangulation constrained by the previously exterior edge condition.
- Construct the mesh dual Voronoi diagram of the triangulation with the cutoff bounds being the projected cv faces or the prescribed maximal extent. This provides the face area which represents the cv volume being cut.
- Compute the 'inner' and 'outer' volumes through a ray tracing intersection algorithm. Link lists together of which control volumes, both partial and full, exist within each FWH exit volume or regular volume. The ray tracing intersection algorithm works by utilizing the point specified as 'in' and then projecting a ray along a vector and counting the number of intersections with the bounding surface. If the intersection count is odd, then the point is on the inside, if it is even it is on the outside. This process is repeated for the three principal directions as a check.

B.1.1 Implementation in an acoustic analogy code

This process occurs only once overall and all relevant data is recorded so that it doesn't have to be repeated during subsequent runs. The output is the cv to plane map index,

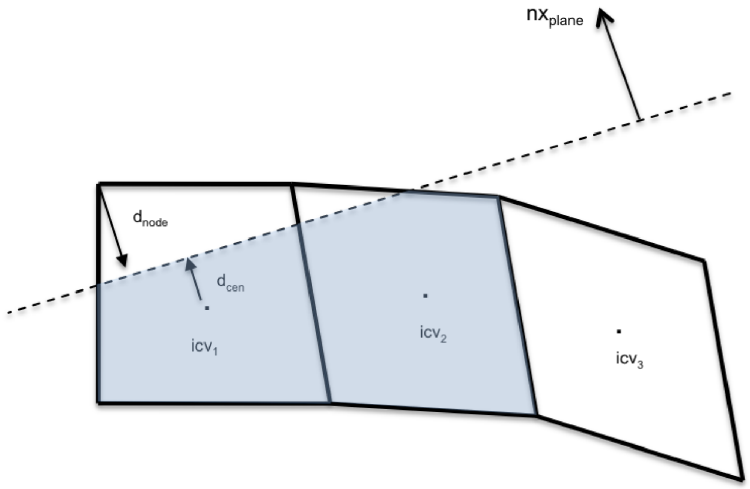

Figure B.1: A control volume is cut if at least one signed nodal distance to plane is of opposite direction from the signed distance of the volume centroid to the plane. Here icv1 and icv2 are found to be members of the plane and icv3 is left intact

the face areas, the face connectivity, the cv to exit volume lists, and the adjusted cv volumes for cut cv's. This process for the 82 million cv cylinder took approximately 20 minutes to process 15 planes resulting in 10 FWH surfaces and 11 exit volumes.

B.2 Constrained Delaunay and Voronoi dual

The pseudo code for a constrained Delaunay triangulation and its Voronoi mesh dual are given below. A Delaunay triangulation is one in which the circle circumscribing the triangle contains no other points of the triangulation map in its interior. It should be note that strictly speaking, constrained Delaunay triangulations do not produce triangulations which are Delaunay, instead the triangulation is Delaunay in the interior away from the boundary. The algorithm that was implemented was an incremental insertion flip algorithm which stores a pointer of previous flip dependencies. The algorithm takes $O(n \log n)$ time; $O(n)$ to insert each point and $O(\log n)$ to check the previous flips. A Voronoi diagram is a mesh which has elements which are equidistant from all Delaunay triangulation nodes. The Voronoi dual is calculated from a tree branching algorithm that searches for connections in the triangulation to find nearest neighbors to construct

lines of equal distance.

- **Begin:** with sorted data and 3 non-colinear points.
  - Determine if point 3 is clockwise or counter-clockwise handed.
  - Based on result, build triangle in counter-clockwise ordering and update triangle neighbor lists.
- **Main Loop:** insert points from outside the current convex hull
  - Establish which edge of current triangulation is closest and determine handedness of the point to the edge.
  - Update the stack of attached triangles with the current one.
  - **Internal loop:** using the stack list swap internal edges amongst the four points to ensure Delaunay or constrained condition.
    - If a triangle is swapped figure out attached triangles to the update vertices and add them to the stack.

B.3 Example surface

In the following example, a plane at $z = 0$ is extracted from a cylinder grid. Figure B.2 shows the cylinder and its assigned boundary as well as inter-processor boundaries since only one processor's information is displayed. This example demonstrates both the constrained nature of the triangulation as well as the truncation associated with the Voronoi diagram to create face areas. In figure B.2 the full triangulation is shown, as well as a close up near the cylinder boundary. The red boundary is the exterior edge that is located. Note how the constrained triangulation will at most attach triangles to other boundary elements since one side of the triangle is constrained to this exterior edge. The closeup in B.2 (b) shows how the constrained edged from the assigned boundary cylinder transitions to the more irregular inter-processor boundaries.

The Voronoi diagram is shown in full and in close up in figure B.3. The full Voronoi diagram shows how the lines of constant distance extend to infinity and therefore need to be truncated by the lines associated with the projected nodes from the control volume

grid. In the close-up, the face elements and the face centroid are shown. Here it is made very clear how the inter-processor face centroid locations as well as the truncation procedure produces a regular face grid and structure. It is these face elements which dictate centroid locations and areas. Recall that the face centroids will be the nodes of the Delaunay triangulation which in-turn were the projected cv centers from the solution grid.

These extraction techniques are demonstrated for a rotor problem showing a box encompassing a rotor in figure B.4. This visualization shows how the extracted face grid is representative of the underlying control volume grid.

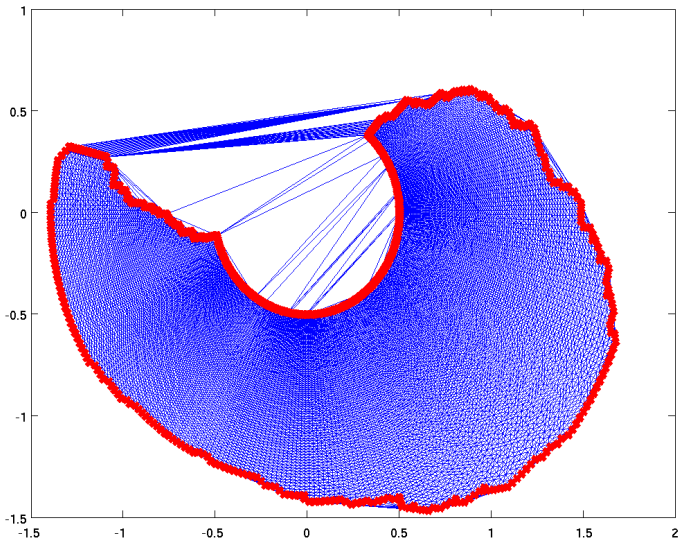

(*a*)

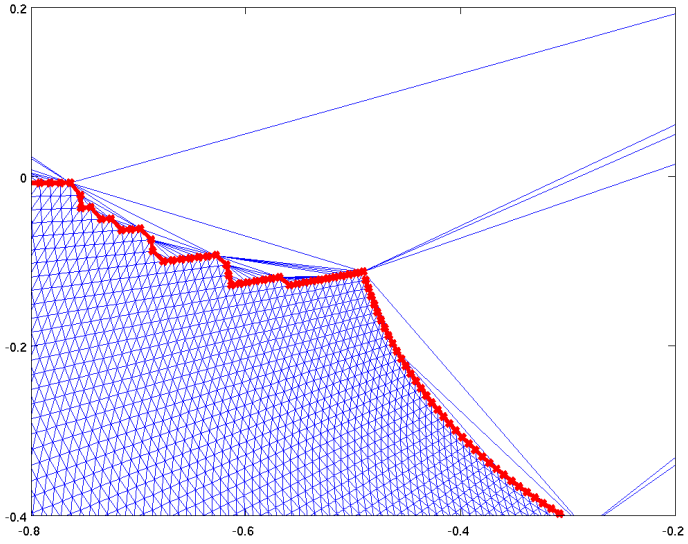

(*b*)

Figure B.2: The constrained Delaunay triangulation for the example case is shown. (a) shows the entire triangulation for the entire processor and (b) shows a close-up view with the boundary outlined in red.

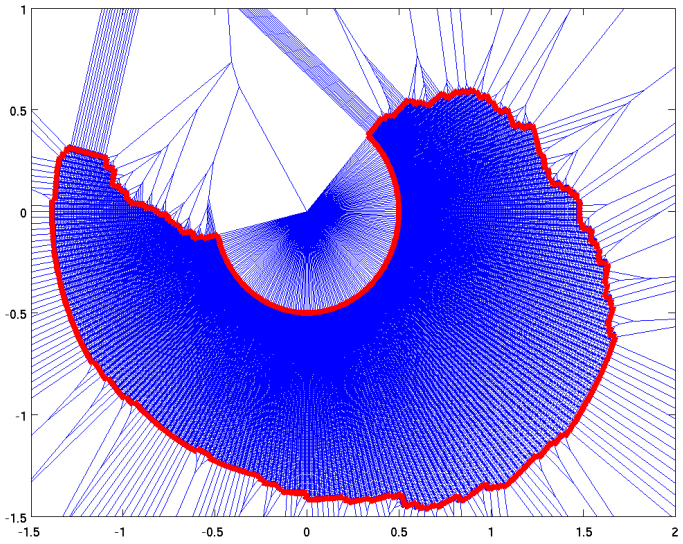

(*a*)

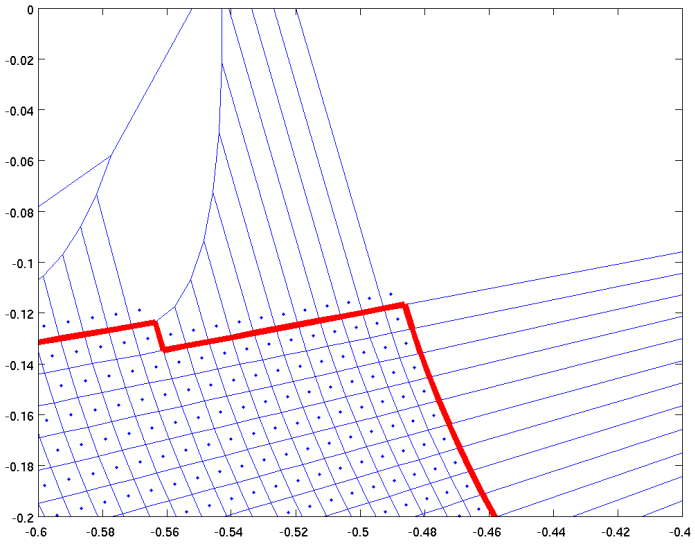

(*b*)

Figure B.3: The Voronoi diagram is shown in blue with the red boundary line. (a) is the full processor and (b) is a closeup view showing off the extracted face grid.

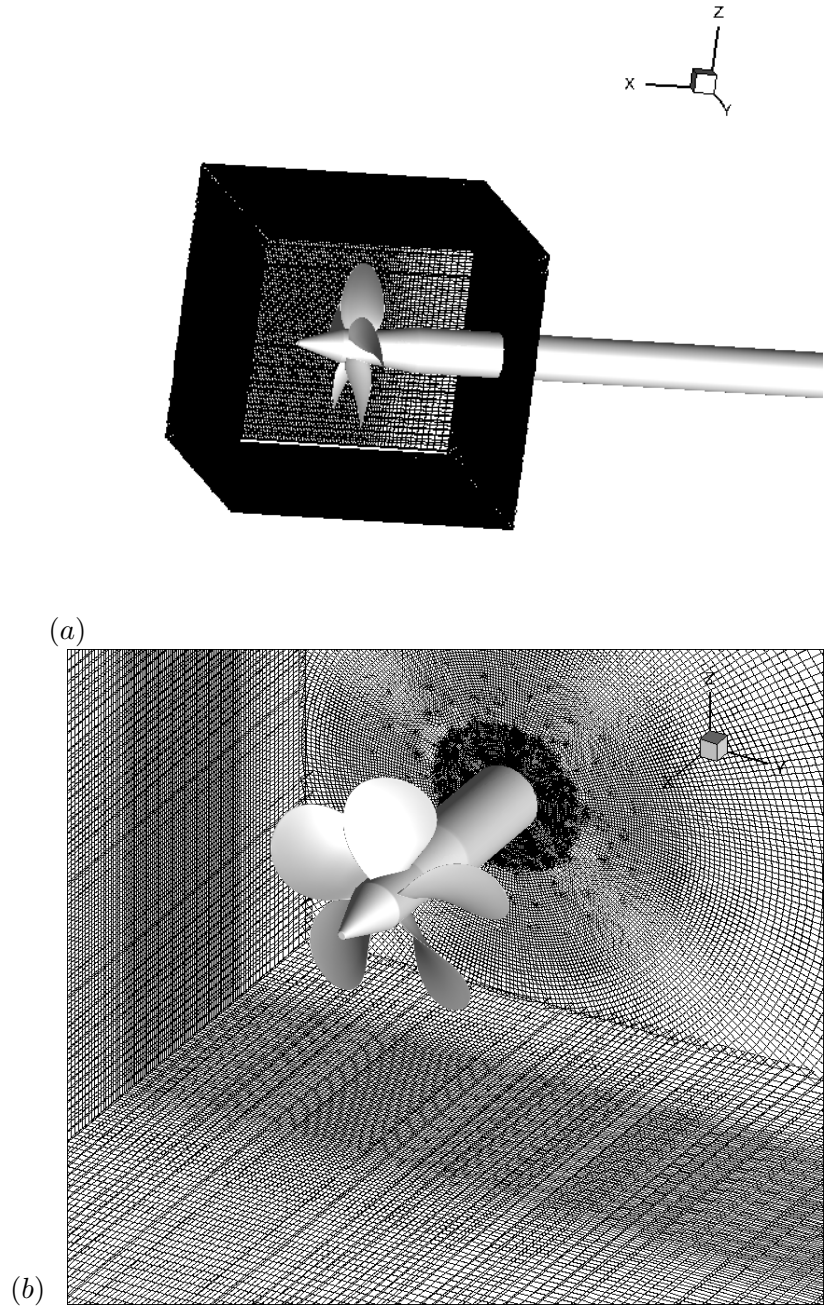

Figure B.4: A porous FWH surface box around a propeller is shown from far away in (a) as well as closeup in (b).

Appendix C

Recycle Rescale methodology

C.1 Introduction and methodology

Generating physically correct inflow for simulations is not a trivial task especially as Re_θ increases, θ being the momentum thickness. The popular approach of recycle-rescale introduced by Lund et al. [13] has been implemented in the incompressible code. The method uses instantaneous flow quantities at a location downstream of the inflow plane which are then rescaled based on inner and outer scales and fed back into or recycled at the inflow. The method decomposes decomposes the flow field into a mean and a fluctuating velocity component and treats the inflow as the sum of the two rescaled. The solution undergoes a dynamic shift and reflection method proposed by Morgan et al. [97] in the span which reduces low frequency correlations found in [97] and Spalart et al. [98]. Specifically, the velocities at the inflow $x = x_{in}$ are

$$\begin{aligned} u(y,z,t) &= \beta[\gamma\bar{U}(x_r,y_r^o,t) + (1-\gamma)U_\infty + \gamma u'(x_r,y_r^o,z_r,t)] \\ &+ (1-\beta)[\gamma\bar{U}(x_r,y_r^i,t) + \gamma u'(x_r,y_r^i,z_r,t)], \qquad \text{(C.1)} \\ v(y,z,t) &= \beta[\bar{V}(x_r,y_r^o,t) + \gamma v'(x_r,y_r^o,z,t)] \\ &+ (1-\beta)[\bar{V}(x_r,y_r^i,t) + \gamma v'(x_r,y_r^i,z,t)] \qquad \text{(C.2)} \\ w(y,z,t) &= \beta\gamma w'(x_r,y_r^o,z,t) + (1-\beta)\gamma w'(x_r,y_r^i,z,t) \qquad \text{(C.3)} \end{aligned}$$

where the $\bar{(\cdot)}$ is the spanwise average through time, 'r' denotes the recycle plane, 'i' denotes the inner scale, 'o' denotes the outer scale, and as mentioned the z location goes

through a shift/reflection procedure. The inner scales are based on the $y+ = u_\tau y/\nu$ scaling and the outer scales are based on $\eta = y/\delta_{99}$. β is the Lund et al. [13] weighting function which blends inner and outer scales with constants $a = 4$ and $b = 0.2$,

$$\beta(\eta) = \frac{1}{2}\left\{\frac{1 + tanh\left(\frac{a(\eta-b)}{(1-2b)\eta+b}\right)}{tanh(a)}\right\} \tag{C.4}$$

The mean boundary layer profile provides the scaling parameters at the recycle plane $(\delta_{99,r}, u_{\tau,r})$ and the mean profile is established as a spanwise average at every timestep which is then averaged via a sliding window average. The averaging time window is either set to $T_w = A\delta_{99,i}|_0/U_\infty$ where $A = 10$ for the initialization transient period or $A = 100$ for the statistically averaged steady-state as recommended by Lund et al. [13]. The sliding window averaging scheme is implemented as,

$$\mathcal{F}(t) = \left(1 - \frac{\Delta t}{T_w}\right)\mathcal{F}(t - \Delta t) + \frac{\Delta t}{T_w} f(t) \tag{C.5}$$

where $\mathcal{F}$ is the running average and f is the instantaneous spanwise average.

The rescale parameter γ is defined in preferential order as one of the following,

$$\gamma = \frac{u_{\tau,r}}{u_{\tau,i}} = \left(\frac{\theta_r}{\theta_i}\right)^{(1/8)} \approx \left(\frac{\delta_{99,r}}{\delta_{99,i}}\right)^{(1/8)} \tag{C.6}$$

In order to maintain the boundary layer profiles that are desired any one of the inflow parameters $u_\tau, \theta,$ or δ_{99} are specified. This in combination with the rescale equation,

$$u_{\tau,i} = u_{\tau,r}\left(\frac{\theta_r}{\theta_i}\right)^{(1/8)}, \tag{C.7}$$

which may need to be rearranged depending on your fixed parameter, provides a way to obtain all four scaling parameters. This is accomplished through a Newton-Rapson scheme which fixes the unchosen inflow parameter based on the scaling in order to obtain the fixed parameter.

C.2 Validation

In order to validate the recycle rescale methodology, a flat plate boundary layer simulation was performed for a $Re_\theta = 1410$ boundary layer. The boundary layer momentum

thickness was set to 0.1 units on a grid that was 20 units tall and 35 units long. The grid had approximately 14 million control volumes and 10 points in the viscous sublayer below the height of $y^+ = 5$.The sliding average with the premultiplier of 10 as well as a specified friction velocity of 0.044 was used for the first 20 units of time to establish the friction velocity and inner scales. After that point, only the prescribed inflow momentum thickness constrained the problem.

C.2.1 Statistically averaged results

The mean and rms velocity profiles are shown in figures C.1, and C.2 (a)-(d). Very good agreement is found between our results for the mean boundary layer profile, shown in figure C.1, to [13], [99], and [100]. The maximum fluctuating velocities of $u'u'_{rms}$ occur at the near wall and are higher than DNS but lower than [13] due to increased grid resolution. The other fluctuating velocity components show very good agreement.

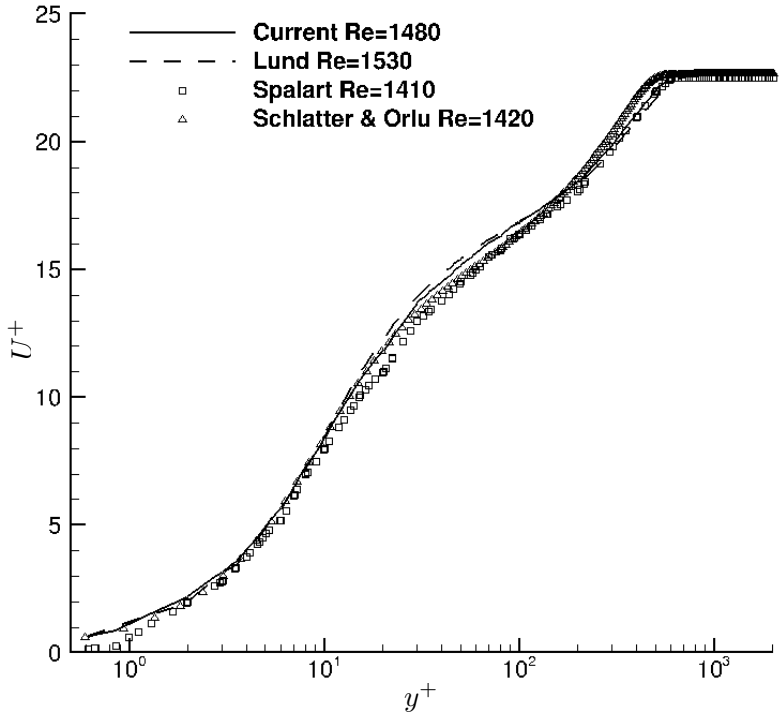

Figure C.1:

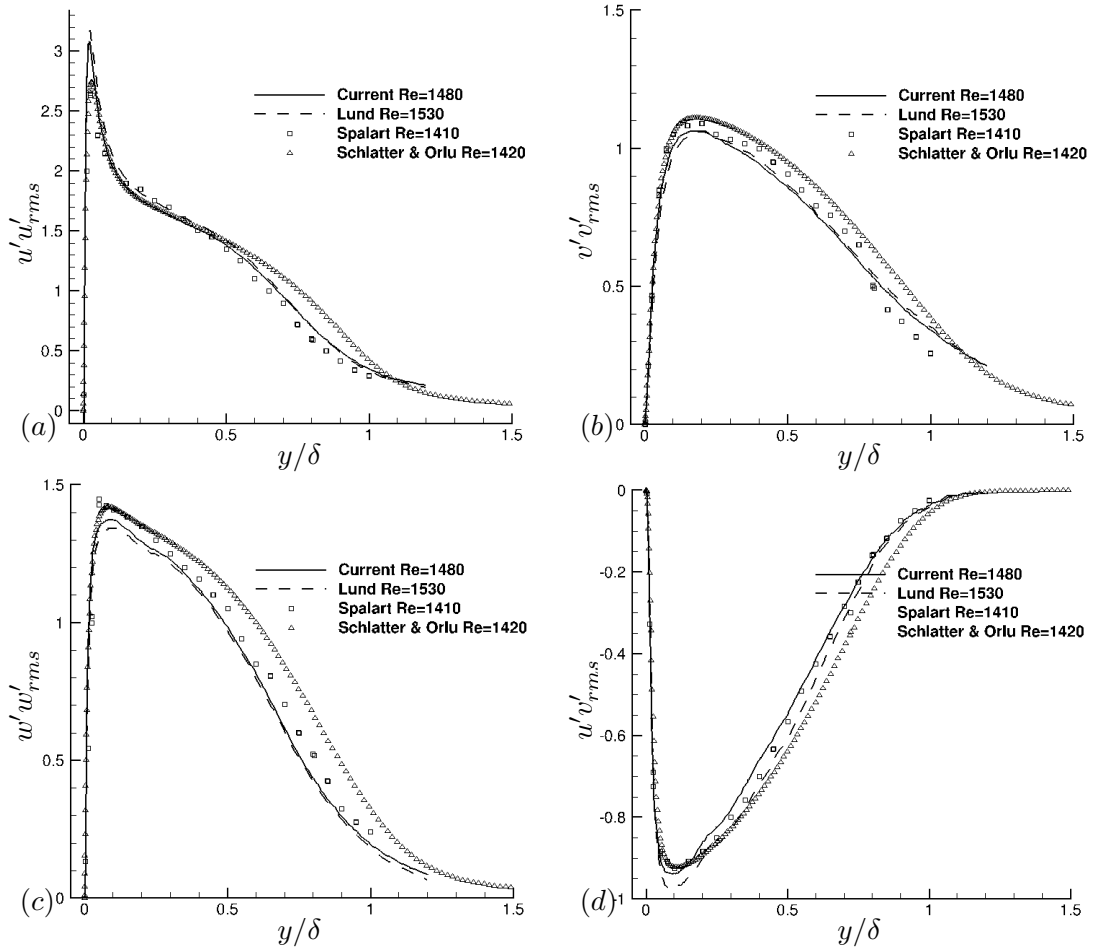

Figure C.2: The rms of the fluctuating velocities. (a) $\overline{u'u'_{rms}}$, (b) $\overline{v'v'_{rms}}$, (c) $\overline{w'w'_{rms}}$, (d) $\overline{u'v'_{rms}}$

Boundary layer growth profiles

The boundary layer growth profiles are compared to [13] and [99] in figure C.3 (a)-(c). Momentum thickness θ, displacement thickness, δ^*, and the boundary layer height, δ, are all compared. Good agreement is found in their growth rates.

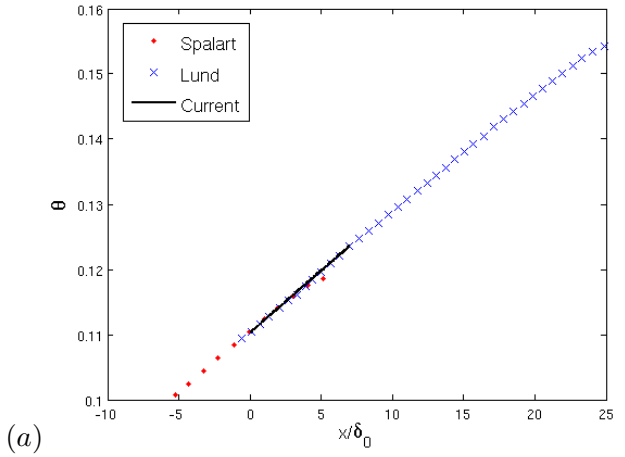

(a)

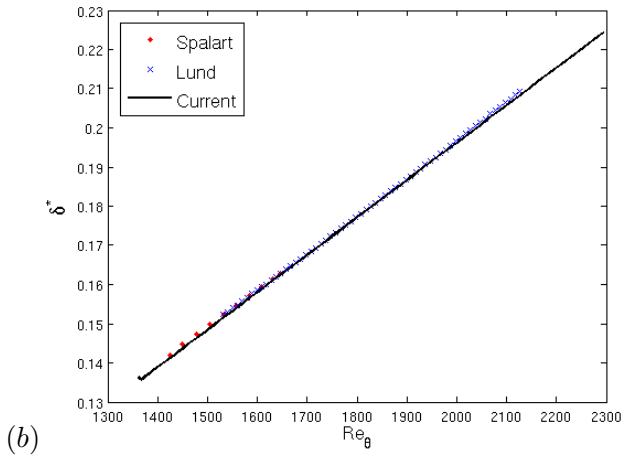

(b)

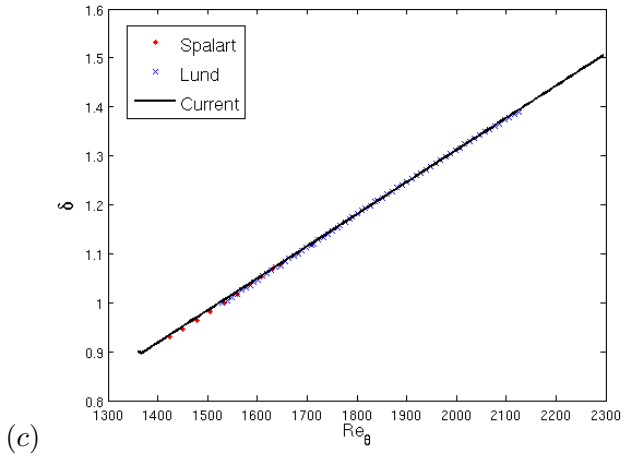

(c)

Figure C.3: The boundary layer growth profile comparisons.